Dissertation

ANALYSIS OF FIBER REINFORCED FILAMENT WOUND ROTORS

ausgeführt zum Zwecke der Erlangung des akademischen Grades eines Doktors der technischen Wissenschaften unter der Leitung von

Univ.-Prof. Dipl.-Ing. Dr.techn. Manfred Kaltenbacher

E325

Institut für Mechanik und Mechatronik

eingereicht an der Technischen Universität Wien

Fakultät für Maschinenwesen und Betriebswissenschaften

von

Dipl.-Ing. Stefan Hartl

Matrikelnummer 0726285

Spittelauer Platz 5/5-6, 1090 Wien

Wien, am

Kurzfassung

In dieser Arbeit wird das mechanische Verhalten von gewickelten faserverstärkten Rotoren analysiert, welche in Schwungradspeichern verwendet werden. Diese Art der Speicherung von elektrischer Energie ist eine ökologisch und ökonomisch nachhaltige Technologie für die dezentrale Energiespeicherung mit langen Lebenszyklen ohne Leistungseinbußen durch zu hohe Entladungstiefe und einem Minimum an System-Wartung. Die Hauptkomponente eines Schwungradspeichers ist der schnell drehende Rotor, bei dem die große Herausforderung in der Maximierung der Energiedichte besteht, welche von den verwendeten Materialien, der Geometrie des Rotors und dem Entwurf abhängt. Der komplexe Aufbau dieser Rotoren erfordert einen rechnergestützten Entwurfsprozess einschließlich der Kenntnis der Materialparameter.

Der erste Teil der Arbeit befasst sich mit der Identifikation der Materialparameter, welche für die weiteren Finite-Elemente (FE) Simulationen benötigt werden. Dafür müssen die elastischen Materialparameter und die Festigkeiten bestimmt werden. Der Messaufwand für faserverstärkte Materialien, vor allem für kohlefaserverstärkten Kunststoff (CFK), ist wesentlich höher im Vergleich zu isotropen Materialien, weil durch das orthotrope Materialverhalten deutliche Unterschiede quer zur Faserrichtung auftreten. Die Auswahl geeigneter Materialien für den entworfenen Rotor des Schwungradspeichers erfolgt mit Hilfe einer neu entwickelten zerstörungsfreien Methode, bei der die elastischen Materialparameter durch Modalanalyse von faserverstärkten Platten bestimmt werden. Nach der Auswahl und der Definition von wiederholbaren Prozessparametern für die Herstellung werden zerstörende Prüfungen, basierend auf Normen, an hochfestem und hochsteifem CFK Material durchgeführt.

Zur Gewährleistung aller Sicherheitsaspekte befasst sich der zweite Teil der Arbeit mit einem statischen Berstversuch für Rotoren von Schwungradspeichern. Das präsentierte statische Testverfahren für eine kontrollierte Initiierung des Berstens von faserverstärkten Rotoren zeigt nahezu die gleiche Spannungsverteilung wie im dynamischen Fall bei hoher Drehzahl. Das Versagen wird dabei mit unterschiedlichen Maximal-Spannungskriterien und einem Sicherheitsfaktor bestimmt. Die Ergebnisse der statischen FE-Simulation des statischen Berstversuchs stimmen gut mit den quasi-statischen FE-Simulationsergebnissen des Rotors überein. Weiterhin wird gezeigt, dass das vorgestellte Verfahren eine sehr gut steuerbare und beobachtbare Möglichkeit ist, um einen schnell drehenden Rotor statisch zu testen. Dadurch ist es möglich, einen sehr viel teureren und gefährlicheren dynamischen Berstversuch mit möglichen Unsicherheiten zu ersetzen.

Schließlich werden die Methoden und Erkenntnisse aus den zerstörenden Prüfungen und dem Berstversuch an einem neuartigen Rotorentwurf angewandt. Dieser Entwurf besteht aus einer CFK-Hohlwelle, verpresst in einer Multi-Ring CFK Schwungmasse, bestehend aus drei verpressten Ringen, die einen H-förmigen Rotorquerschnitt bilden. Mit dieser Konfiguration lässt sich die Energiedichte im Vergleich zu einem Rotorentwurf, bestehend aus einer Aluminium Welle, verpresst in einer dickwandigen CFK Schwungmasse, erhöhen. Darauffolgend werden Messungen zur Validierung der FE-Simulationen des Rotors und zur Bestimmung der Charakteristik des Schwungradspeicher-Prototyps durchgeführt.

Abstract

In this thesis, the mechanical behavior of fiber reinforced filament wound rotors is analyzed that are used for flywheel energy storage systems (FESS). This type of storing electricity is an ecologically and economically sustainable technology for decentralized energy storage with long life cycles without performance degradation depending on depth of discharge and a minimum of systematic maintenance. The main component of a FESS is the high speed rotor, where the major challenge is the maximization of the energy density which depends on the used materials, the geometry of the rotor and the design concept. The complex construction of such rotors requires a computer-aided design process including the knowledge of the material parameters.

The first part of the thesis deals with the material parameter identification used for the ongoing finite element (FE) simulations. Therefore, the elastic and strength material parameters are evaluated. The measurement effort for fiber reinforced materials, especially carbon fiber reinforced plastics (CFRP), is therefore sufficiently higher compared to isotropic materials due to the orthotropic material behavior that differs significantly transverse to the fiber direction. The materials, suitable for the designed FESS rotor, are selected using a new developed nondestructive method, based on modal analysis, to determine the elastic material parameters of fiber reinforced plates. After selection and defining repeatable process parameters for manufacturing, destructive measurements according to standards are performed on high strength and high modulus CFRP materials.

To ensure all safety aspects, the second part of the thesis is dedicated to a flywheel static burst test (FSBT). The presented static test method used for a controlled initiation of a burst event for composite flywheel rotors shows nearly the same stress distribution as in the dynamic case, rotating with maximum speed. Therefore, failure prediction is done using different maximum stress criteria and a safety factor. The static FE simulation results of the FSBT compare well to the quasi-static FE simulation results of the flywheel rotor. Furthermore, it is demonstrated that the presented method is a very good controllable and observable possibility to test a high speed FESS rotor in a static way. Thereby, a much more expensive and dangerous dynamic spin up test with possible uncertainties can be substituted.

Finally, the methods and knowledge from the destructive tests and FSBT are applied to a new FESS rotor design. This design consists of a CFRP hollow shaft that is press-fitted into a multi-ring CFRP inertia mass where the three rings are also press-fitted together forming a rotor with a H-shaped cross-section. With this configuration an increase of the energy density can be achieved compared to an ordinary FESS rotor design using an aluminium shaft press-fitted into a thick wound CFRP inertia mass. Furthermore, measurements are performed on the FESS rotor as well as the built FESS test rig to validate the FE simulations and to measure the FESS characteristics.

Acknowledgments

At this point I would like to address my thanks to the people who have supported me to create this thesis and have made the completion of my doctoral program possible.

A special thanks is given to Univ.Prof. Dipl.-Ing. Dr.techn. Manfred Kaltenbacher, firstly for the excellent scientific support in the context of the thesis and the creation of publications and secondly for the interesting conversations during the work.

I would also like to thank Dipl.-Ing. Dr.techn. Alexander Schulz for his great support and the freedom of design while working together on the project, as well as Dipl.-Ing. Dr.techn. Harald Sima for the valuable suggestions and assistance for problems of any kind.

An extraordinary thanks goes to all colleagues at the Vienna University of Technology at the department of Mechanics and Mechatronics for their great assistance during work, the well done manufacturing and assembling of all needed components and test rigs and the support during complicated measuring tasks.

I want to thank my parents for the free election of my education, giving me the possibility to study and for their unconditional support, at any time and any place. Finally, I want to thank my family and friends for their great support, open ears and helpful hands during difficult times, as well as the strong motivation during my doctoral program.

"Whenever you
find yourself on
the side of the majority
it is time to
pause and reflect."

Mark Twain
1835-1910

Abbreviations

AMB	Active magnetic bearing
BM	Bending mode
CFRP	Carbon fiber reinforced plastic
CLT	Classical lamination theory
CNC	Computer numerical controlled
CS	Clamped support
DAQ	Data acquisition
DC	Direct current
DIC	Digital image correlation
DOD	Depth of discharge
DOF	Degree of freedom
EMA	Experimental modal analysis
FE	Finite element
FEM	Finite element method
FEMA	Finite element modal analysis
FESS	Flywheel energy storage system
FPGA	Field-programmable gate array
FRF	Frequency response function
FRP	Fiber reinforced plastic
FS	Free support
FSBT	Flywheel static burst test
FVT	Forced vibration testing
II	Iterative identification
LSV	Laser scanning vibrometer
MDI	Modified direct identification
M/G	Motor/generator
PCS	Partial clamped support
PID	Proportional-integral-derivative
ROM	Rule of mixture
SEM	Scanning electron microscope
SIMP	Solid isotropic material with penalization
SRM	Switched reluctance motor
TM	Tilting mode
TSE	Total stored energy
UDCFRP	Unidirectional carbon fiber reinforced plastic

Contents

1 Introduction

1.1 Motivation

Flywheel energy storage systems (FESS) represent an ecologically and economically sustainable technology for decentralized energy storage. Long life cycles without performance degradation depending on depth of discharge (DOD) and a minimum of systematic maintenance are key advantages of this technology. The FESS hardware contains the following main parts:

- flywheel rotor consisting of shaft and inertia mass,

- bearings in axial and radial directions,

- motor/generator (M/G) machinery and

- the evacuated safety containment.

The FESS is a mechanical battery that converts electrical into kinetic energy and vice versa. Therefore, if a surplus of electric energy exists, the torque of the motor starts accelerating the flywheel rotor until charging is completed. Afterwards, the FESS stores the kinetic energy of the high speed rotating flywheel rotor as long as self discharge allows it. If there is a demand for electrical energy, the load torque of the generator decelerates the flywheel rotor until the mechanical battery is fully discharged or until the DOD.

The possible long term storage times of FESS depend on the energy needed for levitation summarized by power-, control- and sensor electronics and the rotational losses due to pressure and rotor geometry dependent air friction, the bearing losses and the braking torque of M/G. Therefore, actual FESS show short storage times, typically minutes.

The use of active magnetic bearings (AMB) combined with the operation in an evacuated safety containment reduces rotational losses and furthermore, high energy densities (storage capacity per unit weight) can be achieve using fiber reinforced plastics (FRP). Especially carbon fiber reinforced plastics (CFRP) show a high specific strength ratio, which enable tip speeds up to supersonic speed. This makes this technology attractive again.

The basic principals of FESS started at the early age of industrialization, where flywheels were mostly used to minimize torque fluctuations of steam- and combustion engines. The first idea of a mechanical battery was driven by NASA to power their space missions. In the past decades until today, the need for alternative storage devices becomes stronger and due to increasing climate awareness, decreasing resources and a much more dynamic power grid, this type of technology gets interesting in future.

Research Goal The presented thesis was accomplished within the research project "Optimum-Shape-Flywheel - cost reduction through new designs, rotor geometries and manufacturing techniques" which focuses on the rotor geometry and design to reduce investment costs of FESS. The few currently available flywheels have suboptimal material utilization due to their complex structure and therefore high capital cost. As part of Optimum-Shape-Flywheel research project, innovative approaches to optimal design and the optimum material composition of the central component of any high-efficiency flywheel, the rotor, including the optimal integration of all essential components (M/G, AMB's, etc.) and suitable manufacturing techniques will be developed within a cooperation between the Vienna University of Technology and FWT COMPOSITES & ROLLS GmbH. The much better utilization of strength ("fully-stressed design") and the production optimized structure can on the one hand significantly reduce investment costs and on the other hand improve the overall efficiency, making high efficient flywheels economically viable for a wide range of applications. Following research areas have been studied for this purpose:

- Finite element (FE) based modeling for strength analysis of composite materials with varying ply angle: preparation of complex models for the required prediction of strength and natural frequencies of the Optimum-Shape-Flywheel geometry with consideration of a varying ply angle within the laminate. Implementation of the most suitable failure criterion for composite flywheels. Experimental acquisition of all required material parameters and selecting the best approach.

- Innovative flywheel design with integrated shaft: a completely new flywheel geometry by topology optimization for the best strength utilization ("fully-stressed design") with respect to natural frequencies, thermal behavior and optimal integration of all necessary M/G- and suspension components.

- Manufacturing process for optimal composite topology: production of complex composite structures, optimizing manufacturing precision over manufacturing time, secure integration of metallic inserts, targeted fiber pretension and residual thermal stresses to reduce mechanical stresses in the composite.

- Verification of research results: static test setup for the secure verification of the FE stress calculations. Optimum-Shape-Flywheel measuring setup for total verification of all models, the interaction of all components, the overall efficiency benefit, and the implementation of balancing using AMB's.

The Optimum-Shape-Flywheel technology is thus an essential contribution to the transition to sustainable energy supply with a high proportion of renewable energy.

1.2 State of the Art

1.2.1 Nondestructive Material Parameter Identification

Accurate knowledge of material parameters is necessary to perform precise calculations, especially for composite materials due to their orthotropy. The parameter identification is usually done destructive but if only the elastic material parameters are of interest, a nondestructive method is sufficient.

Within the problematic of modeling plates, there exist a lot of methods that are mostly based on vibrational analysis focused on modal and forced vibration analysis with analytical plate models. There, the boundary conditions define the vibrational behavior of the plate, summarized by the free, simple and clamped supported boundary condition.

The modeling of the mechanical behavior and plate vibration can be made by various approaches including the formulation of the classical plate theory [1], the Reissner-Mindlin plate theory [2, 3, 4], the first-order shear deformation theory [5], the formulation of Hamilton's principal [6] and semi-analytic solutions based on three-dimensional elasticity theory [7]. Finite element simulations are also used to model the free vibrations. In [8] the free vibration of composite cantilevers is studied and in [9] vibration analysis is performed on homogeneous and composite plates. The effect of clamped boundary conditions used for circular plates is studied in [10].

In [11] a nondestructive identification method for rectangular anisotropic plates is discussed. Therein, the natural frequencies and mode shapes are used in combination with the Rayleigh-Ritz method and weighting parameters, obtained by an optimization, to determine the elastic constants. A similar procedure is shown in [12] for thick plates. The direct way without weighting parameters is presented in [13, 14]. There, the modal analysis results of composite plates are used in combination with the principle of virtual displacement to identify the elastic constants. The method in [15] identifies the parameters of quadratic composite plates using the measured natural frequencies and the homogeneous solution of the plates equation of motion.

The elastic constants of anisotropic cantilevers with rectangular cross-section are determined in [16]. In contrast to the already named methods, the elastic constants are derived in a frequency dependent way. The same approach of a complex modulus is used in [17]. Therein, a system identification technique is used in combination of strain data from wave propagation experiments.

A combined experimental and simulation based method is presented in [18, 19, 20]. There, the elastic and damping properties of composite plates and sandwich structures are identified using the results of the modal analysis. The iterative methods minimize the discrepancy between the experimental and numerical modal data derived by higher-order shear deformation theory or by a Rayleigh-Ritz method.

All mentioned methods use a precise measurement setup with an electro-dynamic shaker or loudspeaker for acoustic excitation and a laser scanning vibrometer (LSV). The plate specimen are suspended completely free in a frame by thin wires.

1.2.2 Rotor Analysis and Applications

Literature shows a broad range of analytical calculations for fiber reinforced filament wound rotors used for optimization purpose in many different senses. These are mostly performed quasi-static using an orthotropic linear elastic material model to study the stress distributions of single or multiple material arrangements or combinations and are further used for optimization of the strength ratio or energy density, especially for FESS applications.

The integrated general formulation in [21] is used to study the stress distributions of disc and cylinder like rotors with single and multilayer configuration. Therein, a strong influence of the axial rotor length on stress distribution and moisture absorption was observed. Another important parameter is the stiffness and density of the supporting structure, called hub. The deformation and life analysis of disc like rotors is detailed studied in [22]. The analytical model is capable to perform stress analysis with subject to pressure surface tractions, body forces and interfacial misfits. Furthermore, a representative fatigue/life master curve is shown for a disc application.

A multi-ring composite rotor design to optimize the energy density is shown in [23]. Therein, the used modified generalized plain strain assumption is compared to a full 3D FE simulation. The optimization of a directly wound and press-fitted hybrid composite rotor made of multi-rims with interply and intraply hybrid material formulation as well as the effect of varying winding angles is discussed in [24, 25]. Furthermore, [26] optimizes a composite hub for a hybrid composite rotor. The advantage of press-fitted filament wound flywheel rotors is also presented in [27].

Accurate prediction of the natural frequencies and mode shapes of the rotor are necessary to prevent excessive bearing loss and even catastrophic failure [28]. In [29, 30, 31] the FE method is used to calculate the change in natural frequencies and to perform stress analysis at different rotor speeds. The complexity of general rotor assemblies requires a computer-aided design process. A multi-disciplinary design-optimization procedure for wind turbine blades is discussed in [32, 33]. The modeling of the ferro-magnetic laminated core of motor components is studied in [34]. A detailed overview of several influencing factors, e.g. bearing stiffness and damping, gyroscopic effect, support stiffness, rotor stiffness, notches, unbalance and rotor weight, on the modal characteristics and critical speeds are summarized in [35, 36, 37, 38, 39]. The rotordynamic analysis in [40, 41] shows the modeling of a composite rotor and shaft made of orthotropic material including material damping. In [42] the failure strengths of laminated composite shafts are studied using both theoretical and experimental approaches. The effect of the interference fit on the stiffness of a rotating shaft is discussed in [43].

Successful industrial realized concepts for FESS are depicted in Fig. 1.1, which use an inrunner composite rotor concept that consists of a metal shaft, a filament wound composite rim or ring and a metal hub. A multi- and single-rim composite in combination with a flexible metal hub forming a H-shaped rotor geometry is used in [44, 45, 46]. In contrast, [47, 48, 49] use a single rim composite with a more solid metal hub forming a conventional rectangular rotor geometry.
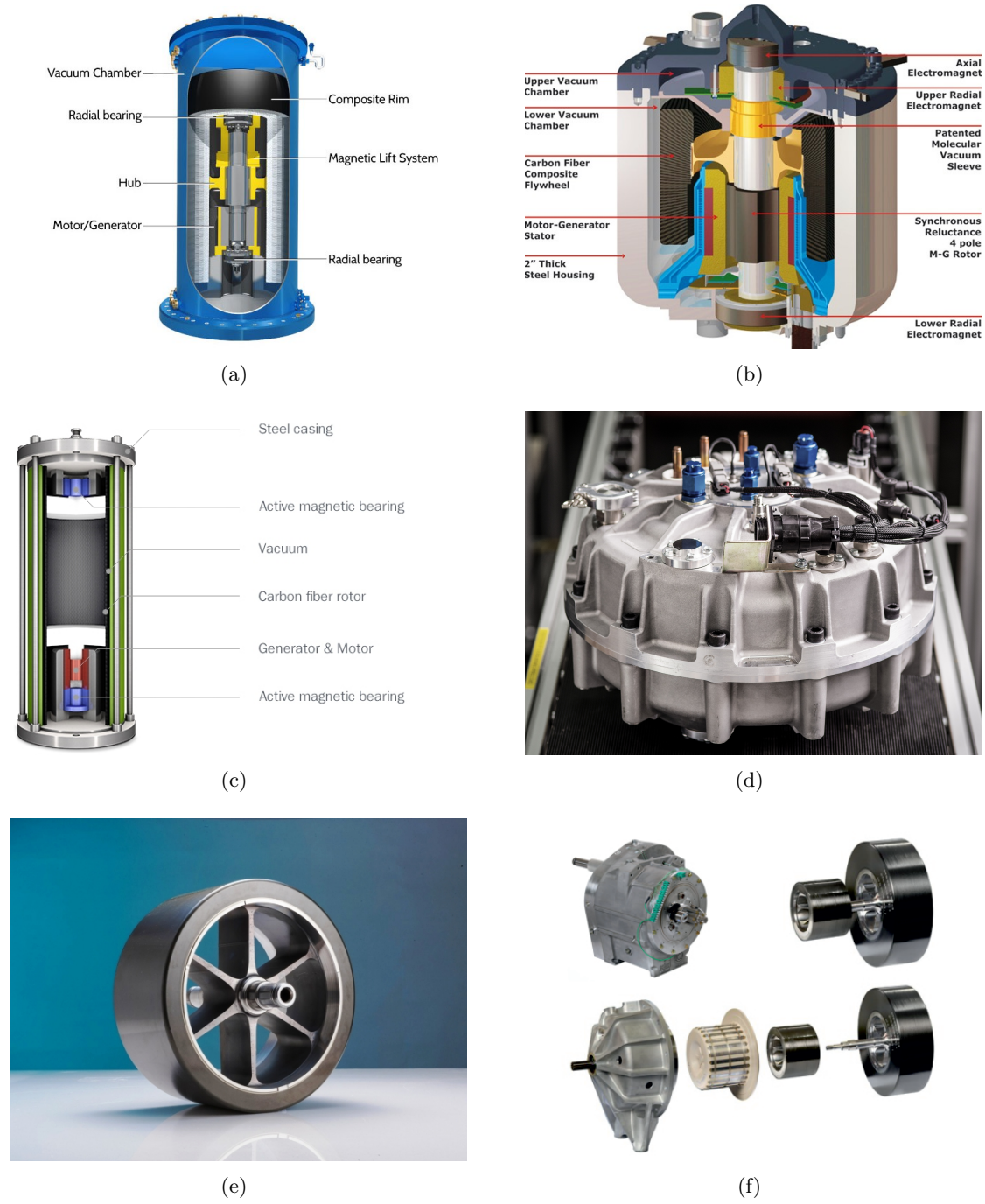
(a)

(b)

(c)

(d)

(e)

(f)

Figure 1.1: State of the art composite rotors for flywheels: (a) Beacon Power Gen4 [44]; (b) PowerTHRU [45]; (c) EnWheel [46];. (d) Gyrodrive [47] ; (e) Flybrid KERS [48]; (f) Flybus [49].

Figure 1.2: Dynamic burst test rigs with highest safety class D [50]: (a) intermediate rotor test inside four steel safety containments; (b) heavy duty rotor test inside a tunnel of $3\,\mathrm{m}$ thick reinforced concrete.

1.2.3 Burst Tests for Rotor Applications

High rotational speeds cause high kinetic energy and so fragments of the rotor can do serious damage to structures and people in case of a burst event. To compensate for possible unknowns, e.g. the real fiber volume fraction, voids or manufacturing imperfections due to the filament winding process, a conservative safety factor for calculation is usually used. The goal is to reduce this safety factor to use the full capability of the material. Hence, a burst test under controlled conditions is necessary to ensure a safe operation. A standard procedure to test the composite part of a rotor is a dynamic spin up under operating conditions till a burst event occurs. On one hand this causes immense costs for testing and on the other hand it is critical with regards to safety and should be avoided.

Therefore, other methods for the burst test have been developed. In [50, 51, 52, 53, 54, 55], the composite rotor is mounted in a proper spin test system that is evacuated for the purpose of dust explosions and to lower the driving power, see Fig. 1.2. The one-sided bearing in [56] can be disadvantageous in case of large rotors, because of the changed rotordynamic behavior and possible unbalance forces during spin up. A similar setup can be used to test disk and cylinder like composite rotors [57, 24, 26]. In [58, 59] a test method for the evaluation of CFRP materials is described. In both setups an elastic-plastic hub is used to drive the CFRP rotor to the burst event. A main disadvantage of a dynamic spin test is the reduced controllability and observability of the burst event compared to a static burst test.

The major challenge of static testing is the application of loads sufficiently similar to inertia loads arising due to the rotation, which is typically not possible. A test to burst hoop filament wounded rings is presented in [60, 61, 62]. Similar tests to burst hoop wounded and angle ply tubes are shown in [63, 64, 65, 66]. These hydroburst test methods use pressure applied by temperature rise or explosive charge on the inside to expand and thereby burst the rings or tubes.

1.3 Structure of the Dissertation

The analysis of fiber reinforced filament wound rotors, presented hereinafter, starts hierarchical from the material parameter identification, goes on with FE simulations and optimizations for the rotor and ends with several experimental measurements to validate FE simulations accomplished on a rotor application example for a FESS. The dissertation is structured as follows:

- Chapter 2 covers the mechanical field equations needed for FE simulations and some basic principles about fiber reinforced composites focused on material modeling and failure analysis.

- Chapter 3 is devoted to the material parameter identification used for ongoing FE simulations. Therefore, the elastic parameters used for the material model as well as the strength parameters for the failure analysis are evaluated. This is firstly performed experimentally by a nondestructive method (elastic parameters only) using modal analysis of rectangular plates and secondly by a destructive method using ordinary tension-, compression- and bending tests according to standards.

- Chapter 4 deals with a static burst test for composite flywheel rotors. This method is developed to substitute a more dangerous and expensive dynamic spin up test and is further applied to an optimized inertia mass followed by an analysis of the burst fragments.

- Chapter 5 shows the design and optimization of a composite rotor for a FESS. The main focus lies on the completely new design of the FESS rotor that consists of a CFRP hollow shaft with sections of different winding angles and a hoop wound hybrid multi-ring, press-fitted inertia mass with a H-shaped cross-section. Furthermore, experiments using modal analysis and the FESS test rig were performed to validate FE simulations.

2 Structural Mechanics

2.1 Mechanical Field

The mechanical field is derived using the idea of a solid body at its equilibrium. Now, we cut a small part Ω out of this solid body and the so arising faces Γ are loaded by mechanical stresses $[\boldsymbol{\sigma}]$ (force per unit area) to still guarantee equilibrium. These stresses are introduced using the Cauchy stress tensor formulated as

$$[\boldsymbol{\sigma}] = \begin{bmatrix} \sigma_{xx} & \sigma_{xy} & \sigma_{xz} \\ \sigma_{yx} & \sigma_{yy} & \sigma_{yz} \\ \sigma_{zx} & \sigma_{zy} & \sigma_{zz} \end{bmatrix} . \tag{2.1}$$

The above defined stress state in combination with the acting volume forces $\boldsymbol{f}_V$ establish the state of equilibrium that is described firstly by the force balance

$$\int_\Omega \boldsymbol{f}_V \, d\Omega + \oint_\Gamma [\boldsymbol{\sigma}]^T \, d\boldsymbol{\Gamma} = 0 , \tag{2.2}$$

and secondly by the moment balance

$$\int_\Omega (\boldsymbol{r} \times \boldsymbol{f}_V) \, d\Omega + \oint_\Gamma \left(\boldsymbol{r} \times [\boldsymbol{\sigma}]^T \right) d\boldsymbol{\Gamma} = 0 . \tag{2.3}$$

Applying the divergence theorem and using the relation $[\boldsymbol{\sigma}] = [\boldsymbol{\sigma}]^T$, detailed explained in [67], results in the equilibrium equation

$$\boldsymbol{f}_V + \boldsymbol{\nabla} [\boldsymbol{\sigma}] = 0 , \tag{2.4}$$

where the stress tensor $[\boldsymbol{\sigma}]$ is expressed in a more convenient form, called Voigt notation to

$$\boldsymbol{\sigma} = \begin{pmatrix} \sigma_{xx} & \sigma_{yy} & \sigma_{zz} & \sigma_{yz} & \sigma_{xz} & \sigma_{xy} \end{pmatrix}^T . \tag{2.5}$$

The use of the differential operator $\mathcal{B}$

$$\mathcal{B} = \begin{pmatrix} \frac{\partial}{\partial x} & 0 & 0 & 0 & \frac{\partial}{\partial z} & \frac{\partial}{\partial y} \\ 0 & \frac{\partial}{\partial y} & 0 & \frac{\partial}{\partial z} & 0 & \frac{\partial}{\partial x} \\ 0 & 0 & \frac{\partial}{\partial z} & \frac{\partial}{\partial y} & \frac{\partial}{\partial x} & 0 \end{pmatrix}^T , \tag{2.6}$$
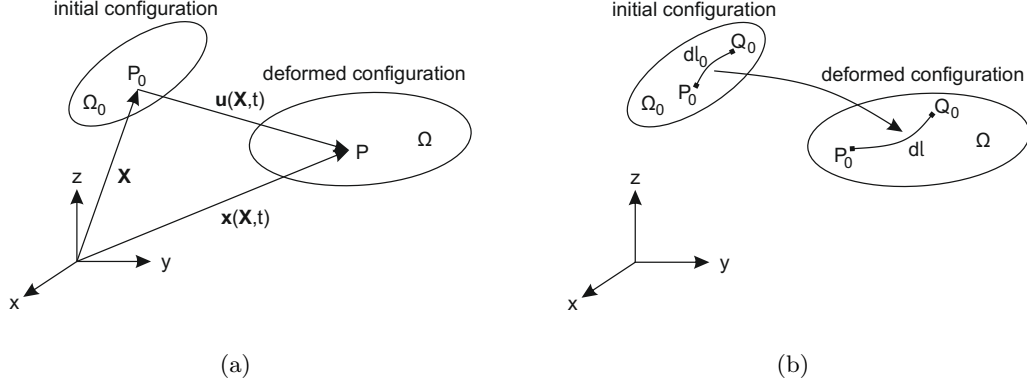
Figure 2.1: Initial Ω_0 and deformed configuration Ω of a body [67]: (a) vectors of material point; (a) strain measurement.

rewrites the equilibrium equation to

$$\boldsymbol{f}_V + \mathcal{B}^T \boldsymbol{\sigma} = 0 \ . \tag{2.7}$$

In the non-static case, described by Newton's second law, the inertial loads due to acceleration $\boldsymbol{a}$ are equal to the sum of all body forces

$$\boldsymbol{f}_V + \mathcal{B}^T \boldsymbol{\sigma} = \rho \boldsymbol{a} \ , \tag{2.8}$$

where ρ is the density of the body. The relation between material point $\boldsymbol{X}$ of an initial configuration Ω_0 and the point $\boldsymbol{x}$ of the deformed configuration is given by the unique map $\boldsymbol{\Phi}$ to $\boldsymbol{x} = \boldsymbol{\Phi}(\boldsymbol{X}, t)$, see Fig. 2.1(a). The difference of these points defines the displacement vector

$$\boldsymbol{u}(\boldsymbol{X}, t) = \boldsymbol{x} - \boldsymbol{X} = \boldsymbol{\Phi}(\boldsymbol{X}, t) - \boldsymbol{X} \ . \tag{2.9}$$

By using the deformation gradient $[\boldsymbol{F}_d]$, which maps a differential line element $d\boldsymbol{X}$ in Ω_0 to the corresponding differential line element $d\boldsymbol{x}$ in Ω

$$d\boldsymbol{x} = [\boldsymbol{F}_d]\, d\boldsymbol{X} = \frac{\partial \boldsymbol{x}}{\partial \boldsymbol{X}} = \boldsymbol{\nabla}_X \boldsymbol{\Phi} \ , \tag{2.10}$$

and the above given displacement vector, the deformation gradient gets the form

$$[\boldsymbol{F}_d] = \boldsymbol{\nabla}_X \left(\boldsymbol{X} + \boldsymbol{u}\right) = \boldsymbol{I} + \boldsymbol{\nabla}_X \boldsymbol{u} = \boldsymbol{I} + \begin{bmatrix} \frac{\partial u_x}{\partial X} & \frac{\partial u_x}{\partial Y} & \frac{\partial u_x}{\partial Z} \\ \frac{\partial u_y}{\partial X} & \frac{\partial u_y}{\partial Y} & \frac{\partial u_y}{\partial Z} \\ \frac{\partial u_z}{\partial X} & \frac{\partial u_z}{\partial Y} & \frac{\partial u_z}{\partial Z} \end{bmatrix} \ . \tag{2.11}$$

The change of the line elements dl_0 and dl between two arbitrarily points in the initial (P_0, Q_0) and deformed (P, Q) configuration is used to derive the relation between the mechanical strain and displacement, see Fig. 2.1(b). The difference of the square of both differential line elements in combination with the deformation gradient expresses as follows

$$
\begin{aligned}
dl^2 - dl_0^2 &= d\boldsymbol{x}^T d\boldsymbol{x} - d\boldsymbol{X}^T d\boldsymbol{X} \\
&= d\boldsymbol{X}^T \left[\boldsymbol{F}_d\right]^T \left[\boldsymbol{F}_d\right] d\boldsymbol{X} - d\boldsymbol{X}^T d\boldsymbol{X} \\
&= d\boldsymbol{X}^T \left(\left[\boldsymbol{F}_d\right]^T \left[\boldsymbol{F}_d\right] - \boldsymbol{I}\right) d\boldsymbol{X} \\
&= d\boldsymbol{X}^T 2 \left[\boldsymbol{V}\right] d\boldsymbol{X} \ ,
\end{aligned}
\tag{2.12}
$$

where $[\boldsymbol{V}]$ denotes the Green-Lagrangian strain tensor that is further given by the relation $[\boldsymbol{F}_d] = \boldsymbol{I} + \boldsymbol{\nabla}_X \boldsymbol{u}$

$$
\begin{aligned}
\left[\boldsymbol{V}\right] &= \frac{1}{2} \left(\left(\boldsymbol{I} + \boldsymbol{\nabla}_X \boldsymbol{u}\right)^T \left(\boldsymbol{I} + \boldsymbol{\nabla}_X \boldsymbol{u}\right) - \boldsymbol{I}\right) \\
&= \frac{1}{2} \left(\boldsymbol{\nabla}_X \boldsymbol{u} + (\boldsymbol{\nabla}_X \boldsymbol{u})^T\right) + \frac{1}{2} \left((\boldsymbol{\nabla}_X \boldsymbol{u})^T \boldsymbol{\nabla}_X \boldsymbol{u}\right) \ .
\end{aligned}
\tag{2.13}
$$

In case of small deflections only the linear part of $[\boldsymbol{V}]$ is used that results in the tensor of linear strains

$$
\left[\boldsymbol{\varepsilon}\right] = \frac{1}{2} \left(\boldsymbol{\nabla}_X \boldsymbol{u} + (\boldsymbol{\nabla}_X \boldsymbol{u})^T\right) \ ,
\tag{2.14}
$$

that is further introduced in Voigt vector notation using the shear deformation angle γ

$$
\boldsymbol{\varepsilon} =
\begin{bmatrix}
\frac{\partial u_x}{\partial X} \\
\frac{\partial u_y}{\partial Y} \\
\frac{\partial u_z}{\partial Z} \\
\left(\frac{\partial u_y}{\partial Z} + \frac{\partial u_z}{\partial Y}\right) \\
\left(\frac{\partial u_z}{\partial X} + \frac{\partial u_x}{\partial Z}\right) \\
\left(\frac{\partial u_x}{\partial Y} + \frac{\partial u_y}{\partial X}\right)
\end{bmatrix}
=
\begin{pmatrix}
\varepsilon_{xx} \\
\varepsilon_{yy} \\
\varepsilon_{zz} \\
2\varepsilon_{yz} \\
2\varepsilon_{xz} \\
2\varepsilon_{xy}
\end{pmatrix}
=
\begin{pmatrix}
\varepsilon_{xx} \\
\varepsilon_{yy} \\
\varepsilon_{zz} \\
\gamma_{yz} \\
\gamma_{xz} \\
\gamma_{xy}
\end{pmatrix} \ .
\tag{2.15}
$$

Hook's law, the linear relation between stress and strain, is used for linear elasticity computations which reads in Voigt notation as

$$
\boldsymbol{\sigma} = \boldsymbol{E}\boldsymbol{\varepsilon} \ ,
\tag{2.16}
$$

for a general anisotropic 4th order elasticity tensor $\boldsymbol{E}$. Furthermore, using the relation $\boldsymbol{\varepsilon} = \mathcal{B}\boldsymbol{u}$, Newton's second law can be rewritten and the so called strong formulation, without specified boundary conditions, for linear elasticity problems reads as

$$
\boldsymbol{f}_V + \mathcal{B}^T \boldsymbol{E} \mathcal{B} \boldsymbol{u} = \rho \frac{\partial^2 \boldsymbol{u}}{\partial t^2} \ .
\tag{2.17}
$$

2.2 Finite Element Formulation

Linear Elasticity The numerical computation is performed using the finite element method (FEM) to solve the partial differential equation (2.17) for linear elasticity problems.

In first, the so called weak formulation is derived. Therefore, the strong formulation is multiplied by an appropriate test function $\boldsymbol{u}'$ and the second term is integrated by parts [67]. The weak formulation for linear elasticity problems in the computational domain Ω reads as

$$\int_\Omega \rho \boldsymbol{u}' \cdot \frac{\partial^2 \boldsymbol{u}}{\partial t^2} d\Omega + \int_\Omega (\mathcal{B}\boldsymbol{u}')^T \boldsymbol{E}\mathcal{B}\boldsymbol{u} d\Omega = \int_\Omega \boldsymbol{u}' \cdot \boldsymbol{f}_V d\Omega \ . \tag{2.18}$$

The continuous displacement $\boldsymbol{u}$ is now approximated by nodal finite elements to perform the spatial discretization as follows

$$\boldsymbol{u} \approx \boldsymbol{u}^h = \sum_{i=1}^{n_d} \sum_{a=1}^{n_n'} N_a u_{ia} \boldsymbol{e}_i = \sum_{a=1}^{n_n'} \boldsymbol{N}_a \boldsymbol{u}_a \ , \tag{2.19}$$

$$\boldsymbol{N}_a = \begin{pmatrix} N_a & 0 & 0 \\ 0 & N_a & 0 \\ 0 & 0 & N_a \end{pmatrix} \ , \tag{2.20}$$

where n_d denotes the space dimension, N_a appropriate basis functions for discretization and n_n' the number of finite element nodes with no Dirichlet boundary condition.

In second, the semidiscrete Galerkin formulation is derived. Therefore, the continuous displacement as well as the test function $\boldsymbol{u}'$ are approximated according to (2.19) and substituted into (2.18), which results in

$$\sum_{a=1}^{n_n'} \sum_{b=1}^{n_n'} \left(\int_\Omega \rho \boldsymbol{N}_a^T \boldsymbol{N}_b d\Omega \frac{\partial^2 \boldsymbol{u}_b}{\partial t^2} + \int_\Omega (\mathcal{B}_a^u)^T \boldsymbol{E}\mathcal{B}_b^u d\Omega \boldsymbol{u}_b - \int_\Omega \boldsymbol{N}_a^T \boldsymbol{f}_V(\boldsymbol{r}_a) d\Omega \right) = 0 \ , \tag{2.21}$$

with

$$\mathcal{B}_a^u = \begin{pmatrix} \frac{\partial N_a}{\partial x} & 0 & 0 & 0 & \frac{\partial N_a}{\partial z} & \frac{\partial N_a}{\partial y} \\ 0 & \frac{\partial N_a}{\partial y} & 0 & \frac{\partial N_a}{\partial z} & 0 & \frac{\partial N_a}{\partial x} \\ 0 & 0 & \frac{\partial N_a}{\partial z} & \frac{\partial N_a}{\partial y} & \frac{\partial N_a}{\partial x} & 0 \end{pmatrix}^T \ . \tag{2.22}$$

The system of ordinary differential equations in time (2.21) is further written in matrix form to

$$\boldsymbol{M}_u \underline{\ddot{u}} + \boldsymbol{K}_u \underline{u} = \underline{f} \ , \tag{2.23}$$

with the mass matrix $\boldsymbol{M}_u$, the stiffness matrix $\boldsymbol{K}_u$, the vector of unknowns $\underline{u}$, it's second time derivative $\underline{\ddot{u}}$ and the load vector $\underline{f}$ that are all assembled from the element matrices
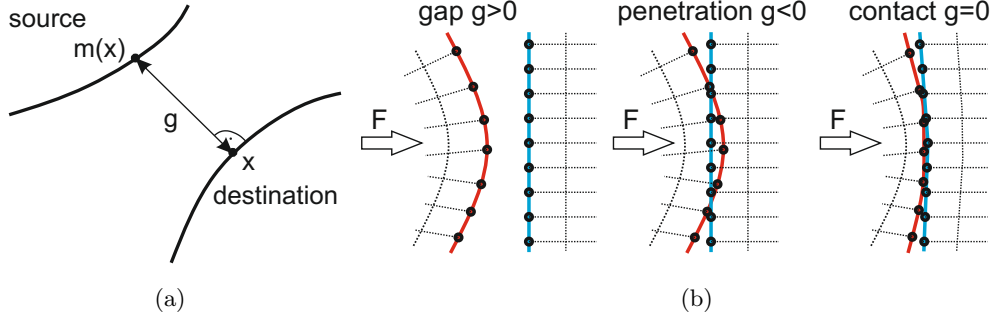
Figure 2.2: Multi-body contact: (a) gap definition [68]; (b) gap-, penetration- and contact state.

and vectors calculated in the element volume Ω^e by

$$\boldsymbol{M}_u = \bigwedge_{e=1}^{n_e} \boldsymbol{m}_u^e \; ; \; \boldsymbol{m}_u^e = [\boldsymbol{m}_{pq}] \; ; \; \boldsymbol{m}_{pq} = \int_{\Omega^e} \rho \boldsymbol{N}_p^T \boldsymbol{N}_q d\Omega \; , \tag{2.24}$$

$$\boldsymbol{K}_u = \bigwedge_{e=1}^{n_e} \boldsymbol{k}_u^e \; ; \; \boldsymbol{k}_u^e = [\boldsymbol{k}_{pq}] \; ; \; \boldsymbol{k}_{pq} = \int_{\Omega^e} \left(\mathcal{B}_p^u\right)^T \boldsymbol{E}\mathcal{B}_q^u d\Omega \; , \tag{2.25}$$

$$\underline{f} = \bigwedge_{e=1}^{n_e} \underline{f}^e \; ; \; \underline{f}^e = \left[\underline{f}_p\right] \; ; \; \underline{f}_p = \int_{\Omega^e} \boldsymbol{N}_p^T \boldsymbol{f}_V(\boldsymbol{r}_p) d\Omega \; . \tag{2.26}$$

Furthermore, the damping $\boldsymbol{C}_u$ is introduced as Rayleigh damping [67]

$$\boldsymbol{C}_u = \alpha \boldsymbol{M}_u + \beta \boldsymbol{K}_u \; , \tag{2.27}$$

where α denotes the mass proportional and β the stiffness proportional damping coefficient. The semidiscrecte Galerkin formulation including damping reads as

$$\boldsymbol{M}_u \underline{\ddot{u}} + \boldsymbol{C}_u \underline{\dot{u}} + \boldsymbol{K}_u \underline{u} = \underline{f} \; . \tag{2.28}$$

Non-linear Case: Contact Mechanical structures are often assembled by multiple parts that are somehow fitted together. Hence, there are multi-body contacts present that drive a linear system non-linear. Furthermore, also single body contact is possible that is not further discussed. For contact modeling using a FE software, e.g. [68, 69] one needs to distinguish between the source and the destination, see Fig. 2.2(a).

The contact formulation described in [68] uses an augmented Lagrangian method. Therefore, the software needs to solve the multi-body contact in a segregated way. The augmentation components are introduced as the contact pressure T_n and the not further discussed components T_{ti} of the friction traction vector T_t. Therefore, an additional iteration level is added where the displacement variables are solved separately from the contact pressure and traction variables. This procedure is repeated until a convergence
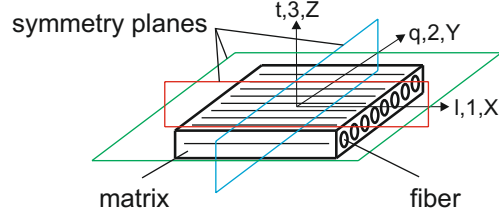
Figure 2.3: A unidirectional fiber-reinforced composite layer.

criterion is fulfilled. This method needs more iterations compared to a pure penalty method but is independent of contact stiffness and penetration depth.

The gap distance g between source and destination is used to derive the penalized contact pressure T_{np} that is defined on the destination boundary by

$$T_{np} = \begin{cases} T_n - p_n g & \text{if } g \leq 0 \\ T_n e^{-\frac{p_n g}{T_n}} & \text{otherwise} \end{cases}, \tag{2.29}$$

where p_n is the defined normal penalty factor. During iterations, the contact states open, penetration and closed are present, see Fig. 2.2(b).

2.3 Mechanics of Composite Materials

Composite materials are a combination of minimum two constituents on the macroscopic scale such that the performance compared to conventional materials is graded. The most common properties, essential for rotors, are the stiffness and strength as well as its weight reduction.

The composite material we deal with is made of two materials: a reinforcement material called fiber and a supporting material, called matrix. Furthermore, the composite made from wet filament winding is of the type continuous fiber reinforced plastics, where the used matrix is epoxy resin.

Composites are inherently heterogeneous from the microscopic point of view, but when lamina or plies are treated from the macroscopic point of view, wherein the lamina is a continuum with material properties derived from a weighted average of the constituents, fiber and matrix, the assumption of a homogeneous material is valid. Hence, the generalized Hooke's law (2.16) can be used to describe the mechanical properties of the composite material.

Orthotropic Material Behavior   The unidirectional, continuous fiber-reinforced lamina is treated as an orthotropic material with symmetry planes parallel and transverse to the fiber direction, see Fig. 2.3.

The micromechanics mean-field approach, the rules of mixture (ROM) by Voigt and

Reuss or Mori-Tanaka's theory [70, 71], to estimate the engineering constants of a lamina is based on the following assumptions [72]:

- perfect bonding between fibers and matrix,

- parallel and uniformly distributed fibers,

- the matrix is free of voids, microcracks and pre-stresses,

- fibers and matrix are isotropic (false for carbon fibers but accepted) and

- the applied loads are either parallel or transverse to the fiber direction.

When using the ROM, the moduli and Poisson's ratio of a continuous fiber reinforced material can be estimated in terms of the moduli, Poisson's ratios and volume fractions of the constituents by

$$E_1 = E_f v_f + E_m v_m \ , \quad \nu_{12} = \nu_f v_f + \nu_m v_m \ ,$$
$$E_2 = \frac{E_f E_m}{E_f v_m + E_m v_f} \ , \quad G_{12} = \frac{G_f G_m}{G_f v_m + G_m v_f} \ , \tag{2.30}$$

where E_1, E_2, ν_{12} and G_{12} denote the longitudinal modulus, the transverse modulus, the major Poissons' ratio and the shear modulus with the parameter of the constituents

$$\begin{aligned}
E_f &= \text{modulus of the fiber}, & E_m &= \text{modulus of the matrix}, \\
\nu_f &= \text{Poisson's ratio of the fiber}, & \nu_m &= \text{Poisson's ratio of the matrix}, \\
v_f &= \text{fiber volume fraction}, & v_m &= \text{matrix volume fraction},
\end{aligned}$$

$$G_f = \frac{E_f}{2(1 + \nu_f)} \ , \quad G_m = \frac{E_m}{2(1 + \nu_m)} \ . \tag{2.31}$$

The engineering parameters E_1, E_2, E_3, G_{12}, G_{13}, G_{23}, ν_{12}, ν_{13} and ν_{23} of an orthotropic material need to be determined experimentally by tension-, compression- and bending tests using appropriate test specimen made of several layers of the composite material.

With these parameters, the linear elastic orthotropic material model, described by the elasticity tensor $\boldsymbol{E}$

$$\boldsymbol{E} = \begin{bmatrix}
\frac{1}{E_1} & \frac{-\nu_{12}}{E_1} & \frac{-\nu_{13}}{E_1} & 0 & 0 & 0 \\
 & \frac{1}{E_2} & \frac{-\nu_{23}}{E_2} & 0 & 0 & 0 \\
 & & \frac{1}{E_3} & 0 & 0 & 0 \\
 & & & \frac{1}{G_{23}} & 0 & 0 \\
 & \text{sym.} & & & \frac{1}{G_{13}} & 0 \\
 & & & & & \frac{1}{G_{12}}
\end{bmatrix}^{-1} \ , \tag{2.32}$$

is found, that is used in the semidiscrete Galerkin formulation (2.28) to calculate the stiffness matrix $\boldsymbol{K}_u$.
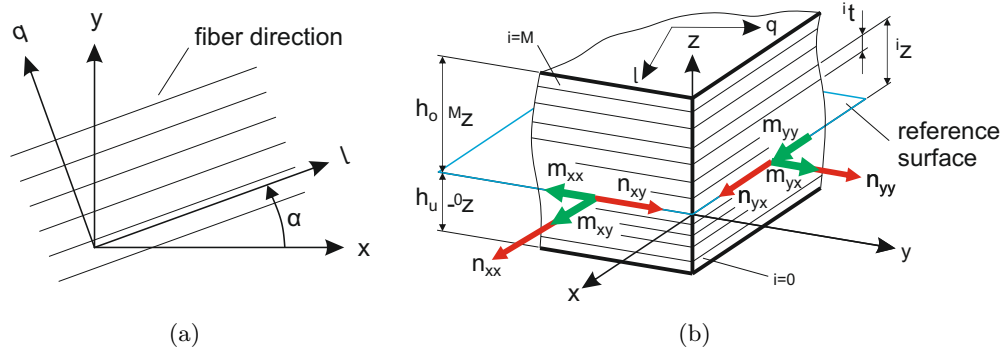
Figure 2.4: Classical laminated plate theory: (a) local l,q- and global x,y-coordinate system; (b) geometry of ply stack forming a laminate.

Classical Laminated Plate Theory   The theory is an extension of the classical plate theory to composite laminates where also the assumption of Kirchhoff's hypothesis holds [72]:

- straight lines perpendicular to the midsurface before deformation remain straight after deformation,

- the transverse normals do not experience elongation and

- the transverse normals rotate such that they remain perpendicular to the midsurface after deformation.

The plain-stress theory starts defining Hooke's law in the local l,q-coordinate system, see Fig. 2.4(a)

$$^i\boldsymbol{\sigma}_L = {}^i\boldsymbol{E}_L\,{}^i\boldsymbol{\varepsilon}_L \ , \tag{2.33}$$

where i denotes the ply number and L is the identifier for the local coordinate system where the orthotropic elasticity tensor $\boldsymbol{E}_L$ is defined. Since the further on defined membrane forces and bending moments are linked with the global strains ${}^i\boldsymbol{\varepsilon}$, the local components, that can differ from ply to ply, need to be transformed in a uniformly global x,y-coordinate system (identifier G). This is applied to the stress and strain [72]

$$^i\boldsymbol{\sigma}_L = {}^i\boldsymbol{T}\,{}^i\boldsymbol{\sigma}_G \ , \ \ ^i\boldsymbol{\varepsilon}_L = {}^i\boldsymbol{T}^{-T}\,{}^i\boldsymbol{\varepsilon}_G \ , \tag{2.34}$$

using the transformation matrix ${}^i\boldsymbol{T}$ with $c = \cos {}^i\alpha$ and $s = \sin {}^i\alpha$

$$^i\boldsymbol{T} = {}^i\begin{bmatrix} c^2 & s^2 & 2cs \\ s^2 & c^2 & -2cs \\ -sc & sc & c^2 - s^2 \end{bmatrix} \ , \tag{2.35}$$

15

that further results in Hooke's law transformed into the global x,y-coordinate system

$$^{i}\boldsymbol{\sigma}_G = {}^{i}\boldsymbol{E}_G{}^{i}\boldsymbol{\varepsilon}_G = {}^{i}\boldsymbol{T}^{-1}{}^{i}\boldsymbol{E}_L{}^{i}\boldsymbol{T}^{-T}{}^{i}\boldsymbol{\varepsilon}_G \ . \tag{2.36}$$

The stacked laminate is depicted in Fig. 2.4(b). Therein, the membrane forces n_{kl} and bending moments m_{kl} are shown that calculates to

$$n_{kl} = \int_{-h_u}^{h_o} \sigma_{kl}(z)dz \approx \sum_{i=1}^{M} {}^{i}\sigma_{kl}({}^{i}z - {}^{i-1}z) \ ,$$

$$m_{kl} = -\int_{-h_u}^{h_o} \sigma_{kl}(z)zdz \approx -\sum_{i=1}^{M} {}^{i}\sigma_{kl}({}^{i}z - {}^{i-1}z)\frac{{}^{i}z + {}^{i-1}z}{2} \ ,$$

$$\boldsymbol{n}_G = (n_{xx}, \ n_{yy}, \ n_{xy})^T = \sum_{i=1}^{M} {}^{i}\boldsymbol{\sigma}_G({}^{i}z - {}^{i-1}z) \ , \tag{2.37}$$

$$\boldsymbol{m}_G = (m_{xx}, \ m_{yy}, \ m_{xy})^T = -\sum_{i=1}^{M} {}^{i}\boldsymbol{\sigma}_G\frac{{}^{i}z^2 - {}^{i-1}z^2}{2} \ . \tag{2.38}$$

with the distances from the reference surface h_o and h_u and M is the total number of plies in the laminate. The Kirchhoff's assumptions lead to the following kinematic relations for the displacements $(u, \ v, \ w)$

$$u = \bar{u} - z\frac{\partial w}{\partial x} \ , \ v = \bar{v} - z\frac{\partial w}{\partial y} \ , \ \boldsymbol{\varepsilon}_G = \bar{\boldsymbol{\varepsilon}} - z\boldsymbol{\kappa} \ , \tag{2.39}$$

where $\bar{\varepsilon}$ and $\boldsymbol{\kappa}$ denote the strains in the reference surface and the curvatures defined by

$$\bar{\boldsymbol{\varepsilon}} = \left(\frac{\partial\bar{u}}{\partial x}, \ \frac{\partial\bar{v}}{\partial y} \ \frac{\partial\bar{u}}{\partial y} + \frac{\partial\bar{v}}{\partial x}\right)^T \ , \ \boldsymbol{\kappa} = \left(\frac{\partial^2 w}{\partial x^2}, \ \frac{\partial^2 w}{\partial y^2}, \ 2\frac{\partial^2 w}{\partial x\partial y}\right)^T \ . \tag{2.40}$$

When combining the above given relations for the global strain $\boldsymbol{\varepsilon}_G$ with (2.37) and (2.38) the following relations for the membrane forces

$$\boldsymbol{n}_G = \sum_{i=1}^{M} {}^{i}\boldsymbol{E}_G({}^{i}z - {}^{i-1}z)\bar{\boldsymbol{\varepsilon}} - \sum_{i=1}^{M} {}^{i}\boldsymbol{E}_G\frac{{}^{i}z^2 - {}^{i-1}z^2}{2}\boldsymbol{\kappa} = \boldsymbol{A}\bar{\boldsymbol{\varepsilon}} + \boldsymbol{B}\boldsymbol{\kappa} \tag{2.41}$$

and the bending moments

$$\boldsymbol{m}_G = -\sum_{i=1}^{M} {}^{i}\boldsymbol{E}_G\frac{{}^{i}z^2 - {}^{i-1}z^2}{2}\bar{\boldsymbol{\varepsilon}} + \sum_{i=1}^{M} {}^{i}\boldsymbol{E}_G\frac{{}^{i}z^3 - {}^{i-1}z^3}{3}\boldsymbol{\kappa} = \boldsymbol{B}\bar{\boldsymbol{\varepsilon}} + \boldsymbol{D}\boldsymbol{\kappa} \tag{2.42}$$

result that are finally summarized in the linear elastic material law for a laminate

$$\begin{bmatrix} \boldsymbol{n}_G \\ \boldsymbol{m}_G \end{bmatrix} = \begin{bmatrix} \boldsymbol{A} & \boldsymbol{B} \\ \boldsymbol{B} & \boldsymbol{D} \end{bmatrix} \begin{bmatrix} \bar{\boldsymbol{\varepsilon}} \\ \boldsymbol{\kappa} \end{bmatrix} \ . \tag{2.43}$$

Failure Prediction In contrast to linear elastic isotropic materials, where failure is predicted by e.g. von Mises or Tresca criterion, composite materials need special investigation for failure prediction. Therefore, many failure criteria exist that are separated in criteria that consider interactions between stress components (Hill, Tsai/Hill, Hoffman, Tsai-Wu, etc.) and those who do not (maximum stress and maximum strain).

In the following, the maximum stress and Tsai-Wu [73] failure criteria are described for failure prediction of an orthotropic composite material. In the maximum stress criterion, failure occurs if any of the following conditions is satisfied

$$R_1^t = \frac{\sigma_{ll}}{X_t} \geq 1 \ , \ R_2^t = \frac{\sigma_{qq}}{Y_t} \geq 1 \ ,$$

$$R_3^t = \frac{\sigma_{tt}}{Z_t} \geq 1 \ , \ R_1^c = \left| -\frac{\sigma_{ll}}{X_c} \right| \geq 1 \ ,$$

$$R_2^c = \left| -\frac{\sigma_{qq}}{Y_c} \right| \geq 1 \ , \ R_3^c = \left| -\frac{\sigma_{tt}}{Z_c} \right| \geq 1 \ ,$$

$$R_4 = \left| \frac{\sigma_{qt}}{S_{23}} \right| \geq 1 \ , \ R_5 = \left| \frac{\sigma_{lt}}{S_{13}} \right| \geq 1 \ , \ R_6 = \left| \frac{\sigma_{lq}}{S_{12}} \right| \geq 1 \ , \tag{2.44}$$

where (X_t, Y_t, Z_t) are the lamina normal strength in tension (t) and (X_c, Y_c, Z_c) are the normal strength in compression (c) along the (1, 2, 3) directions and (S_{12}, S_{13}, S_{23}) are the shear strengths in the (12, 13, 23) planes, respectively.

The Tsai-Wu criterion, where the failure is predicted using a scalar failure parameter R_{TW}, is derived as follows

$$R_{TW} = \overline{\boldsymbol{F}}^T \boldsymbol{\sigma}_L + \boldsymbol{\sigma}_L^T \widetilde{\boldsymbol{F}} \boldsymbol{\sigma}_L \geq 1 \ , \tag{2.45}$$

with the stress state $\boldsymbol{\sigma}_L = (\sigma_{ll} \ \sigma_{qq} \ \sigma_{tt} \ \sigma_{qt} \ \sigma_{lt} \ \sigma_{lq})^T = (\sigma_{11} \ \sigma_{22} \ \sigma_{33} \ \sigma_{23} \ \sigma_{13} \ \sigma_{12})^T$ and the second and fourth order tensor of the strength parameters given as follows

$$\bar{\boldsymbol{F}} = (F_1, F_2, F_3, F_4, F_5, F_6)^T \ , \tag{2.46}$$

$$\widetilde{\boldsymbol{F}} = \begin{bmatrix} F_{11} & F_{12} & F_{13} & F_{14} & F_{15} & F_{16} \\ & F_{22} & F_{23} & F_{24} & F_{25} & F_{26} \\ & & F_{33} & F_{34} & F_{35} & F_{36} \\ & & & F_{44} & F_{45} & F_{46} \\ & sym. & & & F_{55} & F_{56} \\ & & & & & F_{66} \end{bmatrix} . \tag{2.47}$$

Due to the orthotropic material behavior, no coupling between the normal and shear stress terms and between the shear terms are assumed. This leads to

$$F_4 = F_5 = F_6 = 0$$
$$F_{14} = F_{15} = F_{16} = F_{24} = F_{25} = F_{26} = 0$$
$$F_{34} = F_{35} = F_{36} = F_{45} = F_{46} = F_{56} = 0 \ . \tag{2.48}$$

Hence, (2.45) reads as

$$
\begin{aligned}
R_{TW} =\ & F_1\sigma_{11} + F_2\sigma_{22} + F_3\sigma_{33} \\
& + F_{11}\sigma_{11}^2 + F_{22}\sigma_{22}^2 + F_{33}\sigma_{33}^2 + 2F_{12}\sigma_{11}\sigma_{22} + 2F_{13}\sigma_{11}\sigma_{33} \\
& + 2F_{23}\sigma_{22}\sigma_{33} + F_{44}\sigma_{23}^2 + F_{55}\sigma_{13}^2 + F_{66}\sigma_{13}^2 \geq 1 \ .
\end{aligned}
\tag{2.49}
$$

The strength parameters can be found by using the maximum strengths of the lamina and considering it for each stress component

$$
\left.
\begin{aligned}
\sigma_{11} = X_t, \quad F_{11}X_t^2 + F_1 X_t = 1 \\
\sigma_{11} = X_c, \quad F_{11}X_c^2 + F_1 X_c = 1
\end{aligned}
\right\} \Rightarrow \quad
F_{11} = \left| \frac{1}{X_t X_c} \right| , \quad F_1 = \frac{1}{X_t} - \left| \frac{1}{X_c} \right| ,
$$

$$
\left.
\begin{aligned}
\sigma_{22} = Y_t, \quad F_{22}Y_t^2 + F_2 Y_t = 1 \\
\sigma_{22} = Y_c, \quad F_{22}Y_c^2 + F_2 Y_c = 1
\end{aligned}
\right\} \Rightarrow \quad
F_{22} = \left| \frac{1}{Y_t Y_c} \right| , \quad F_2 = \frac{1}{Y_t} - \left| \frac{1}{Y_c} \right| ,
$$

$$
\left.
\begin{aligned}
\sigma_{33} = Z_t, \quad F_{33}Z_t^2 + F_3 Z_t = 1 \\
\sigma_{33} = Z_c, \quad F_{33}Z_c^2 + F_3 Z_c = 1
\end{aligned}
\right\} \Rightarrow \quad
F_{33} = \left| \frac{1}{Z_t Z_c} \right| , \quad F_3 = \frac{1}{Z_t} - \left| \frac{1}{Z_c} \right| ,
$$

$$
\sigma_{12} = S_{12}, \quad F_{44}S_{12}^2 = 1 \Rightarrow \quad F_{44} = \frac{1}{S_{23}^2} ,
$$

$$
\sigma_{13} = S_{13}, \quad F_{55}S_{13}^2 = 1 \Rightarrow \quad F_{55} = \frac{1}{S_{13}^2} ,
$$

$$
\sigma_{23} = S_{23}, \quad F_{66}S_{23}^2 = 1 \Rightarrow \quad F_{66} = \frac{1}{S_{12}^2} \ .
\tag{2.50}
$$

The strength parameters F_i and F_{ii} are calculated with the experimental determined normal, compressive and shear strengths. The interaction strength parameter F_{12}, F_{13} and F_{23} are of the following form

$$
F_{ij} = F_{ij}^* \sqrt{F_{ii} F_{jj}} ,
\tag{2.51}
$$

that are also determinable through experimental tests using combined load cases. Due to the fact, that these tests are rather costly, the F_{ij}^* are therefore empirically determined. In [73], the use of $F_{ij}^* = -0.5$ is recommended for composites made of glass or carbon fiber reinforced epoxy resin.

3 Determination of Material Parameters of Fiber Reinforced Plastics

3.1 Introduction

This chapter deals in general with the material parameter identification used for the on-going finite element simulations. Therefore, the elastic parameters used for the elasticity tensor as well as the strength parameters for the failure criteria have to be evaluated.

The measurement effort for FRP materials is therefore sufficiently higher compared to materials with isotropic behavior due to the material behavior that differs significantly transverse to the fiber direction.

For a better understanding of this effort it must be mentioned that for one specific fiber/matrix combination at least a full set of 25 destructive measurements using a universal tensile testing have to be performed ([74]). Therefore, the assumption of transversely isotropic material behavior with a minimal statistical power of five for each parameter was made. Furthermore, at the early design stage with FRP materials one has to consider firstly, a large pool of possible fiber/matrix combinations and secondly, due to manufacturing, each fiber/matrix combination itself can differ because of a possible changing of the fiber volume fraction and also by different curing cycles.

To delimit this problematic and to stay within a given budget, a direct nondestructive method ([75]) was developed to fast characterize different FRP materials suitable for thick filament wound rotating structures, e.g. flywheel rotors.

In the following, the described methods are used to identify the in-plane stiffness parameters of transversely isotropic plates that are manufactured in the same way as thick filament wound structures. The results are used for characterization purpose only because pre-simulations with assumed parameters, mostly out of [76], showed that a low stiffness transverse to the fiber direction and density lead to a reduced stress distribution in radial direction of rotating thick wound structures. This aspect is the key for success and further used for material selection for thick wound structures using modal analysis performed on thin rectangular unidirectional FRP plates.

After selection and defining repeatable process parameters for manufacturing, the full sets of destructive measurements were performed in cooperation with the Institute of Materials Science and Technology at Vienna University of Technology to measure the material parameters.

3.2 Nondestructive Methods Based on Modal Analysis

Both nondestructive methods, explained in the following, need the results from a previous experimental modal analysis, performed on thin rectangular plates, as input quantities. The results are the mode shapes (the number of nodal lines separated in each direction) and the undamped natural frequencies for each mode shape. Based on those, the elastic material parameters are evaluated by a direct and an iterative numerical method.

3.2.1 Direct Identification Using Lagrange's Equation of Motion

The basis of this method is similar to the single degree of freedom (displacement x) spring-mass system. There, the knowledge of the mass m and the measured natural frequency ω directly calculates the elastic spring constant $k = \omega^2 m$. This can be seen by using Lagrange's equation of motion

$$\frac{d}{dt}\left(\frac{\partial T}{\partial \dot{q}_i}\right) - \frac{\partial T}{\partial q_i} + \frac{\partial V}{\partial q_i} = 0, \quad i = 1, 2, ..., n \tag{3.1}$$

where $q = x$ is the generalized coordinate. The total potential energy $V = \frac{1}{2}kq^2$ in combination with the kinetic energy $T = \frac{1}{2}m\dot{q}^2$ and by use of Lagrange's equation of motion directly shows up an expression for the natural frequency of this system $\ddot{q} + \frac{k}{m}q = 0$, whose solution for the natural frequency is already discussed above.

Direct Method By assuming, that the above procedure also holds for any structure and furthermore for every mode shape, it is possible to calculate the natural frequency of any mode shape. Vice versa, by knowing a sufficient number N of natural frequencies it must be possible to calculate N_P unknown elastic parameters of the structure by setting up an overdetermined system of equations $N > N_P$. This system can be solved e.g. by a least squares fit.

As noted earlier, the method is applied to rectangular plates. Therefore, the classical plate theory is used to calculate the total potential energy V and the kinetic energy T of an ordinary plate summarized in [72]. Due to the Kirchhoff assumptions the equations are given as follows

$$V = \frac{1}{2}\int_\Omega \left[N_{xx}\varepsilon_{xx} + M_{xx}\kappa_{xx} + N_{yy}\varepsilon_{xx} + M_{yy}\kappa_{yy} + N_{xy}\gamma_{xy} + M_{xy}\kappa_{xy}\right] dxdy \tag{3.2}$$

$$T = \frac{1}{2}\int_\Omega \left[\underbrace{\rho h}_{I_0}\,\dot{w}^2 + \underbrace{\rho\frac{h^3}{12}}_{I_2}\left(\left(\frac{\partial \dot{w}}{\partial x}\right)^2 + \left(\frac{\partial \dot{w}}{\partial y}\right)^2\right)\right] dxdy\ , \tag{3.3}$$

where the quantities (N_{xx}, N_{yy}, N_{xy}) are called the in-plane force resultants and (M_{xx}, M_{yy}, M_{xy}) are called the moment resultants. Furthermore, (ε_{xx}, ε_{yy}, γ_{xy}) are the membrane strains and (κ_{xx}, κ_{yy}, κ_{xy}) are the curvatures depending on the deflection w of the plate with thickness h and density ρ.

Due to the further performed measurement, with the possibility to measure the deflection w of the plate (the out of plane movement), the membrane strains are neglected and therefore the curvature $\boldsymbol{\kappa}$ and moment resultants $\boldsymbol{M}$ are used

$$\boldsymbol{\kappa} = \begin{bmatrix} \kappa_{xx} \\ \kappa_{yy} \\ \kappa_{xy} \end{bmatrix} = \begin{bmatrix} -\frac{\partial^2 w}{\partial x^2} \\ -\frac{\partial^2 w}{\partial y^2} \\ -2\frac{\partial^2 w}{\partial x \partial y} \end{bmatrix} \tag{3.4}$$

$$\boldsymbol{M} = \begin{bmatrix} M_{xx} \\ M_{yy} \\ M_{xy} \end{bmatrix} = - \begin{bmatrix} D_{11}\frac{\partial^2 w}{\partial x^2} + D_{12}\frac{\partial^2 w}{\partial y^2} + 2D_{16}\frac{\partial^2 w}{\partial x \partial y} \\ D_{12}\frac{\partial^2 w}{\partial x^2} + D_{22}\frac{\partial^2 w}{\partial y^2} + 2D_{26}\frac{\partial^2 w}{\partial x \partial y} \\ D_{16}\frac{\partial^2 w}{\partial x^2} + D_{26}\frac{\partial^2 w}{\partial y^2} + 2D_{66}\frac{\partial^2 w}{\partial x \partial y} \end{bmatrix} , \tag{3.5}$$

where $(D_{11}, D_{22}, D_{12}, D_{16}, D_{26}, D_{66})$ are the components of the bending stiffness tensor $\boldsymbol{D}$. In combination with the generalized coordinate $q = w(t, x, y)$ that can be separated to $q = Q(t)W(x, y)$, and the assumption of transversely isotropic material behavior $(D_{16} = D_{26} = 0)$ the total potential energy V and the kinetic energy T computes as

$$V = \frac{1}{2}\int_{\Omega}\left[D_{11}\left(\frac{\partial^2 w}{\partial x^2}\right)^2 + 2D_{12}\frac{\partial^2 w}{\partial x^2}\frac{\partial^2 w}{\partial y^2} + D_{22}\left(\frac{\partial^2 w}{\partial y^2}\right)^2 + 4D_{66}\left(\frac{\partial^2 w}{\partial x \partial y}\right)^2\right]dxdy$$

$$= \frac{Q^2(t)}{2}\left[D_{11}\underbrace{\int_{\Omega}\left(\frac{\partial^2 W}{\partial x^2}\right)^2 dxdy}_{\alpha} + 2D_{12}\underbrace{\int_{\Omega}\frac{\partial^2 W}{\partial x^2}\frac{\partial^2 W}{\partial y^2}dxdy}_{\beta}\right.$$

$$\left. + D_{22}\underbrace{\int_{\Omega}\left(\frac{\partial^2 W}{\partial y^2}\right)^2 dxdy}_{\gamma} + 4D_{66}\underbrace{\int_{\Omega}\left(\frac{\partial^2 W}{\partial x \partial y}\right)^2 dxdy}_{\delta}\right] , \tag{3.6}$$

$$T = \frac{1}{2}\int_{\Omega}\left[I_0\dot{q}^2 + I_2\left(\left(\frac{\partial \dot{q}}{\partial x}\right)^2 + \left(\frac{\partial \dot{q}}{\partial y}\right)^2\right)\right]dxdy$$

$$= \frac{1}{2}\dot{Q}^2(t)\underbrace{\int_{\Omega}\left[I_0 W^2(x,y) + I_2\left(\left(\frac{\partial W(x,y)}{\partial x}\right)^2 + \left(\frac{\partial W(x,y)}{\partial y}\right)^2\right)\right]dxdy}_{\epsilon} . \tag{3.7}$$

By using the above given terms in Lagrange's equation of motion (3.1), a second order differential equation results

$$\ddot{Q}(t) + \underbrace{\frac{D_{11}\alpha + 2D_{12}\beta + D_{22}\gamma + 4D_{66}\delta}{\epsilon}}_{\omega^2} Q(t) = 0 . \tag{3.8}$$

Assuming that this relation holds for any mode shape with the natural frequency ω_i and deflection $W_i(x,y) = W_i(x)W_i(y)$ the already mentioned overdetermined system of equations can be set up

$$
\underbrace{\begin{bmatrix}
\alpha_1 & 2\beta_1 & \gamma_1 & 4\delta_1 \\
\alpha_2 & 2\beta_2 & \gamma_2 & 4\delta_2 \\
\alpha_3 & 2\beta_3 & \gamma_3 & 4\delta_3 \\
. & . & . & . \\
\alpha_i & 2\beta_i & \gamma_i & 4\delta_i \\
. & . & . & . \\
\alpha_N & 2\beta_N & \gamma_N & 4\delta_N
\end{bmatrix}}_{A}
\underbrace{\begin{bmatrix}
D_{11} \\
D_{12} \\
D_{22} \\
D_{66}
\end{bmatrix}}_{D^*}
=
\underbrace{\begin{bmatrix}
\omega_1^2 \epsilon_1 \\
\omega_2^2 \epsilon_2 \\
\omega_3^2 \epsilon_3 \\
. \\
\omega_i^2 \epsilon_i \\
. \\
\omega_N^2 \epsilon_N
\end{bmatrix}}_{B} ,
\tag{3.9}
$$

to solve for the components of the bending stiffness tensor $\boldsymbol{D}$ by using a least squares approximation

$$
D^* = \begin{bmatrix}
D_{11} \\
D_{12} \\
D_{22} \\
D_{66}
\end{bmatrix} = (A^T A)^{-1} A^T B \quad , \quad
\boldsymbol{D} = \begin{bmatrix}
D_{11} & D_{12} & 0 \\
D_{12} & D_{22} & 0 \\
0 & 0 & D_{66}
\end{bmatrix} .
\tag{3.10}
$$

Approximation of Mode Shape Deflection   The mode shape deflection $W(x,y)$ is approximated by the solution of the equation of motion of anisotropic plates given in [72]. The fourth order differential equation used for a plate with dimensions $0 \le x \le a$, $0 \le y \le b$ and thickness h reads as

$$
D_{11}\frac{\partial^4 W}{\partial x^4} + 2(D_{12} + 2D_{66})\frac{\partial^4 W}{\partial x^2 \partial y^2} + D_{22}\frac{\partial^4 W}{\partial y^4} = q_f - I_0 \ddot{W} + I_2\left(\frac{\partial^2 \ddot{W}}{\partial x^2} + \frac{\partial^2 \ddot{W}}{\partial y^2}\right) ,
\tag{3.11}
$$

where the homogeneous solutions are directly related to the mode shapes using the number of nodal lines m, n in each direction. Therefore, a separation approach

$$
W_{mn}(x,y) = W_m(x)W_n(y) \quad m = 1,2,3,... \quad n = 1,2,3... ,
\tag{3.12}
$$

is used and the general homogenous solution follows to

$$
\begin{aligned}
W_m(x) &= A_{1m}\cos(\alpha_m x) + A_{2m}\sin(\alpha_m x) + A_{3m}\cosh(\alpha_m x) + A_{4m}\sinh(\alpha_m x) \\
W_n(y) &= B_{1n}\cos(\beta_n y) + B_{2n}\sin(\beta_n y) + B_{3n}\cosh(\beta_n y) + B_{4n}\sinh(\beta_n y) .
\end{aligned}
\tag{3.13}
$$

In addition, the deflections for the rigid body motions for the free supported plate compute by

$$
W_0(x) = 1 \quad , \quad W_0(y) = 1 \quad , \quad W_1(x) = 1 - \frac{2x}{a} \quad , \quad W_1(y) = 1 - \frac{2y}{b} ,
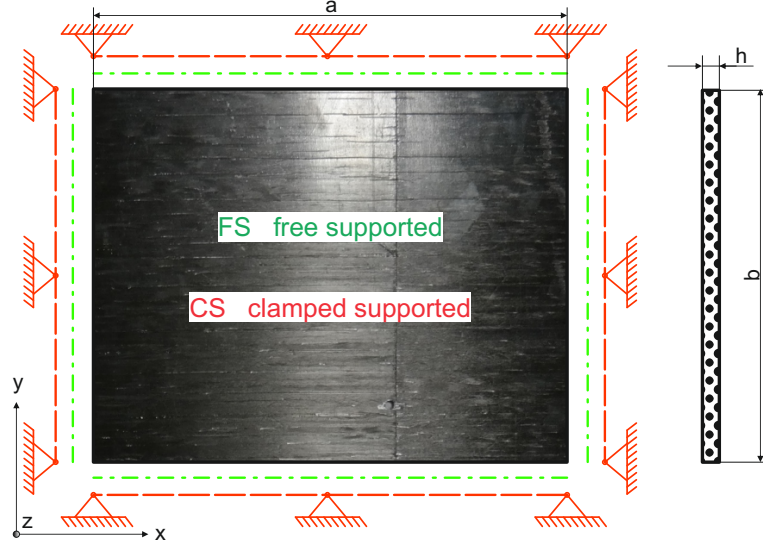\tag{3.14}
$$

Figure 3.1: Rectangular plate and applied boundary conditions.

where the coefficients A_{im}, B_{in}, α_m, β_n depend on the applied boundary conditions (see Fig. 3.1). The coefficients for the free (FS) and clamped (CS) supported solutions are summarized in Table 3.1. The measured natural frequencies and the corresponding approximated mode shapes are used to set up (3.9), to further solve for the elastic material parameters in a direct way.

Table 3.1: Boundary conditions and coefficients for the free (FS) and clamped (CS) supported solutions.

Boundary conditions	$x = 0$	$x = a$	$y = 0$	$y = b$
FS	$\frac{\partial^2 W_m}{\partial x^2} = 0$ $\frac{\partial^3 W_m}{\partial x^3} = 0$	$\frac{\partial^2 W_m}{\partial x^2} = 0$ $\frac{\partial^3 W_m}{\partial x^3} = 0$	$\frac{\partial^2 W_n}{\partial y^2} = 0$ $\frac{\partial^3 W_n}{\partial y^3} = 0$	$\frac{\partial^2 W_n}{\partial y^2} = 0$ $\frac{\partial^3 W_n}{\partial y^3} = 0$
CS	$W_m = 0$ $\frac{\partial W_m}{\partial x} = 0$	$W_m = 0$ $\frac{\partial W_m}{\partial x} = 0$	$W_n = 0$ $\frac{\partial W_n}{\partial y} = 0$	$W_n = 0$ $\frac{\partial W_n}{\partial y} = 0$
Coefficients	$A_{1m} = B_{1n}$	$A_{2m} = B_{2n}$	$A_{3m} = B_{3n}$	$A_{4m} = B_{4n}$
FS	$-\lambda_i$	1	$-\lambda_i$	1
CS	$-\lambda_i$	1	λ_i	-1
FS/CS	$\alpha_1 = \frac{4.730}{a}$ $\beta_1 = \frac{4.730}{b}$ $\lambda_1 = 1.0178$	$\alpha_2 = \frac{7.853}{a}$ $\beta_2 = \frac{7.853}{b}$ $\lambda_2 = 0.99922$	$\alpha_m \approx (2m+1)\frac{\pi}{2a}$ $\beta_n \approx (2n+1)\frac{\pi}{2b}$ $\lambda_i = -1 \quad i > 2$	

3.2.2 Iterative Numerical Identification Using Genetic Algorithm

The method uses, similar to the above presented approach, the measured natural frequencies and further an optimization procedure performed on a FE model to estimate iteratively the elastic material parameters. The advantage of this method is the possibility to identify any wanted number of parameters.

Iterative Numerical Method The optimization uses a function that minimizes the discrepancies between the experimental measured and evaluated numerical modal data. Therefore, the relative difference of the natural frequencies is used, computed as follows

$$\eta_i^{\omega_N} = \left(\widetilde{\omega}_i - \omega_i\right)/\omega_i \quad i = 1, 2, ..., n_{\text{modes}} \ , \tag{3.15}$$

where the ω_i and $\widetilde{\omega}_i$ are the ith measured and simulated natural frequencies that are summarized in a global error vector $\boldsymbol{\eta}$

$$\boldsymbol{\eta}^{\omega_N} = \left(\eta_1^{\omega_N}, \eta_2^{\omega_N}, ..., \eta_{n_{\text{modes}}}^{\omega_N}\right)^T \ . \tag{3.16}$$

In order to guarantee a defined order of the simulated mode shapes according to the measured mode shapes, well defined lower and upper bounds for the material parameters are necessary. This results in a constrained optimization for the objective function f, which reads as

$$\min_{\boldsymbol{x}} \left\{f(\boldsymbol{x})\right\} = \min_{\boldsymbol{x}} \left\{\|\boldsymbol{\eta}^{\omega_N}(\boldsymbol{x})\|_2^2\right\} \ , \tag{3.17}$$

where $\boldsymbol{x} = (E_1, E_2, E_3, \nu_{12}, \nu_{13}, \nu_{23}, G_{12}, G_{13}, G_{23})^T$ is the vector of the optimization variables, the full set of material parameters for a general orthotropic material and $\|.\|_2$ symbolizes the Euclidean vector norm. The optimization was performed with the MATLAB built-in function *ga(...)* [77]. Therefore, the population size was set to 50 and five elite individuals were used. Any other options where left default.

Finite Element Model of the Plate The simulated natural frequencies are evaluated by a 3-dimensional orthotropic plate model built up in the FE software COMSOL ([68]) performing a modal analysis using the following semi-discrete Galerkin eigenvalue formulation for an undamped structure

$$\left[\boldsymbol{K}_u - \widetilde{\omega}_i^2 \boldsymbol{M}_u\right] \boldsymbol{\Phi}_i = \boldsymbol{0} \ , \tag{3.18}$$

where $\boldsymbol{M}$ and $\boldsymbol{K}$ denotes the mass and stiffness matrix of the plate. The mode shape relates to the mass scaled eigenvector $\boldsymbol{\Phi}_i$ for the corresponding natural frequency $\widetilde{\omega}_i$. The boundaries on each edge are FS or CS, depending on the study, see Fig. 3.1. The geometry of the model is discretized by hexahedron finite elements with tri-cubic basis functions, see Fig. 3.2(a). The elasticity tensor $\boldsymbol{E}$ for each element is given by the optimization variables described above and results by using the relation $\boldsymbol{E} = \boldsymbol{C}^{-1}$ with the compliance tensor $\boldsymbol{C}$ to
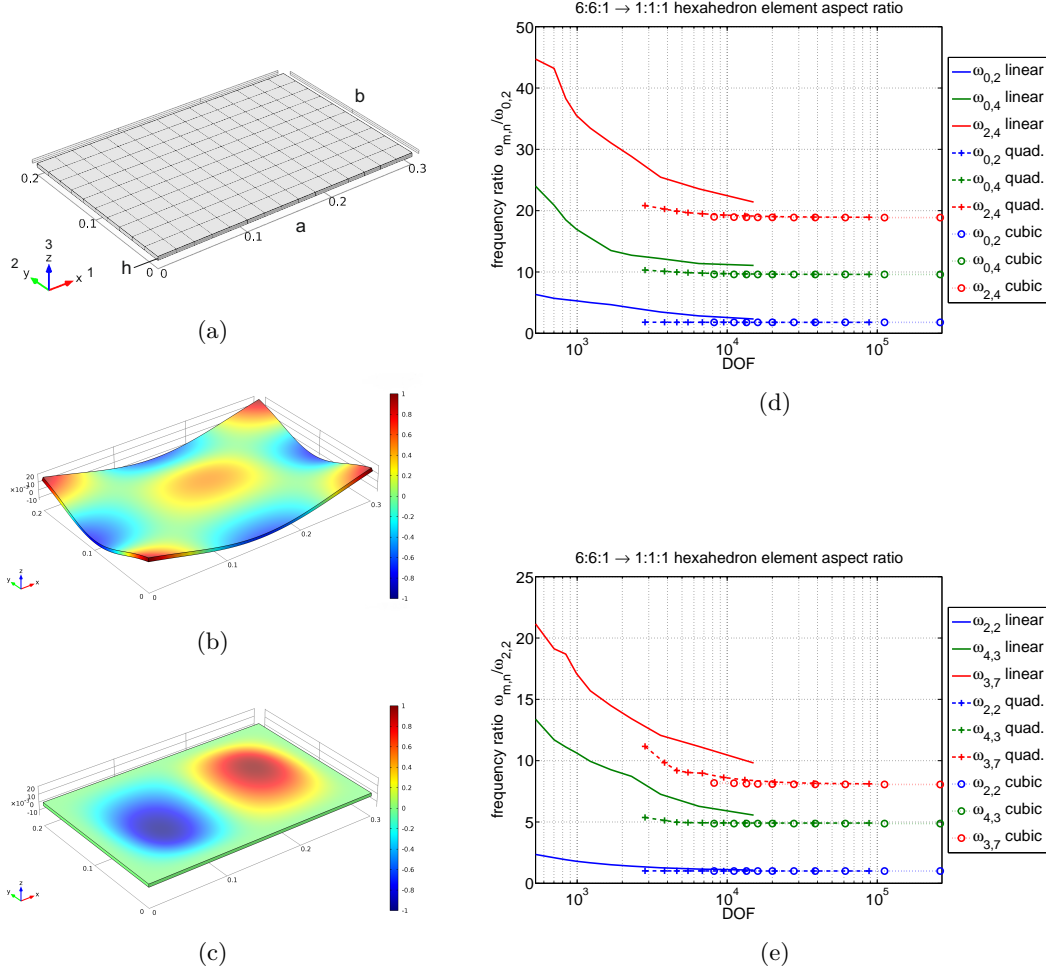
(a)

(b)

(c)

(d)

(e)

Figure 3.2: Numerical modal analysis of a rectangular plate: (a) plate model showing the mesh, dimensions in mm; (b) sample mode shape for FS; (c) sample mode shape for CS; (d) mesh study for FS; (e) mesh study for CS.

$$
\boldsymbol{C} =
\begin{bmatrix}
\frac{1}{E_1} & \frac{-\nu_{12}}{E_1} & \frac{-\nu_{13}}{E_1} & 0 & 0 & 0 \\
& \frac{1}{E_2} & \frac{-\nu_{23}}{E_2} & 0 & 0 & 0 \\
& & \frac{1}{E_3} & 0 & 0 & 0 \\
& & & \frac{1}{G_{23}} & 0 & 0 \\
& sym. & & & \frac{1}{G_{13}} & 0 \\
& & & & & \frac{1}{G_{12}}
\end{bmatrix} .
\tag{3.19}
$$

The optimization, especially with a genetic algorithm, performs a lot of function evaluations. Therefore, a drastically reduction of degrees of freedom (DOF) to reduce simulation effort and time is necessary. When performing a modal analysis one has to keep in mind that depending on the DOF the mode shape differs and furthermore the value

of the natural frequency changes. This effect is shown in Fig. 3.2(d) and Fig. 3.2(e) for different boundary conditions and orders of basis functions. The hexahedron element aspect ratio depends on the DOF and defines a coarse (6:6:1) or a fine (1:1:1) FE mesh, where one is equal to the plate thickness.

In the following described simulations, a hexahedron element aspect ratio of 4:4:1 that is equal to $18 \times 18 \times 4.5 \, \text{mm}^3$ and cubic basis functions were used.

3.2.3 Numerical Test Case: Unidirectional CFRP Plate

Both methods were tested by use of the FE model described above. Therefore, an example plate with $300 \times 300 \times 4.5 \, \text{mm}^3$ with a mass density of $1470 \, \text{kg/m}^3$ was used. The elastic parameters are chosen to $E_1 = 130 \, \text{GPa}$, $E_2 = E_3 = 9 \, \text{GPa}$, $\nu_{12} = \nu_{13} = 0.35$, $\nu_{23} = 0.3$, $G_{12} = G_{13} = 4.5 \, \text{GPa}$ and $G_{23} = 3.5 \, \text{GPa}$. The numerical modal analysis results for the first 12 mode shapes and different boundary conditions (FS and CS) are given in Table 3.2.

The presented methods were then applied to identify the elastic parameters for the given numerical test case. At first, the direct method is carried out and the results can be seen in Table 3.3 and Table 3.4. The FS condition shows a maximum relative error for the poisson ratio ν_{12} that is about 69 %. This large discrepancy is caused by the second derivatives of the deflection shape and further the well underestimated bending stiffness parameter D_{12} that results for mode shapes with $m < 2$ or $n < 2$. The CS condition stays within a maximum relative error of about 16 %. There, due to the fixed boundary condition of the FE model, the mode shapes slightly differ to the analytic results that leads to the overestimated results.

Table 3.2: Modal analysis results for the FS and CS boundary conditions.

Mode	FS		CS	
	m,n	f in Hz	m,n	f in Hz
1	(1,1)	92.0	(2,2)	507.0
2	(0,2)	127.1	(2,3)	631.0
3	(1,2)	226.5	(2,4)	893.5
4	(0,3)	349.7	(2,5)	1294.3
5	(1,3)	447.7	(3,2)	1315.7
6	(2,0)	482.5	(3,3)	1400.2
7	(2,1)	516.7	(3,4)	1581.0
8	(2,2)	623.1	(2,6)	1819.4
9	(0,4)	687.3	(3,5)	1887.5
10	(1,4)	776.0	(3,6)	2329.8
11	(2,3)	822.2	(2,7)	2458.4
12	(2,4)	1124.1	(4,2)	2496.5

Therefore, the direct identification method is modified by use of global weighting parameters g_i resulting in the modified frequency expression

$$g_1 D_{11} \alpha_i + g_2 2 D_{12} \beta_i + g_3 D_{22} \gamma_i + g_4 4 D_{66} \delta_i = \epsilon_i \omega_i^2 \ . \tag{3.20}$$

The weighting parameters are calculated by an unconstrained optimization using the objective function

$$\min_{\boldsymbol{x}} \{f(\boldsymbol{x})\} = \min_{\boldsymbol{x}} \left\{ \left\| \boldsymbol{\eta}^{\mathrm{FE}}(\boldsymbol{x}) \right\|_2^2 \right\} \ , \tag{3.21}$$

where $\boldsymbol{x} = (g_1, g_2, g_3, g_4)^T$ is the vector of the optimization variables and $\boldsymbol{\eta}^{FE}$ is the vector of relative errors between the elastic parameters of the FE model and the direct identified results. The results for the global weights and the modified direct identification method are summarized in Table 3.3 and Table 3.4.

In contrast, the iterative method is able to determine the elastic parameters with a numerical error, depending on the defined change in the error function. The obtained parameters are the result of 1025 function evaluations that makes this method very time consuming.

Table 3.3: Identification results for the numerical test case and FS boundary condition by use of the modal analysis results of Table 3.2.

Elastic parameter	FE modal analysis	Direct method	Direct modified*	Iterative method
E_1, GPa	130	125.87	130.04	130.12
E_2, GPa	9	8.82	8.99	8.99
ν_{12}	0.35	0.5924	0.3499	0.3453
G_{12}, GPa	4.5	3.88	4.50	4.49

* $g_1 = 0.984$, and $g_2 = 1.688$, $g_3 = 0.997$ and $g_4 = 0.863$.

Table 3.4: Identification results for the numerical test case and CS boundary condition by use of the modal analysis results of Table 3.2.

Elastic parameter	FE modal analysis	Direct method	Direct modified*	Iterative method
E_1, GPa	130	136.12	130.35	128.29
E_2, GPa	9	9.56	9.12	8.85
ν_{12}	0.35	0.4053	0.3699	0.3664
G_{12}, GPa	4.5	4.67	4.55	4.93

* $g_1 = 1.028$, and $g_2 = 1.321$, $g_3 = 1.010$ and $g_4 = 1.032$.
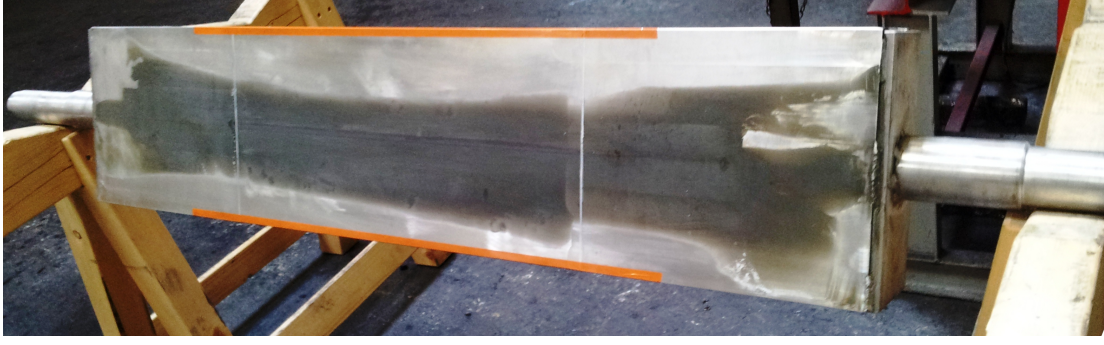
Figure 3.3: Winding mandrel for plate specimen manufacturing.

3.2.4 Manufacturing of Test Specimens

The specimens investigated in the following material parameter identification are manufactured by wet filament winding. Therefore, the impregnated and pre-tensioned fiber roving is wound on an aluminium mandrel with rectangular cross-section to guarantee flat specimens, see Fig. 3.3.

After winding operation, the largest front and back surfaces are further flattened by using metal cover plates that are counter fixed with clamps. The finished cured part was then pulled off the mandrel by a hydraulic cylinder and the specimen geometry was machined using a saw and milling operation. This procedure was repeated for different fiber/matrix combinations summarized in Table 3.5.

Table 3.5: Fiber/matrix combinations for test specimens. Unidirectional arranged fibers with a volume fraction of 60 %.

| Plate ID	Fiber type			Matrix type, weight ratio in %		
	E_l	X_t	ρ	E	X_t	T_h
1	Torayca T800S 24K			705, epoxy A/B/hardener 25:25:50		
	294 GPa	5880 MPa	1800 kg/m^3	3 GPa	72 MPa	160°C
2	Dialead K13916 16K			705, epoxy A/B/hardener 25:25:50		
	725 GPa	3000 MPa	2110 kg/m^3	3 GPa	72 MPa	160°C
3	Torayca T800S 24K			704, epoxy/hardener 76.9:23.1		
	294 GPa	5880 MPa	1800 kg/m^3	3 GPa	59 MPa	70°C
4	Torayca T800S 24K			700, epoxy A/B/hardener 49.6:5:45.4		
	294 GPa	5880 MPa	1800 kg/m^3	2.9 GPa	67 MPa	160°C
5	Dialead K63712 12K			700, epoxy A/B/hardener 49.6:5:45.4		
	633 GPa	2628 MPa	2120 kg/m^3	2.9 GPa	67 MPa	160°C
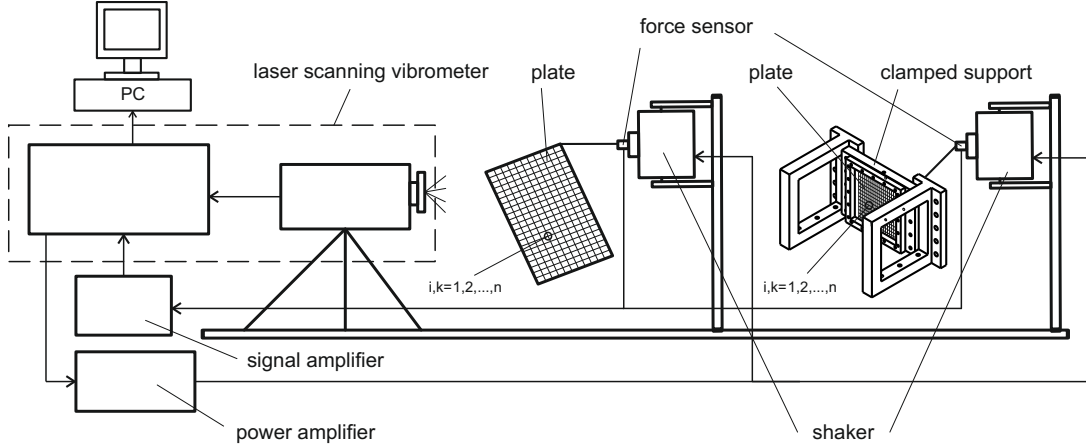
Figure 3.4: FVT scheme for the the FS and CS plates.

3.2.5 Measurement Setup - Modal Analysis of Rectangular Plates

The modal characteristics for the square plates with FS and CS boundary condition are identified by forced vibration testing (FVT). Therefore, both setups were excited in a fixed point i and the acceleration $a_k(t)$ is measured together with the forcing signal $F_i(t)$, see Fig. 3.4. After measurement, the time signals are Fourier transformed into frequency domain and the peaks of the frequency response function $H(j\omega) = a(j\omega)/F(j\omega)$ belong to the vibrational modes of the plate. The structural response was measured in discrete points by a PSV-500-H4 LSV in a non contact way, see Fig. 3.5(a).

Free Support   The edge of the plate is directly mounted on the piezoelectric force sensor which is fixed onto the electrodynamic shaker, see Fig. 3.5(b). This fulfills almost the FS boundary condition as a compromise to the setup effort and possible number of identifiable mode shapes, discussed in [75].

Clamped Support   The plate is mounted inside a rigid support, where the plate is fully clamped between a steel frame and a thick steel plate, see Fig. 3.5(c). The force input was provided by a coupling rod, including a piezoelectric force sensor that was mounted on an electrodynamic shaker, see Fig. 3.5(d).

Measurement Setup   The out of plane movement of the plates was observed in $n = 900$ points. The excitation signal used was a periodic chirp $(20\,\mathrm{Hz}-2.5\,\mathrm{kHz})$ for both setups. The measurements were filtered and averaged $(n_{AVG} = 10)$. Afterwards, the best measurable natural bending frequencies and the corresponding mode shapes were extracted out of the average frequency response function (FRF) over all measured points, see Fig. 3.6. The measured natural frequencies and corresponding mode shapes (nodal lines m, n) were then used for the identification of the elastic parameters.
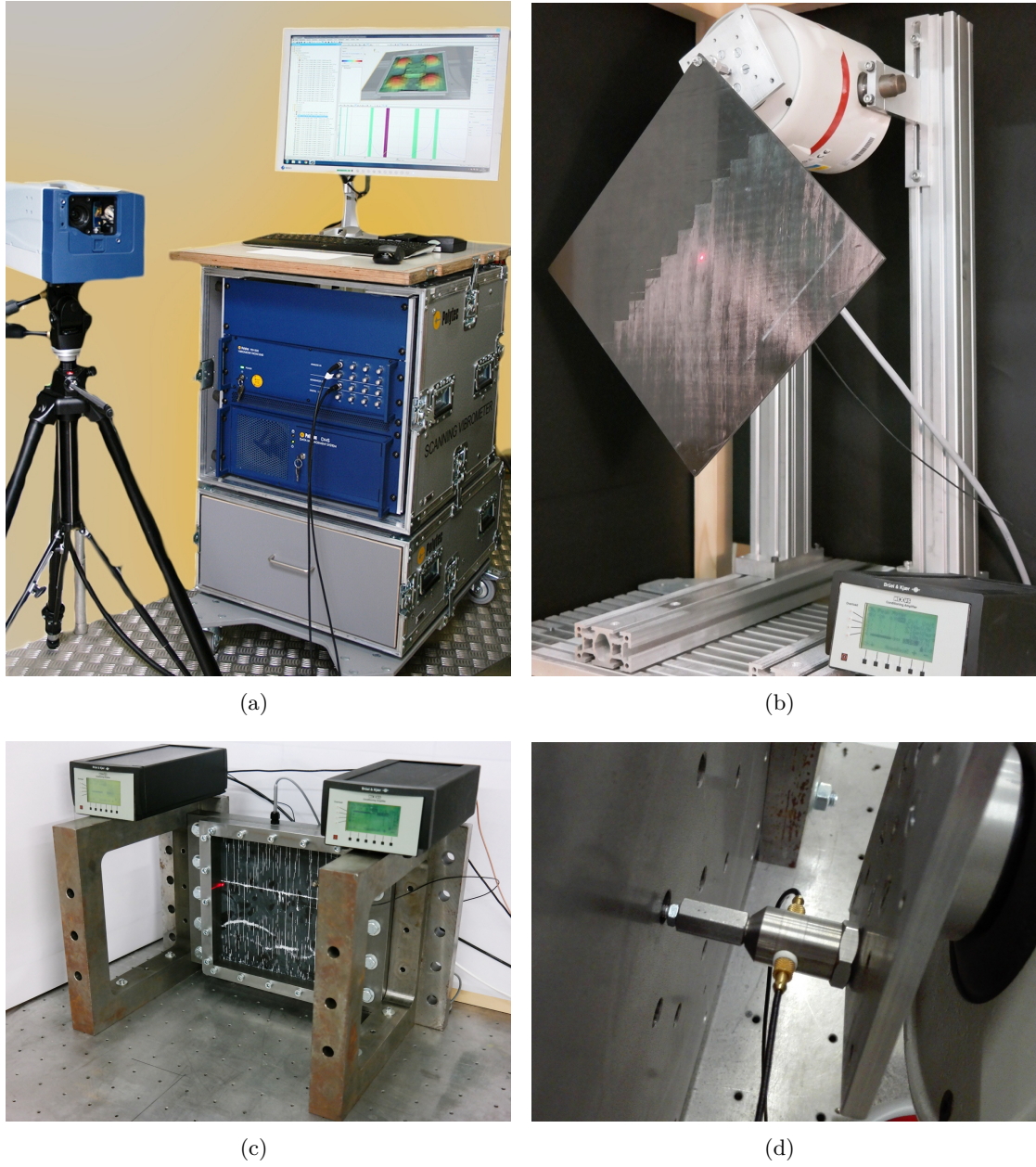
(a)

(b)

(c)

(d)

Figure 3.5: Experimental modal analysis of rectangular plates: (a) PSV-500-H4 laser scanning vibrometer; (b) FS plate and piezoelectric force sensor mounted on shaker; (c) stiff modal test rig for CS plate; (d) piezoelectric force sensor mounted on shaker used for CS plate excitation.
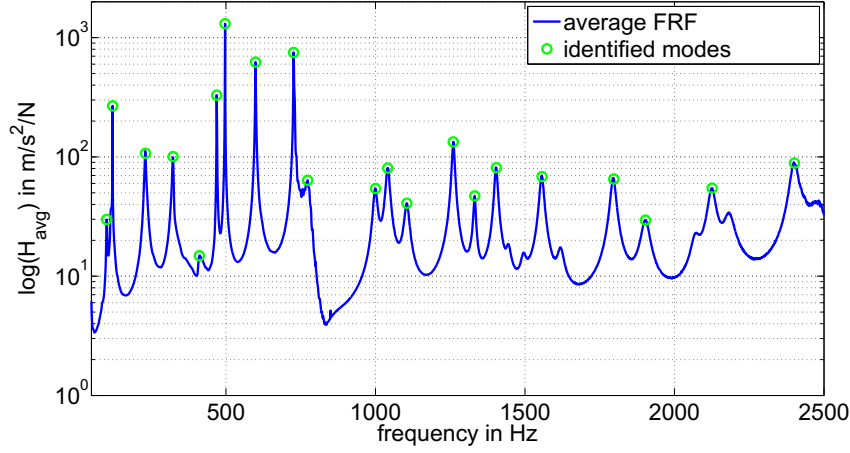
Figure 3.6: Average FRF and identified peaks of the present mode shapes of plate 1.

3.2.6 Analysis of Results

Free Support (FS)   The first measurement was performed on unidirectional carbon fiber reinforced plastics (UDCFRP) square plates with different fiber/matrix combinations and ply layups. The results of the modified direct (MDI) and iterative identification (II) method are summarized in Table 3.6.

These identified elastic parameters are the results of the lowest ten and best measurable mode shapes. The peak-picking for the natural frequencies and nodal lines counting for the corresponding mode shape was done fully manually, because interpreting the modal data needs experimental modal analysis experience and can not be easy simplified

Table 3.6: Modified direct (MDI) and iterative (II) identification results for example FS UDCFRP plates.

Plate ID		E_1, GPa	E_2, GPa	ν_{12}	G_{12}, GPa
1 T800S/705 $300 \times 300 \times 4.16\,\mathrm{mm}^3$	MDI	125.2	7.3	0.458	4.1
9-ply $[0°]_9$, $m = 0.588\,\mathrm{kg}$	II	122.8	6.4	0.275	5.4
2 K13916/705 $300 \times 300 \times 3.75\,\mathrm{mm}^3$	MDI	310.3	4.8	0.426	2.4
6-ply $[0°]_6$, $m = 0.541\,\mathrm{kg}$	II	338.9	4.8	0.429	2.0
3 T800S/704 $300 \times 300 \times 6.46\,\mathrm{mm}^3$	MDI	153.3	10.5	0.404	4.9
16-ply $[0°]_{16}$, $m = 0.905\,\mathrm{kg}$	II	123.6	8.2	0.283	6.9
4 T800S/700 $300 \times 300 \times 6.38\,\mathrm{mm}^3$	MDI	149.1	9.0	0.499	4.6
15-ply $[0°]_{15}$, $m = 0.904\,\mathrm{kg}$	II	122.6	7.8	0.495	7.0
5 K63712/700 $300 \times 300 \times 5.63\,\mathrm{mm}^3$	MDI	244.3	4.8	0.499	3.8
12-ply $[0°]_{12}$, $m = 0.834\,\mathrm{kg}$	II	250.8	5.4	0.337	3.6

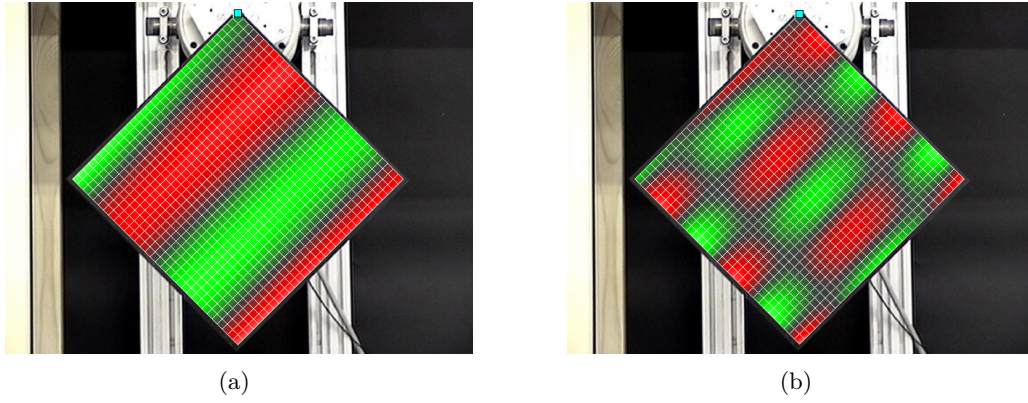(a)   (b)

Figure 3.7: Experimental modal analysis of plate 1 for FS boundary condition (nodal lines in black, excitation point in cyan): (a) mode shape $(0, 3)$ at $f = 197\,\mathrm{Hz}$; (b) mode shape $(2, 5)$ at $f = 1309\,\mathrm{Hz}$.

by trivial computations, e.g. modal assurance criterion. Some of the mode shapes are not apparent, unrecognizable deformed or hardly detectable due to very low vibration amplitudes. This can be improved by manufacturing thinner plates, but by use of wet filament winding a minimum of eight plies is the limit to manufacture UDCFRP plates. Sample mode shapes for plate 1 are depicted in Fig. 3.7(a) and Fig. 3.7(b).

The identified elastic parameter E_1 showed firstly the discrepancy between the high strength (T800S) and the high modulus (K13916 and K63712) fibers for both methods. Secondly, it differs for the T800S fiber within the MDI-method that is the result of the rather thick plate and therefore the parameter is underestimated due to less apparent bending modes in fiber direction. This has no effect onto the II-method were the results compare well among themselves.

The other elastic parameters are slightly influenced by the resin types (the mixtures are optimized for processing times and hardening temperatures) but strongly influenced by the resin fiber bond that is dependent on the PAN- or Pitch based fiber producing method. The PAN based T800S fiber shows higher values for E_2 and G_{12} in comparison to the Pitch based K13916 and K63712 fibers for both identification methods. The Poisson's ratio ν_{12} depends on both above mentioned reasons due to the well known relation $E_1\nu_{21} = E_2\nu_{12}$.

Clamped (CS) and Partial Clamped Support (PCS)   The already mentioned problematic of low vibration amplitudes gets even worse by increasing the stiffness of a system by applying more rigid boundary conditions. The MDI-method was not applicable because a minimum of four measured modes is necessary that could not be clearly identified. Furthermore, the measurement result is strongly dependent on the clamping force applied by the screws of the frame. It was observed, that increasing the applied torque leads to a convergence of the natural frequencies. Due to this large pre-stressing, the thinner plates 1 and 2 broke transverse to the fiber direction near the frame. Therefore,
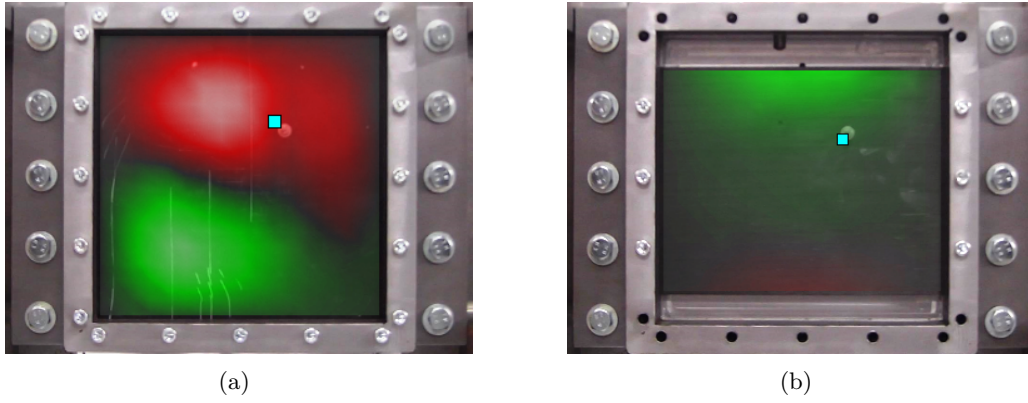
<div align="center">(a)   (b)</div>

Figure 3.8: Experimental modal analysis (nodal lines in black, excitation point in cyan):
(a) mode shape $(3, 2)$ at $f = 1949\,\text{Hz}$ of plate 3 for CS boundary condition;
(b) mode shape $(2, 1)$ at $f = 750\,\text{Hz}$ of plate 2 for PCS boundary condition.

the plates 1 and 2 were re-sized and partial clamped supported. Sample mode shapes are depicted in Fig. 3.8(a) and Fig. 3.8(b). The PCS condition increased the flexibility of the system, but now the excitation point is in any case too close to the nodal lines that leads to unexcited mode shapes. Hence, the MDI-method is also not applicable.

Table 3.7 shows the results of the II-method performed on the measurement result of three modes for each plate. It can be seen that the identified elastic parameter E_1 differs well compared to the FS condition. This overestimation results due to the fact that a fully clamped boundary condition is in reality not possible. Hence, due to this uncertainties the FS condition is used for the material characterization.

Table 3.7: Iterative identification (II) results for example CS and PCS UDCFRP plates.

Plate ID		E_1, GPa	E_2, GPa	ν_{12}	G_{12}, GPa
1 T800S/705 $259 \times 198 \times 4.16\,\text{mm}^3$	II	153.1	8.9	0.498	5.9
9-ply $[0°]_9$, $m = 0.335\,\text{kg}$	PCS				
2 K13916/705 $259 \times 198 \times 3.75\,\text{mm}^3$	II	355.2	5.0	0.452	5.2
6-ply $[0°]_6$, $m = 0.311\,\text{kg}$	PCS				
3 T800S/704 $259 \times 259 \times 6.46\,\text{mm}^3$	II	144.3	8.4	0.475	5.7
16-ply $[0°]_{16}$, $m = 0.682\,\text{kg}$	CS				
4 T800S/700 $259 \times 259 \times 6.38\,\text{mm}^3$	II	155.3	8.6	0.441	5.9
15-ply $[0°]_{15}$, $m = 0.678\,\text{kg}$	CS				
5 K63712/700 $259 \times 259 \times 5.63\,\text{mm}^3$	II	263.1	5.1	0.489	6.0
12-ply $[0°]_{12}$, $m = 0.623\,\text{kg}$	CS				

3.3 Destructive Material Testing

In the following, the destructive determination of material parameters for the selected UDCFRP material combinations is described. Therefore, many different standardized test methods exist that are mostly covered within ASTM, ISO, EN and DIN standards as well as standards of the aerospace industry (Airbus, Boeing, NASA).

Within this work the following test methods and adapted versions of them were used and performed on unidirectional and hoop wound specimen to measure the five elastic and six strength parameters:

- Tensile testing of flat coupon specimens DIN EN ISO 527-1&5 [78, 79], DIN EN ISO2561 [80] and DIN EN ISO 14129 [81], Young's modulus in fiber direction E_1, tensile strength in fiber direction X_t, Young's modulus transverse to fiber direction $E_2 = E_3$, tensile strength transverse to fiber direction $Y_t = Z_t$, Poisson's ratio $\nu_{12} = \nu_{13}$, shear modulus $G_{12} = G_{13}$ and shear strength $S_{12} = S_{13}$.

- Compression testing of flat coupon specimens DIN EN ISO 14126 [82], compression strength in fiber direction X_c and compression strength transverse to fiber direction $Y_c = Z_c$.

- 3-point bending tests on flat coupon specimens DIN EN ISO 14125 [83], bending Young's modulus in fiber direction E_{b1}, bending strength in fiber direction σ_{b1}, bending young's modulus transverse to fiber direction E_{b2}, bending strength transverse to fiber direction σ_{b2}.

- Split disc testing of hoop wound ring specimens, similar to ASTM D2290-12 [84], tensile strength in fiber direction X_t.

3.3.1 Investigated Materials

The flat coupon and ring specimens were manufactured by wet filament winding using the above mentioned aluminium mandrel with rectangular cross-section and an ordinary cylindrical mandrel made of steel. The investigated materials are the high strength CFRP T800S/705 and the high modulus CFRP K13916/705.

The flat coupon specimens were cut from the manufactured hoop and bidirectional wound plates. The layup and size of the specimens with a fiber volume fraction of 60% used for the above mentioned standardized test methods are summarized in the following:

- $[0°]_4$ $250 \times 12 \times 2.5\,\text{mm}^3$ (unidirectional), tension

- $[0°]_4$ $110 \times 10 \times 2.5\,\text{mm}^3$ (unidirectional), compression

- $[0°]_{14}$ $300 \times 25 \times 6.5\,\text{mm}^3$ (unidirectional), bending

- $[90°]_{10}$ $200 \times 25 \times 5.5\,\text{mm}^3$ (unidirectional), tension

- $[90°]_{10}$ $110 \times 10 \times 5.5\,\text{mm}^3$ (unidirectional), compression

- $[90°]_{14}$ $300 \times 25 \times 6.5\,\text{mm}^3$ (unidirectional), bending

- $\left[\pm 45°/+\overline{45°}\right]$ $250 \times 25 \times 2.5\,\text{mm}^3$ (bidirectional), tension

- $[0°]_5$ $\o 250 \times 10 \times 2.5\,\text{mm}^3$ (unidirectional), tension of ring specimen

To guarantee successful tests, some of the thicknesses and widths of the specimens were adapted due to the fact that by filament winding the quality of the specimens is much worse compared to a hand layup produced plate by use of an autoclave.

Furthermore, stripes of the same material with the configuration $\left[\pm 45°/+\overline{45°}\right]$ were added to some specimen at the load transfer points to avoid unwanted damage of the specimen in this area.

3.3.2 Testing of Flat Coupon Specimen

Tension Tests The above mentioned tension tests were performed using a Zwick Z250 Universal Testing System for the measurement of X_t and a Zwick Z50 Universal Testing System for the other parameters, see Fig. 3.9. The pulling force F was transmitted via wedge clamping jaws or ordinary clamping jaws depending on the maximum force. The applied force was measured by a load cell and the velocity of the crosshead travel was kept constant for all tests at $1\,\text{mm/min}$.

The strains were measured using the extensometer of the testing system and digital image correlation (DIC). Hence, by use of DIC, the non-contact measurement of the Poisson's ratios ν_{12}, ν_{21} and ν_{23} was done using a white spray painted stochastic pattern on the surface of the specimen.

Under the consideration of small strains that leads to the assumption of a constant cross-section surface during the whole test, the uni-axial stress σ of the specimen is given by the applied force F and the cross-section surface A_0

$$\sigma = \frac{F}{A_0} \ . \tag{3.22}$$

The engineering strain ε is expressed as the change in length ΔL per unit of the original length L

$$\varepsilon = \frac{\Delta L}{L} \ . \tag{3.23}$$

Poisson's ratios can be calculated by measuring the strains in different directions

$$\nu_{12} = -\frac{\varepsilon_q}{\varepsilon_l}, \quad \nu_{21} = -\frac{\varepsilon_l}{\varepsilon_q}, \quad \nu_{23} = -\frac{\varepsilon_t}{\varepsilon_q} \ . \tag{3.24}$$

The Young's modulus E is calculated as secant modulus using the stress differences of σ_1 and σ_2 and corresponding strain differences $\varepsilon_1 = 0.0005$ and $\varepsilon_2 = 0.0025$

$$E = \frac{\sigma_2 - \sigma_1}{\varepsilon_2 - \varepsilon_1} \ . \tag{3.25}$$

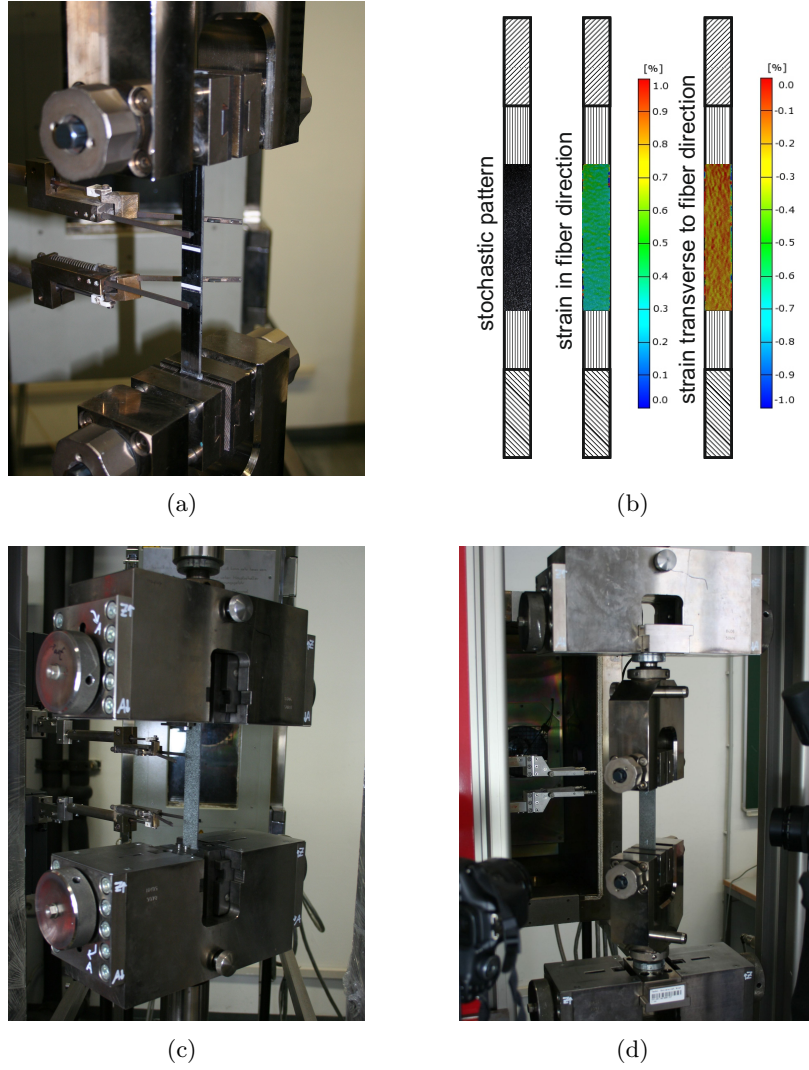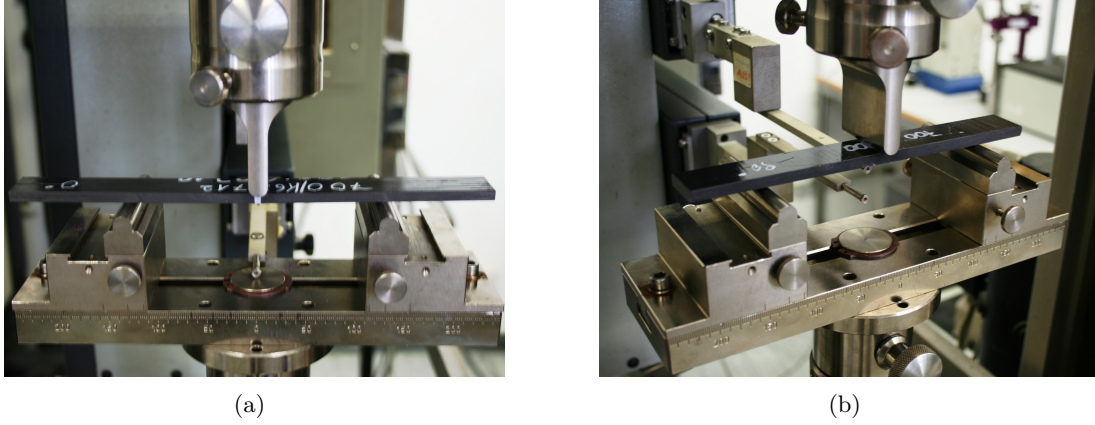Figure 3.9: Tension test setup using Zwick Z50 Universal Testing System: (a) unidirectional 0°; (b) unidirectional 0° strain measurement using DIC; (c) bidirectional ±45° specimen showing the stochastic pattern; (d) unidirectional 90° and the two camera setup for strain measurement by DIC in two planes.

The shear stress τ_{12} and the shear deformation γ are calculated as follows

$$\tau_{12} = \frac{F}{2A_0}, \quad \gamma = \varepsilon_l - \varepsilon_q .$$ (3.26)

The shear modulus G_{12} is calculated analogous to the Young's modulus by use of shear deformations $\gamma_1 = 0.001$ and $\gamma_2 = 0.005$.

The shear stress τ_{23} and the shear modulus G_{23} are calculated with the assumption

(a)   (b)

Figure 3.10: 3-point bending test setup using Zwick Z50 Universal Testing System: (a) unidirectional 0°; (b) unidirectional 90°.

of transversely isotropic behavior using the shear deformation $\gamma_{23} = \varepsilon_2 - \varepsilon_3$

$$G_{23} = \frac{E_2}{2(1+\nu_{23})} \; , \tag{3.27}$$

$$\tau_{23} = G_{23}\gamma_{23} = \frac{E_2}{2(1+\nu_{23})}(\varepsilon_2 - \varepsilon_3) \; . \tag{3.28}$$

Compression Tests   The compression tests were performed using a Zwick Z50 Universal Testing System. The test conditions were different to the standardized test method due to the unavailable Celanese-clamping jaws, used in [82]. Therefore, ordinary clamping jaws with aiming position for zero slipping were used with no measurement of the strains. Hence, only the compression strength can be found using the same above mentioned assumptions for the tension test. During the test, the applied force F was measured by a load cell and the velocity of the crosshead travel was kept constant for all tests at $1\,\mathrm{mm/min}$.

3-Point Bending Tests   The 3-point bending test were performed using a Zwick Z50 Universal Testing System with a support length to thickness ratio $L/h = 20$ and the radii of the contact points are $R_1 = R_2 = 5\,\mathrm{mm}$, see Fig. 3.10. The applied force F was measured by a load cell and the velocity of the crosshead travel was kept constant for all tests at $1\,\mathrm{mm/min}$. During the test, the deflection s of the beam was recorded.
   The maximum bending stress σ [83] in the extreme fiber can be calculated using

$$\sigma = \frac{3FL}{2bh^2}\left(1 + 6\left(\frac{s}{L}\right)^2 - 3\left(\frac{sh}{L^2}\right)\right) \; , \tag{3.29}$$

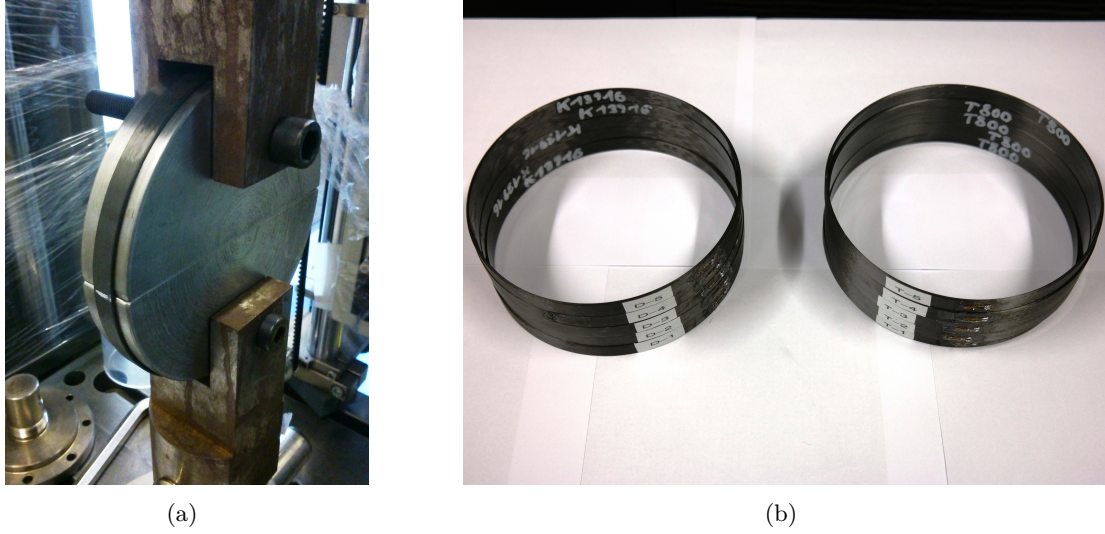(a)   (b)

Figure 3.11: Split disc test setup using Zwick Z250 Universal Testing System: (a) semi-circular steel discs; (b) ring specimen.

where b is the width of the specimen. The corrected strain ε [83] for large deflections is expressed as

$$\varepsilon = \frac{h}{L}\left(6\frac{s}{L} - 24.37\left(\frac{s}{L}\right)^3 + 62.17\left(\frac{s}{L}\right)^5\right) \ . \tag{3.30}$$

3.3.3 Testing of Ring Specimen

The split disc test was performed using a Zwick Z250 Universal Testing System, see Fig. 3.11. The two semicircular steel discs were well centered within the load transfer elements that transmit the pulling force F using steel bolts to guarantee a bending free support.

The applied force was measured by a load cell and the velocity of the crosshead travel was kept constant for all tests at $1\,\mathrm{mm/min}$. The hoop stress σ of the ring specimen is given by the applied force F and the cross-section surface A_0

$$\sigma = \frac{F}{2A_0} \ . \tag{3.31}$$

Furthermore, the hoop strain ε was measured using Hottinger Baldwin Messtechnik (HBM) strain gauges with a resistance of $120\,\Omega$ in quarter bridge operation that were directly applied at the outer specimen surface. The sampling rate was set to $f_S = 5\,\mathrm{Hz}$.
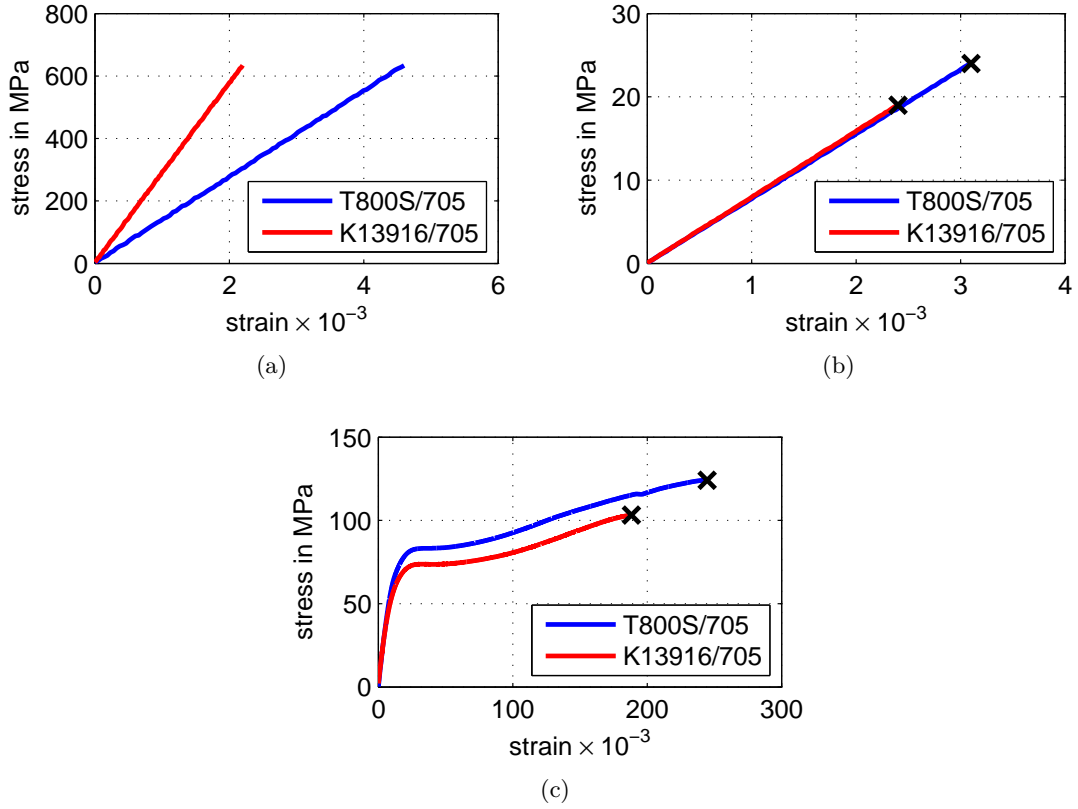
Figure 3.12: Tension stress-strain relation of the investigated materials: (a) unidirectional 0°; (b) unidirectional 90°; (c) bidirectional ±45°.

3.3.4 Analysis of Results

Tension Tests The results of the tension tests are depicted in Fig. 3.12. The unidirectional 0° specimen were tested in two steps, firstly pure elastic with the Zwick Z50 to measure the strain and Young's modulus, see Fig. 3.12(a) and secondly with the Zwick Z250 until failure to measure the ultimate strength without strain measurement.

In general, the expected high modulus and high strength characteristic of the investigated materials was observed. Both materials show an ideal elastic behavior until failure occurs. The T800S/705 specimen reaches the highest strength whereas the K13916/705 specimen reaches the highest stiffness. The failure of the specimen is for both materials an explosive event. The T800S/705 specimen tend to splice in bundles with the thickness of the used roving denoted as brittle failure with debonding and/or matrix cracking and the K13916/705 specimen split in large pieces denoted as brittle failure, see Fig. 3.13.

The unidirectional 90° specimen show for both materials very low strengths compared to the 0° specimen, see Fig. 3.12(b). In this configuration the material behavior is matrix dominated that can also be observed for the stiffness. In fact, by knowing the
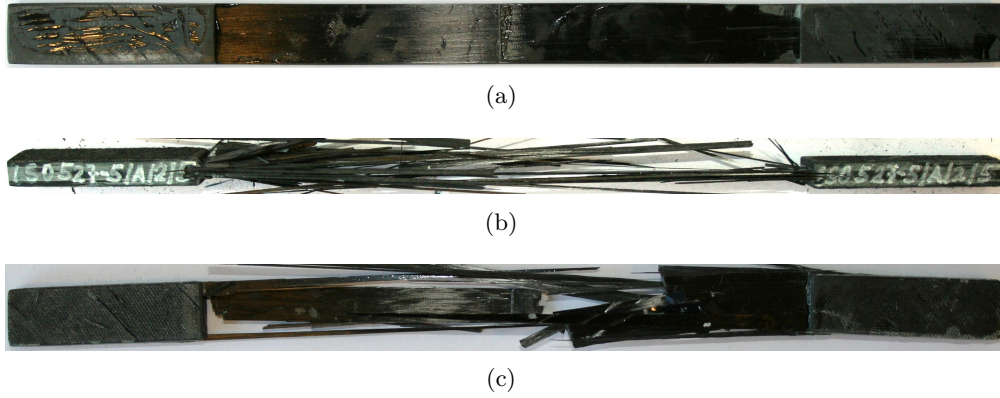
(a)

(b)

(c)

Figure 3.13: Failure of unidirectional 0° tension tested specimen: (a) initial geometry; (b) T800S/705; (c) K13916/705.
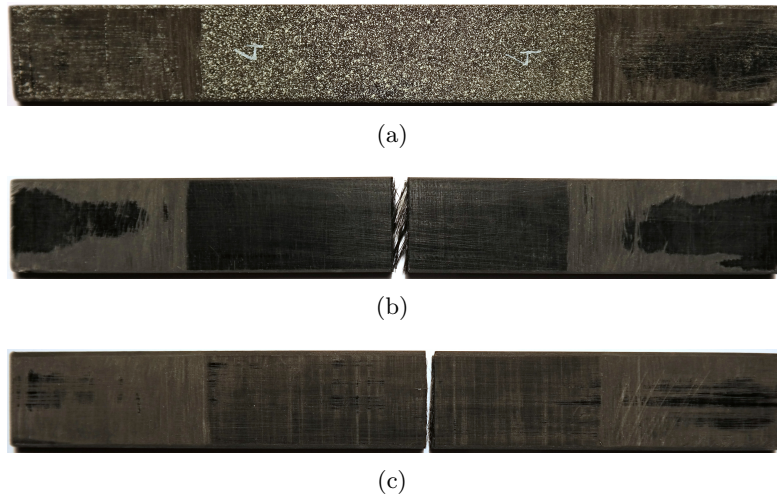

(a)

(b)

(c)

Figure 3.14: Failure of unidirectional 90° tension tested specimen: (a) initial geometry; (b) T800S/705; (c) K13916/705.

matrix 705 strength of about 72 MPa, the fiber matrix bond or the void content due to manufacturing is the reason for 60% less strength compared to the pure matrix. The investigated materials show the same failure mode that is identified as matrix cracking, see Fig. 3.14.

The results for the bidirectional ±45° specimen are depicted in Fig. 3.12(c). At the beginning both materials behave linear elastic followed by a non-linear rising due to progressive damage of the material. This is a result of the irreversible reorientation of the fibers. The failure mode in this case is delamination and inter-fiber failure for both materials, see Fig. 3.15. The results of all tension tests are summarized in Table 3.8.
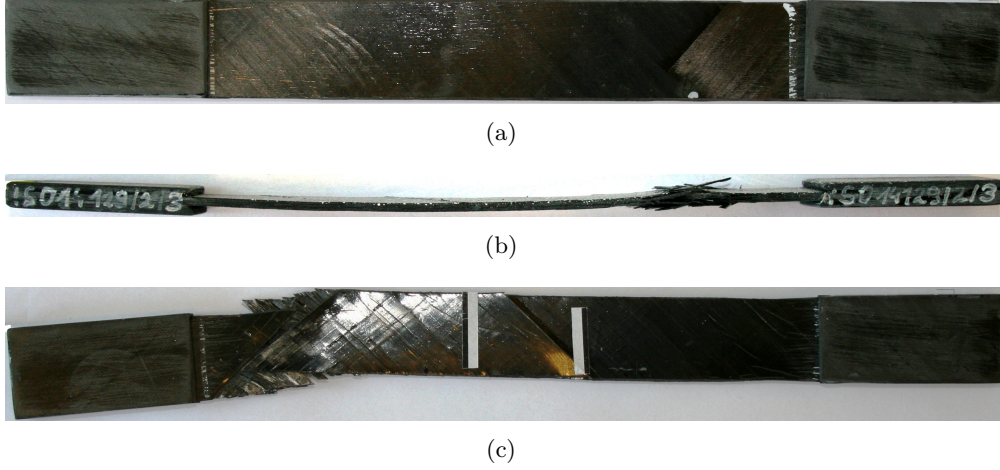
(a)

(b)

(c)

Figure 3.15: Failure of bidirectional ±45° tension tested specimen: (a) initial geometry; (b) T800S/705; (c) K13916/705.

Compression Tests The compression tests were performed without strain measurement. The unidirectional 0° tests were unsuccessful due to the wrong clamping unit resulting in a slipping of the specimen. Therefore, the 3-point bending test was used to evaluate the compression strength in fiber direction, explained in the following.

The unidirectional 90° specimen show nearly the same compression strength for both materials that is again matrix dominated. The failure mode of the specimen is shear dominated resulting in a matrix crack under an slight angle, see Fig. 3.16. The results of the compression tests are summarized in Table 3.9.

3-Point Bending Tests The unidirectional 0° specimen showed at the beginning an ideal linear elastic behavior followed by a short non-linear region until failure occurs,

Table 3.8: Material parameters obtained by tension tests.

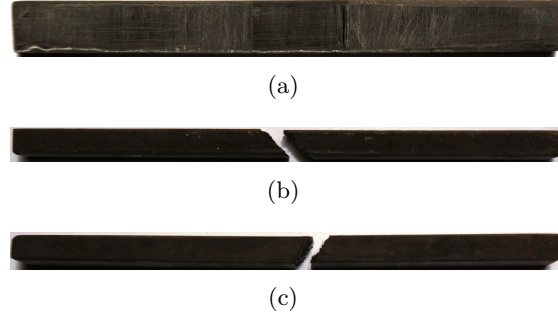|	T800S/705	K13916/705
E_1, GPa	139	290
E_2, GPa	7.8	7.9
ν_{12}	0.41	0.4
ν_{23}	0.38	0.4
G_{12}, GPa	3.4	3.3
X_t, MPa	2200	1300
Y_t, MPa	24	19
S_{12}, MPa	57	25
S_{23}, MPa	14	14

Figure 3.16: Failure of unidirectional 90° compression tested specimen: (a) initial geometry; (b) T800S/705; (c) K13916/705.
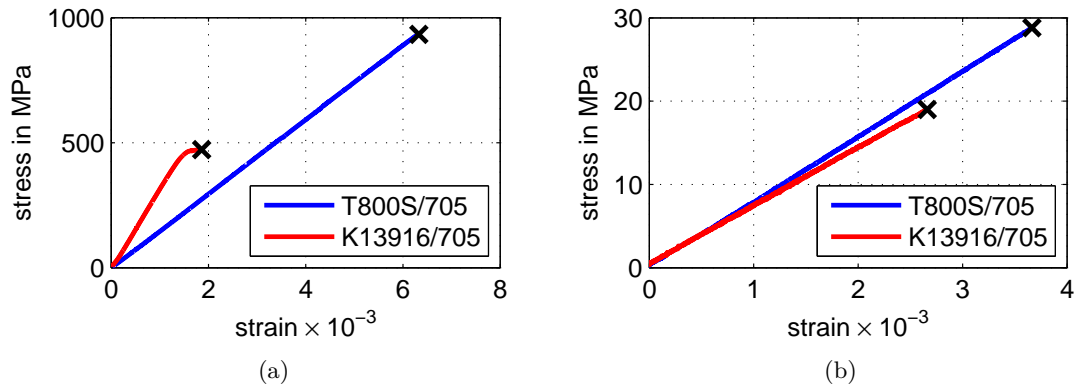

Figure 3.17: Bending stress-strain relation of investigated materials: (a) unidirectional 0°; (b) unidirectional 90°.

see Fig. 3.17(a). The failure starts at the load application point that is an indicator for a failure because of compressive stress. Due to the nature of the 3-point bending test, transverse forces are present at this point that lead to the assumption that the identified compressive strengths are lower than to the pure bending case. Furthermore it could be observed that the compressive strength is about 50% of the tensile strength. The brittle failure of the investigated materials is depicted in Fig. 3.18.

The results for the unidirectional 90° specimen are depicted in Fig. 3.17(b). Both materials behave linear with nearly identical stiffness. The failure occurs at the tension side due to matrix cracking of the specimen resulting in a similar failure surface shown

Table 3.9: Material parameters obtained by compression tests.

	T800S/705	K13916/705
Y_c, MPa	113	105

(a)

(b)

(c)

(d)   (e)
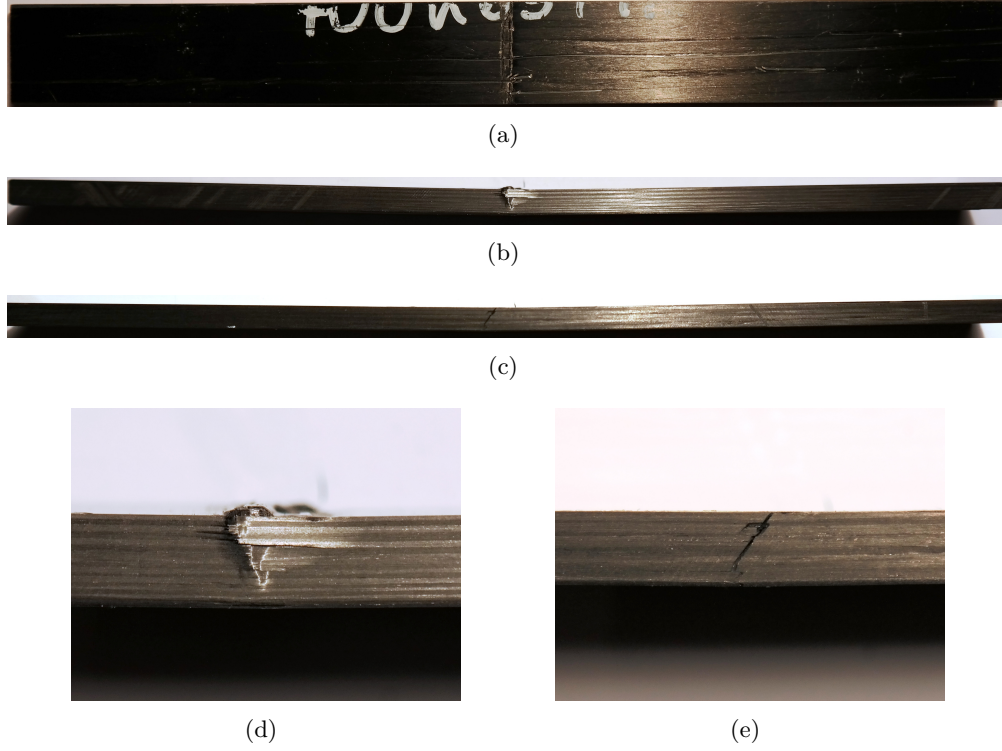
Figure 3.18: Failure of 3-point bending unidirectional 0° specimen: (a) initial geom-
etry; (b) T800S/705; (c) K13916/705; (d) T800S/705 failure detail; (e)
K13916/705 failure detail.

in Fig. 3.14. The results for the tension strength compare well to the tension tests. The
identified material parameters are summarized in Table 3.10.

Split Disc Test   The results of the split disc tests of the hoop wound specimen are de-
picted in Fig. 3.19. The non-linearity at the beginning is the result of an oval deformation
that leads to compression of the strain gauge due to bending. After the alignment with
the semicircular discs the expected high modulus and high strength characteristics of
the investigated materials can be seen. Both materials show an ideal elastic behavior
until the failure occurs. The T800S/705 specimen reaches the highest strength whereas
the K13916/705 specimen reaches the highest stiffness.

Table 3.10: Material parameters obtained by 3-point bending tests.

	T800S/705	K13916/705
X_c, MPa	933	470
Y_t, MPa	28	18

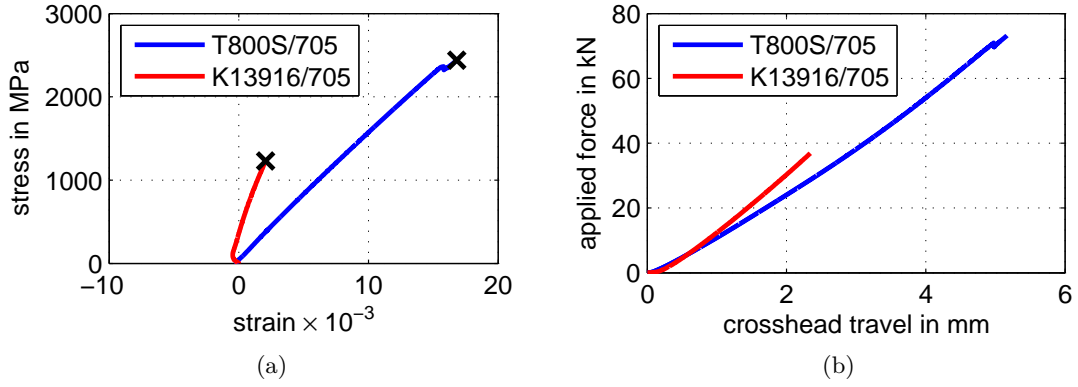(a)   (b)

Figure 3.19: Split disc test: (a) stress-strain relation of investigated materials; (b) applied force-crosshead travel relation of investigated materials.

(a)   (b)

Figure 3.20: Failure of split disc test hoop wound ring specimen: (a) T800S/705; (b) K13916/705.

The explosive failure characteristics is similar to the tension tests for all specimen. The T800S/705 specimen tend to splice in bundles with the thickness of the used roving denoted as brittle failure with debonding and/or matrix cracking and the K13916/705 specimen split in large pieces denoted as brittle failure, see Fig. 3.20. The identified material parameters are summarized in Table 3.11 and compare well to the unidirectional $0°$ tension tests.

Table 3.11: Material parameters obtained by split disc tests.

	T800S/705	K13916/705
E_1, GPa	149	320
X_t, MPa	2250	1250

3.4 Nondestructive vs. Destructive Material Parameter Determination

The nondestructive material parameter identification is used to determine the elastic material properties of UDCFRP plates, that is possible with one measurement, whereas the destructive material testing is used to determine the elastic and strength material properties of UDCFRP flat coupon specimen, but therefore at least 25 measurements are needed. If the focus is only on the elastic parameters, the destructive material testing needs 15 measurements. Both material parameter determinations have in common that the test specimen have the same basic rectangular geometry that are manufactured in the same way using filament winding.

In the following, the elastic parameters are compared for the high strength T800S/705 and the high modulus K13916/705 specimens. The results are summarized in Table 3.12. There, the relative errors are in relation to the results of the destructive material testing that are the true values with a statistical power of five. It can be seen that the discrepancies are all larger than 6% for the MDI-method as well as the II-method. The most problematic parameters are the Poisson's ratio ν_{12} and the shear modulus G_{12} with a relative error up to 74%.

The most obvious reason for these huge discrepancies lies in the quality of the measurement using a LSV and due to the influence of the non-perfect applicable boundary conditions. Anyway, both nondestructive methods are a good alternative to characterize the material in relation to the stiffness in fiber and transverse to the fiber direction.

Table 3.12: Nondestructive vs. destructive material parameter determination.

T800S/705	Destructive material testing	MDI-method FS	Relative error in %	II-method FS/PCS	Relative error in %
E_1, GPa	139.0	125.2	-10	122.8/153.1	-12/10
E_2, GPa	7.8	7.3	-6	6.4/8.9	-18/14
ν_{12}	0.41	0.458	12	0.275/0.498	-33/22
G_{12}, GPa	3.4	4.1	21	5.4/5.9	59/74
K13916/705	Destructive material testing	MDI-method FS	Relative error in %	II-method FS/PCS	Relative error in %
E_1, GPa	290.0	310.3	7	338.9/355.2	17/23
E_2, GPa	7.9	4.8	-39	4.8/5.0	-39/-37
ν_{12}	0.4	0.426	7	0.429/0.452	7/13
G_{12}, GPa	3.3	2.4	-27	2.0/5.2	-39/58

4 Static Testing Of Rotating Structures

4.1 Introduction

Within this chapter a flywheel static burst test (FSBT) method for composite flywheel rotors, already published in [85], is presented. This method is a safe alternative to a dynamic spin test, and because of the quasi-static loading the burst event is better controllable and observable. Another advantage is the better possibility to analyze the burst fragments, e.g. by a scanning electron microscope (SEM). Thereby, a much more dangerous and expensive dynamic spin up test with possible uncertainties can be substituted.

4.2 Feasibility Study

The method is a result of many different approaches that have been analyzed through static FE simulations compared to a previously optimized inertia mass geometry made of CFRP as a starting point, as presented in [86, 87]. The optimized topology of this inertia mass is depicted in Fig. 4.1.

In a first step, the starting point is analyzed to study the failure characteristics and to find out the position of the burst event. Therefore, a FE model was built up in the FE software COMSOL ([68]), (for details see [74]). There, the stress analysis was carried out with the quadratic Tsai-Wu criterion [73] and the material parameters summarized in [86]. The results showed a maximum of the Tsai-Wu parameter on the inner radius between the shaft interface and the cantilever part of the CFRP inertia mass, see Figure 4.2(i). The failure forcing component is the radial stress component due to the inertial load. These results are the requirements for the FSBT: (1) quantitatively the same stress state and deformation characteristics, (2) the predicted failure point has to be identical.

In a second step, a feasibility study was performed using the given restrictions. Thereby, the testing method must be feasible by applying external forces, which is in general not possible due to volume forces given by the inertial load. Therefore, many possibilities and also the use of similar geometries were studied to find an appropriate test method that best reflects reality. Figure 4.2 shows the results that are further explained below.

- For rotating structures with low thickness to radius ratio, it is possible to simulate the inertial load by use of pressure load applied onto the inner contour. Therefore, the first approach uses high hydraulic pressure which models the internal high pressure forming process. The problem with this method is a different failure point, see Fig. 4.2(a).
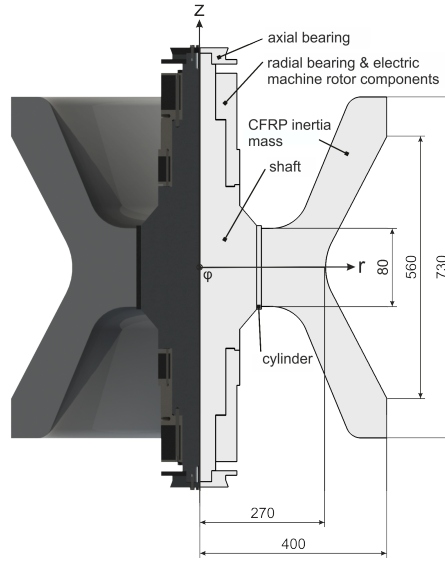
Figure 4.1: Flywheel rotor consisting of the CFRP inertia mass, shaft (aluminium), bearing and motor components (soft magnetic iron) and a steel cylinder to optimize the press-fitting process; dimensions in mm.

- This method uses force loading applied onto the top surface of the inertia mass. Therefore, a huge force is needed that can be applied by heavy stamping or hydraulic presses. The deformation shows the expected behavior, but the failure point is different, see Fig. 4.2(b).

- This method is similar to the previous explained, but now the inertia mass is isotropic scaled by a factor of $\chi = 0.5$ and so the needed force can be drastically reduced by a factor of 0.25, see Fig. 4.2(c).

- Figure 4.2(d) shows a similar geometry where also a force load acts on the top surface. The deformation characteristics and failure point are acceptable but the manufacturing by filament winding is almost impossible.

- The geometry for the next method is further changed by varying the cantilever part and radii to get a symmetric geometry. The advantage for this method is, that only half of the inertia mass must be manufactured. The problem with this method is also a different failure point, see Fig. 4.2(e).

- This method is similar to the previous explained, but now the thickness is further reduced. The deformation characteristics and failure point are acceptable, but applying of any measuring equipment inside is tricky, see Fig. 4.2(f).

- Figure 4.2(g) shows a well simplified geometry that covers all collected knowledge of the above described methods. The problem with this configuration is the tricky manufacturing of thin slices by wet filament winding.

- The result of a completely reconsideration, by applying loads in hoop direction, can be seen in Fig. 4.2(h). Here, an isotropic scaled ($\chi = 0.4$) equivalent of the inertia mass in Fig. 4.1 is cutted on the mid plane on one side to apply a force load onto this surface. The resulting deformation characteristics and failure point are nearly identical to the result in Fig. 4.2(i) and is therefore the chosen test method.
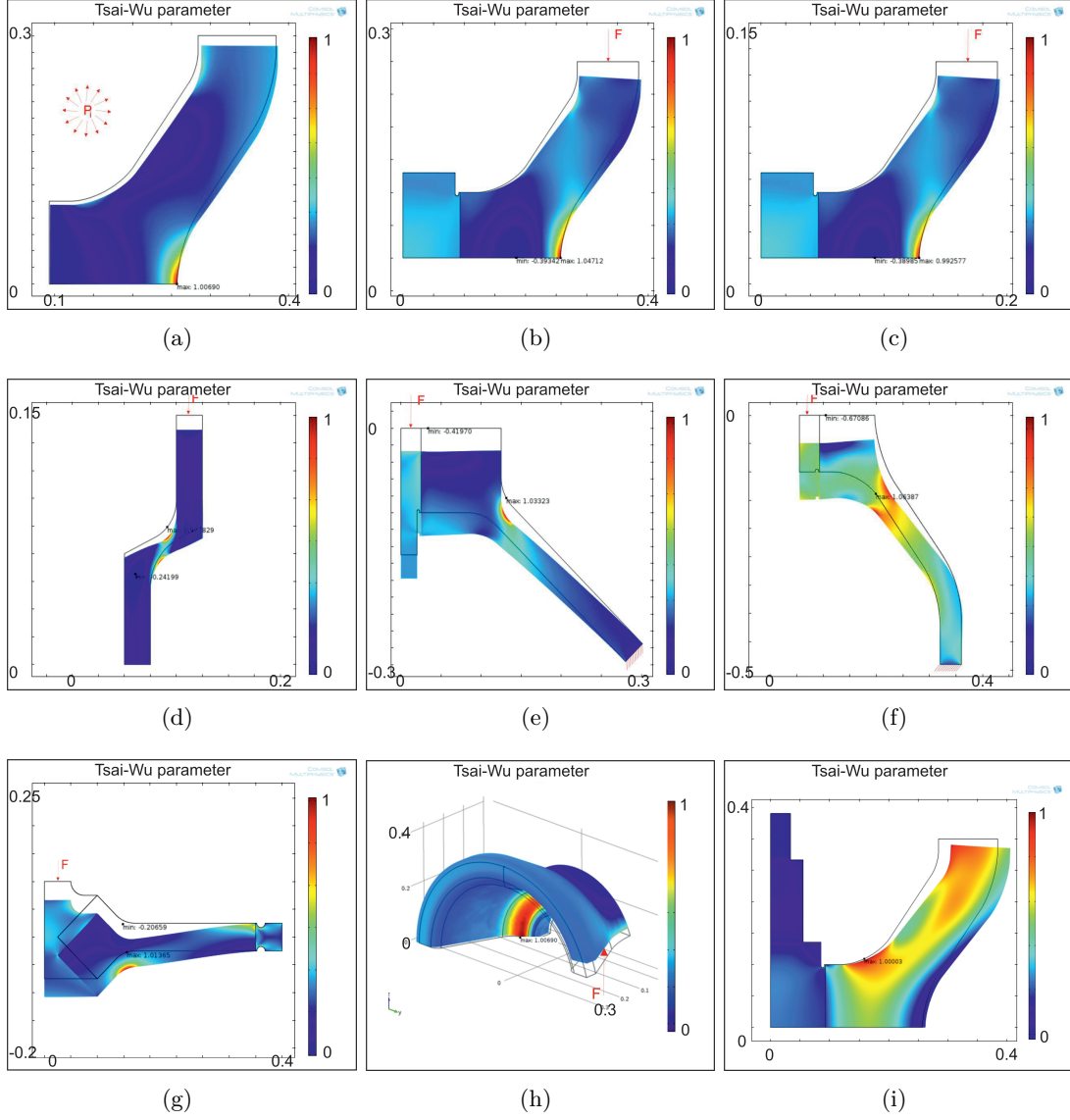

Figure 4.2: Test methods out of [74], deformation scale = 5 and dimensions in m: (a) pressure $p_i = 985\,\text{bar}$; (b) force $F = 17.5\,\text{MN}$; (c) force $F = 4.3\,\text{MN}$; (d) force $F = 3.3\,\text{MN}$; (e) force $F = 2.9\,\text{MN}$; (f) force $F = 9\,\text{MN}$; (g) force $F = 1.2\,\text{MN}$; (h) force $F = 250\,\text{kN}$; (i) starting point result at $\omega = 2200\,\text{s}^{-1}$.
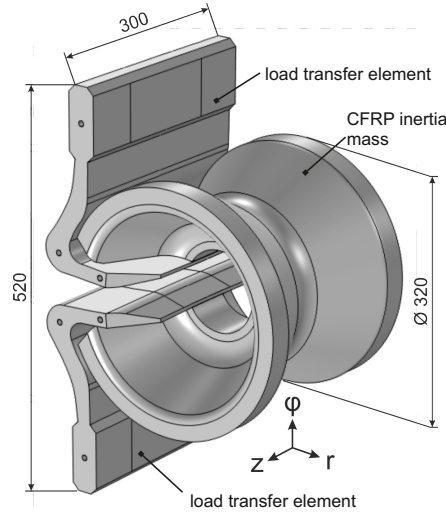
Figure 4.3: FSBT geometry consisting of the load transfer elements (steel) and the CFRP inertia mass; dimensions in mm.

4.3 Static Burst Test Approach

The developed FSBT uses the CFRP inertia mass of the optimized FESS rotor, as shown in Fig. 4.3, to test exactly the same equivalent cutted geometry in a static way. To reduce the required pulling force, e.g. provided by a tensile test machine, an isotropic geometry scaling factor of $\chi = 0.4$ for the CFRP inertia mass is used.

Therefore, a 250 kN universal tensile test machine can be used to burst the CFRP rotor. A difference to the dynamic case is the absence of the whole shaft and steel components. This can influence the results, but as prestressing due to thermal press-fitting increases loading capability [88], the FSBT is a more conservative test method.

Design and Topology Optimization of Load Transfer Elements   The design space for applying the pulling force load F is limited due to the cut out and mounting space inside the universal tensile test machine.

Furthermore, it is necessary to optimize the load transfer elements for maximum stiffness in pulling direction to optimally transfer the applied load from the machine to the test specimen. This optimization was carried out by using the FE software COMSOL [68] performing the solid isotropic material with penalization (SIMP) method [89, 90].

The design space is discretized by quadrilateral $N = 5500$ finite elements with bilinear basis functions, see Fig. 4.4(a). Thereby, each non-dimensional element density ρ_i (running from 0 to 1) is a design variable forming the vector of optimization variables $\boldsymbol{x} = (\rho_1, \rho_2, ..., \rho_N)^t$. For any continuum structure represented by finite elements including boundary conditions, the topology optimization problem using the SIMP algorithm for minimizing the total strain energy reads as
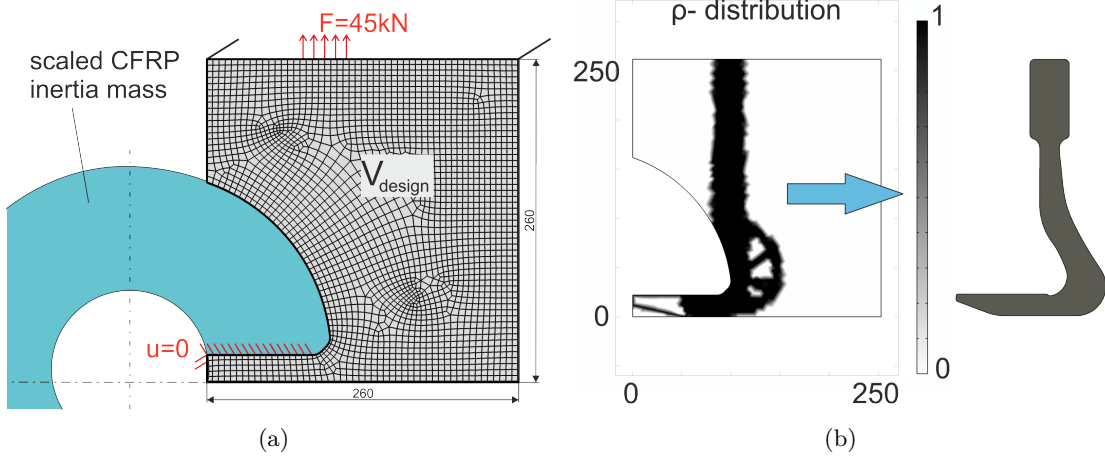
Figure 4.4: Topology optimization of the load transfer elements, dimensions in mm: (a) design space; (b) resulting black/with topology for $p = 4$ and $V_0 = 20\%$ of V_{design}.

$$\min_{\boldsymbol{x}} \left\{ \boldsymbol{u}^T \boldsymbol{K} \boldsymbol{u} \right\} = \min_{\boldsymbol{x}} \left\{ \sum_{j=1}^{N} \boldsymbol{u}_j^T \boldsymbol{K}_j \boldsymbol{u}_j \right\} = \min_{\boldsymbol{x}} \left\{ \sum_{j=1}^{N} \boldsymbol{u}_j^T \boldsymbol{\rho}_j^p K_e \boldsymbol{u}_j \right\}, \qquad (4.1)$$

$$s.t. \qquad \sum_{j}^{N} \rho_j V_j \leq V_0 \,,$$

$$0 < \rho_{\min} \leq \rho \leq 1.0 \,,$$

where $\boldsymbol{u}$ is the nodal displacements vector and $\boldsymbol{K}_j$ is the stiffness matrix of the jth element formed by the initial element stiffness matrix $\boldsymbol{K}_e$ modulated by ρ_j and the penalization power p, which can take any value greater than one. Therefore, the element stiffness matrix can vary in magnitude from a minimum (void element) to a maximum (solid element).

The topology optimization was performed using a plain strain FE simulation with the load, boundaries, material parameter (steel) and design space, shown in Fig. 4.4(a). The use of penalization powers $p \leq 3$ results in a black/white (solid/void) topology that is very desirable for further construction. Hence, differing penalization powers p and maximum volumes V_0 were studied and it showed up, that for decreasing maximum volumes V_0 the optimization starts to form local holes that is of no practical use for the following manufacturing. Therefore, the limit configuration with $p = 4$ and $V_0 = 20\%$ of V_{design} , shown in Fig. 4.4(b), is simplified and a stress analysis is performed to select a steel type with a suitable ultimate strength. The load transfer elements were cutted out of steel plates using a waterjet and then welded together to achieve the required width of $300\,\text{mm}$. The milled finished elements are shown in Fig. 4.5.
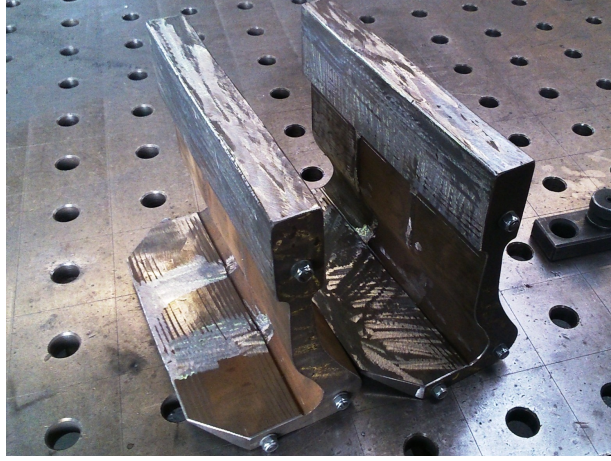
Figure 4.5: Welded and milled load transfer elements.

Modeling of the CFRP Inertia Mass   In the following simulations a hoop wound structure using a filament winding process with a fiber angle of 90° between the fibers and the axis of rotation is assumed. Hence, the stiffness tensor $\boldsymbol{E}$ and its entries, given in Eqs. (4.2), (4.3) and (4.4), can be expressed by use of five independent constants, given and described in Table 4.1.

$$
\boldsymbol{E} =
\begin{bmatrix}
E_{\varphi\varphi} & E_{\varphi r} & E_{\varphi z} & 0 & 0 & 0 \\
 & E_{rr} & E_{rz} & 0 & 0 & 0 \\
 & & E_{zz} & 0 & 0 & 0 \\
 & & & G_{rz} & 0 & 0 \\
 & sym. & & & G_{\varphi r} & 0 \\
 & & & & & G_{\varphi r}
\end{bmatrix}
\tag{4.2}
$$

$$
\Delta = \frac{1 - 2\nu_{\varphi r}\nu_{r\varphi} - 2\nu_{r\varphi}\nu_{rz}\nu_{\varphi r} - \nu_{rz}^2}{E_\varphi E_r^2}
\tag{4.3}
$$

$$
\begin{aligned}
G_{rz} &= \frac{E_r}{2(1 + \nu_{rz})}, & \frac{\nu_{ij}}{E_i} &= \frac{\nu_{ji}}{E_j}, \quad i,j = \varphi, r, z \ , \\
E_{\varphi\varphi} &= \frac{1 - \nu_{rz}^2}{E_r^2 \Delta}, & E_{\varphi r} &= \frac{\nu_{r\varphi} + \nu_{r\varphi}\nu_{rz}}{E_r^2 \Delta}, \\
E_{rr} &= \frac{1 - \nu_{\varphi r}\nu_{r\varphi}}{E_\varphi E_r \Delta}, & E_{rz} &= \frac{\nu_{rz} + \nu_{\varphi r}\nu_{r\varphi}}{E_\varphi E_r \Delta}, \\
E_{zz} &= \frac{1 - \nu_{\varphi r}\nu_{r\varphi}}{E_\varphi E_r \Delta}, & E_{\varphi z} &= \frac{\nu_{r\varphi} + \nu_{r\varphi}\nu_{rz}}{E_r^2 \Delta} \ .
\end{aligned}
\tag{4.4}
$$

Stress Analysis To investigate the failure of the following described models, several failure criteria have been used. For simple evaluating of material failure the maximum stress criteria expressed in Eq. (4.5) can be applied. Once the normal stress in principal material directions (radial, hoop, rz-plane) reach their corresponding maximum strengths (X_t, Y_t, S_{23}), material failure can be expected.

$$\frac{\sigma_r}{Y_t} \geq 1, \quad \frac{\sigma_\varphi}{X_t} \geq 1, \quad \frac{\sigma_{rz}}{S_{23}} \geq 1 \ . \tag{4.5}$$

This criterion does not consider interactions between the stress components of the given stress state. For a more reliable failure estimation with consideration of the inter-stress effect, the generalized quadratic Tsai-Wu criterion [73] was considered, which reads as

$$\overline{\boldsymbol{F}}^T \boldsymbol{\sigma} + \boldsymbol{\sigma}^T \widetilde{\boldsymbol{F}} \boldsymbol{\sigma} \geq 1 \ . \tag{4.6}$$

Table 4.1: Material data for T800S/705 specimens with a fiber volume fraction of 60 % and metal material data used for simulation.

T800S/705		
Elastic modulus radial r, GPa	E_r^*	7.8
Elastic modulus hoop φ, GPa	E_φ^*	139
Elastic modulus axial z, GPa	E_z	7.8
Poissons ratio	$\nu_{\varphi r}^*$	0.41
Poissons ratio	ν_{zr}^*	0.38
Shear modulus φr, GPa	$G_{\varphi r}^*$	3.4
Tensile strength φ, MPa	X_t^*	2200
Compressive strength φ, MPa	X_c^*	1000
Tensile strength r, z, MPa	Y_t^*, Z_t	24
Compressive strength r, z, MPa	Y_c^*, Z_c	113
Shear strength φr, MPa	S_{12}^*	57
Shear strength φz, MPa	S_{13}	57
Shear strength rz, MPa	S_{23}	14
Steel		
Elastic modulus, GPa	E_{St}	210
Poissons ratio	ν_{St}	0.3
Von Mises strength, MPa	$\sigma_{V,St}$	690
Aluminium		
Elastic modulus, GPa	E_{Al}	70
Poissons ratio	ν_{Al}	0.3
Von Mises strength, MPa	$\sigma_{V,Al}$	500

* obtained by measurements.

The stress state vector $\boldsymbol{\sigma}$ and $\overline{\boldsymbol{F}}$, $\widetilde{\boldsymbol{F}}$ the second and fourth order tensor of the strength parameters out of Table 4.1 are given as follows

$$
\boldsymbol{\sigma} = \begin{bmatrix} \sigma_\varphi \\ \sigma_r \\ \sigma_z \\ \sigma_{rz} \\ \sigma_{\varphi z} \\ \sigma_{\varphi r} \end{bmatrix}, \quad \overline{\boldsymbol{F}} = \begin{bmatrix} F_1 \\ F_2 \\ F_3 \\ 0 \\ 0 \\ 0 \end{bmatrix}, \tag{4.7}
$$

$$
\widetilde{\boldsymbol{F}} = \begin{bmatrix} F_{11} & F_{12} & F_{13} & 0 & 0 & 0 \\ & F_{22} & F_{23} & 0 & 0 & 0 \\ & & F_{33} & 0 & 0 & 0 \\ & & & F_{44} & 0 & 0 \\ & & & & F_{55} & 0 \\ sym. & & & & & F_{66} \end{bmatrix}, \tag{4.8}
$$

$$
\begin{aligned}
F_1 &= \frac{1}{X_t} - \left| \frac{1}{X_c} \right|, & F_2 &= \frac{1}{Y_t} - \left| \frac{1}{Y_c} \right|, \\
F_3 &= \frac{1}{Z_t} - \left| \frac{1}{Z_c} \right|, & F_{11} &= \left| \frac{1}{X_t X_c} \right|, \\
F_{22} &= \left| \frac{1}{Y_t Y_c} \right|, & F_{33} &= \left| \frac{1}{Z_t Z_c} \right|, \\
F_{44} &= \frac{1}{S_{23}^2}, & F_{55} &= \frac{1}{S_{13}^2}, \\
F_{66} &= \frac{1}{S_{12}^2}, & F_{12} &= -\frac{1}{2} \sqrt{F_{11} F_{22}}, \\
F_{13} &= -\frac{1}{2} \sqrt{F_{11} F_{33}}, & F_{23} &= -\frac{1}{2} \sqrt{F_{33} F_{22}} \, .
\end{aligned} \tag{4.9}
$$

Finite Element Models The axisymmetric geometry of the nonlinear quasi-static model of the rotor is discretized by quadrilateral finite elements with bilinear basis functions and using the $r\varphi$-symmetry plane as roller boundary condition, see Fig. 4.6(a). The CFRP inertia mass is assumed to be transversely isotropic in hoop direction. In Table 4.1 the used material parameters for the CFRP inertia mass and the shaft components are summarized.

The stress state of this FESS rotor was calculated in two steps. In the first step the thermal shrink fit of the shaft onto the rotor and in the second step the inertial loads due to rotation was computed.

For static FE simulation of the FSBT, a 3-dimensional model of the isotropic scaled ($\chi = 0.4$) CFRP rotor (see Fig. 4.3) using two symmetry planes as roller boundary condition to reduce simulation effort has been used. The model is discretized by quadratic

tetragonal finite elements (see Fig. 4.6(c)) and the CFRP inertia mass is assumed to be transversely isotropic in hoop direction. The material parameters for the scaled CFRP inertia mass and load transfer elements made of steel are given in Table 4.1. Modeling of the contact between the load transfer elements and the rotor was neglected, as the observed failure point is far away from the contact area and therefore has minimal influence and so a linear simulation has been performed.

For both models a mesh convergence study has been performed to check for the influence of mesh type and size onto the Tsai-Wu criterion in the predicted failure point. Furthermore, a safety factor S is introduced as a proportional factor as follows

$$\boldsymbol{\sigma}^* = S\boldsymbol{\sigma} \ . \tag{4.10}$$

Thereby, S links the actual stress state $\boldsymbol{\sigma}$ and the stress state $\boldsymbol{\sigma}^*$ that causes material failure. Combining Eqs. (4.6) and (4.10) and defining $\boldsymbol{\sigma}^* = \boldsymbol{\sigma}$ results in a quadratic equation with the following (positive) solution for the safety factor

$$S = \frac{-\overline{\boldsymbol{F}}^T\boldsymbol{\sigma} + \sqrt{(\overline{\boldsymbol{F}}^T\boldsymbol{\sigma})^2 + 4\boldsymbol{\sigma}^T\widetilde{\boldsymbol{F}}\boldsymbol{\sigma}}}{2\boldsymbol{\sigma}^T\widetilde{\boldsymbol{F}}\boldsymbol{\sigma}}. \tag{4.11}$$

A safety factor of $S \leq 1$ indicates material failure. In the following stress analysis the maximum stress criteria and the inverse safety factor are used to study the burst event and the failure mode.

Stress Distributions The simulation results of the FESS rotor without considering the shaft region are shown in Fig. 4.6(a). The minimum safety factor ($S = 1$) appears on the inner radius between the shaft interface and the cantilever part of the CFRP rotor at a radial position of $r = 69\,\text{mm}$, see Fig. 4.6(b). The analysis of the maximum stress criterion along the dashed line illustrates that the radial stress σ_r is the critical factor.

A failure occurs when the rotor speed is increased over the value which leads to a safety factor of $S = 1$. This happens at a rotor speed of $\omega = 2590\,\text{s}^{-1}$, where the radial stress σ_r is equal to the maximum tensile strength Y_t, see Fig. 4.6(b).

The FSBT simulation results are depicted in Fig. 4.6(c). The minimum safety factor $S = 1$ can be found on the inner radius of the contour located at the used symmetry plane. The radial position is $r = 67\,\text{mm}$, see Fig. 4.6(d). If the load is increased above $43\,\text{kN}$, a failure occurs due to the radial stress σ_r that reaches the maximum tensile strength Y_t, see Fig. 4.6(d).

The results of the FSBT and the FESS rotor simulation show very good agreement, as shown in Fig. 4.6(b) and 4.6(d). The position, where the failure occurs, is nearly identical and so the main restriction is respected. The inverse safety factor shows one big difference at increasing radius. As one can see in Fig. 4.6(b), the curve is rising but is still lower than at the predicted failure point. The analysis shows that the safety factor can mainly be approximated by the combination of the radial- and hoop maximum stress criteria.
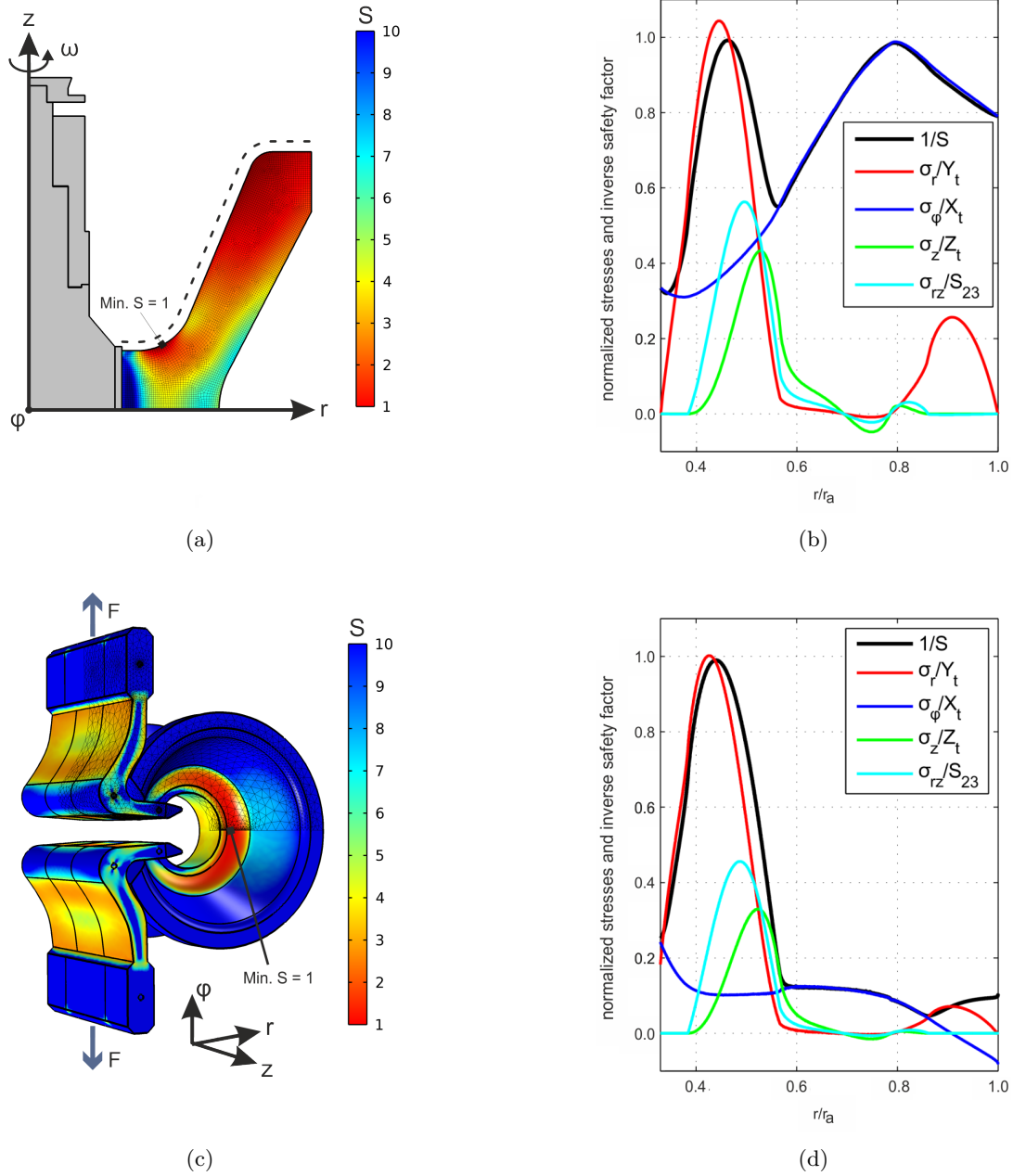
(a)

(b)

(c)

(d)

Figure 4.6: Simulation results: (a) FESS rotor, safety factor S evaluated at $\omega = 2590\,\mathrm{s}^{-1}$; (b) FESS rotor, normalized stresses and inverse safety factor evaluated at $\omega = 2590\,\mathrm{s}^{-1}$ on the upper boundary of the CFRP inertia mass, $r_a = 400\,\mathrm{mm}$; (c) FSBT, safety factor S evaluated at $F = 43\,\mathrm{kN}$; (d) FSBT, normalized stresses and inverse safety factor evaluated for $F = 43\mathrm{kN}$ on the upper boundary of the CFRP inertia mass, $r_a = 160\,\mathrm{mm}$. Safety factors calculated based on Eq. (4.11).

4.4 Manufacturing of the Specimen

The hoop wound scaled specimen of the FESS inertia mass was manufactured using the same wet filament winding technique with equal process parameters as used for the manufacturing of the specimens for material parameter identification, given in Table 4.2.

In total, a set of six T800S 12 K rovings were combined to achieve a band thickness of about 12 mm and a layer thickness of about 0.4 mm. Winding was done using an aluminium mandrel that has been CNC machined to get the inner rotor contour, see Fig. 4.7(a). The slight pretension force was kept constant at 20 N during the winding operation until the whole mandrel was filled, see Fig. 4.7(b).

After the winding operation, the specimen together with the mandrel were then placed into a temperature-controlled oven for curing, see Fig. 4.7(c). After curing and before removing the specimen from the mandrel the outer contour has been CNC machined.

The specimen was then pulled off the mandrel by a hydraulic cylinder and cutted through on one side to serve space for the load transfer elements, see Fig. 4.7(d).

4.5 Experimental Results

This section presents the results of a FSBT experiment on an isotropic scaled equivalent of the FESS inertia mass described above. The experiments were done in cooperation with the Institute of Materials Science and Technology at Vienna University of Technology. The section closes with a discussion of the overall results from the experiments and compares them to simulation results mentioned above.

Test procedure For tensile testing a Zwick Z250 Universal Testing System with a load capacity of 250 kN was used. The specimen was placed between the two well centered load transfer elements, see Fig. 4.8. During the tensile test, the test speed of the testing machine was kept constant at a level of 1 mm/min and the load and strain data were measured until failure of the specimen.

Table 4.2: Material and process parameters of fiber and resin.

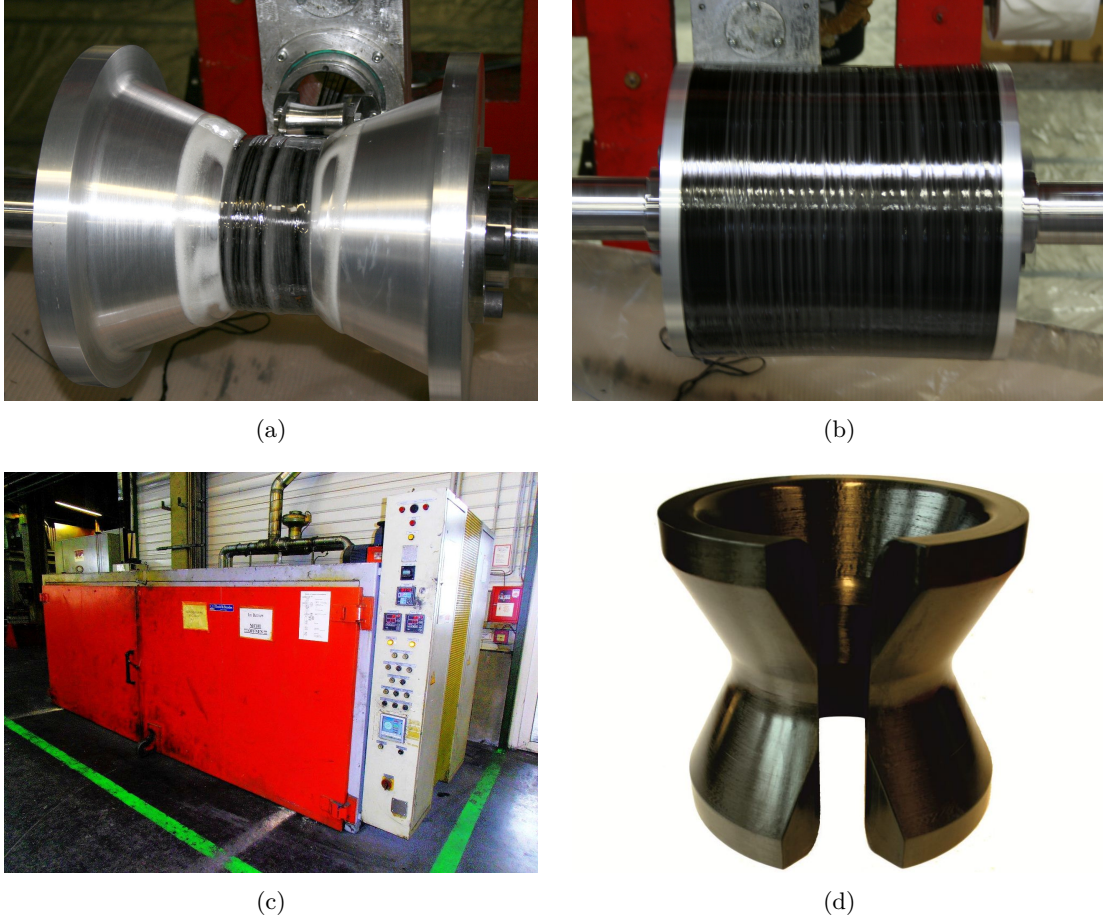| TORAY Torayca T800S	Matrix 705	
	Fiber	Resin
Tensile strength, MPa	5490	72
Tensile modulus, GPa	294	3.0
Elongation at break, %	1.9	4.9
Density, kg/m^3	1810	1100
Filament diameter, μm	5	-
Tow size	12K	-
Tex	445	-
Curing schedule	1st: 2h/80°C, 2nd: 6h/120°C, 3rd: 1h/60°C	

Figure 4.7: Fabrication of the test specimen: (a) aluminium mandrel; (b) finished winding operation; (c) temperature-controlled oven; (d) turned and milled specimen.

Strain Measurement The strains in radial-, hoop- and axial direction where measured by strain gauges on one side of the specimen directly at the location of the predicted failure point and optically by digital image correlation using a region of about $50\,\mathrm{mm}\times30\,\mathrm{mm}$ centered around the failure point on the other side of the specimen. Electrical and optical measurements were synchronized by measuring the crosshead travel of the testing machine.

Strain Gauge Measurement The used Hottinger Baldwin Messtechnik (HBM) $350\,\Omega$ strain gauge was directly applied at the predicted failure point, see Fig. 4.9(a). To measure the correct strain in radial- and hoop direction a strain gauge rosette with three measurement grids in $0°/45°/90°$ (strain ε_a, ε_b and ε_c) alignment, each in quarter bridge operation mode, was used.
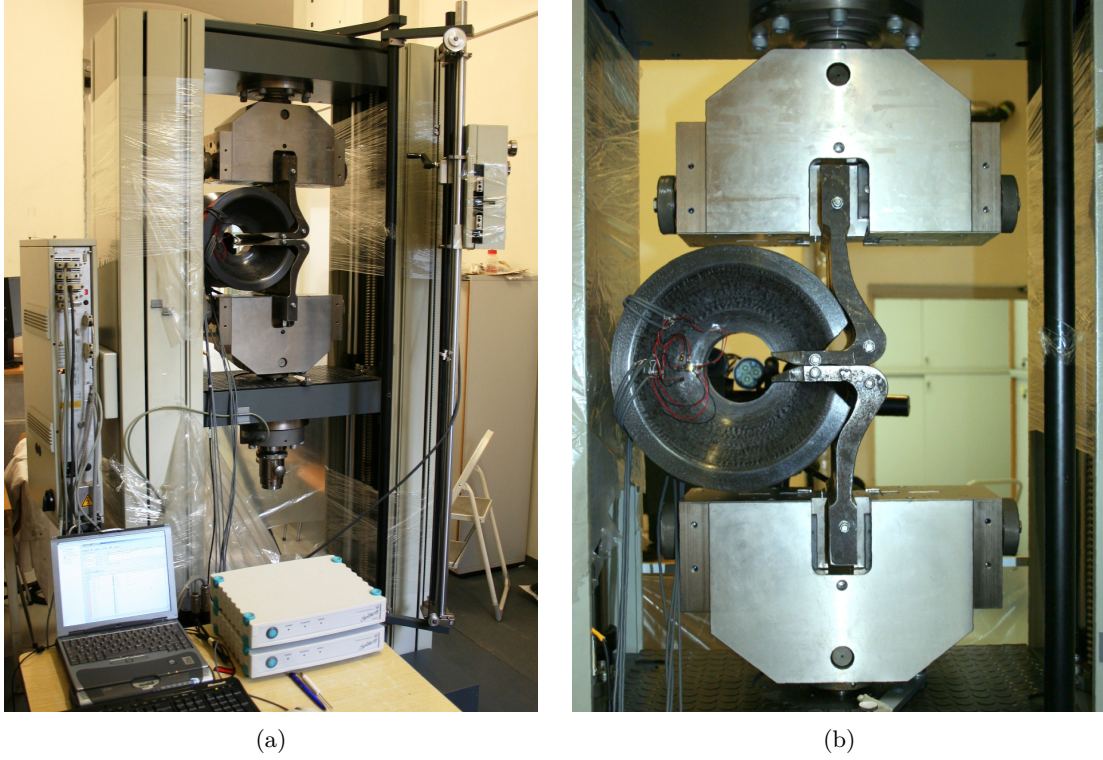
Figure 4.8: Test machine setup: (a) Zwick Z250 Universal Testing System; (b) load transfer elements and the scaled CFRP rotor.

By combination of the three measured strains the main strain direction angle ϕ and the main strain magnitudes ε_φ, ε_r are obtained by

$$\varepsilon_\Delta = \sqrt{2}\sqrt{(\varepsilon_a - \varepsilon_b)^2 + (\varepsilon_b - \varepsilon_c)^2}\,, \tag{4.12}$$
$$\phi = \tan^{-1}\left(\frac{\varepsilon_c - \varepsilon_a + \varepsilon_\Delta}{2\varepsilon_b - \varepsilon_a - \varepsilon_c}\right),$$
$$\varepsilon_\varphi = \frac{\varepsilon_a + \varepsilon_c}{2} + \frac{\varepsilon_\Delta}{2}\,,$$
$$\varepsilon_r = \frac{\varepsilon_a + \varepsilon_c}{2} - \frac{\varepsilon_\Delta}{2}\,.$$

The axial strain could not be measured at the predicted failure point. Instead, the $350\,\Omega$ strain gauge in quarter bridge operation was applied to the closest point on the innerst radius, as the simulation showed almost no difference between the analysis results of those two points. For data acquisition two HBM Spider8 amplifier with eight channels and the measurement software HBM Catman 3.0 were used, see Fig. 4.9(b). The crosshead travel was measured using a IL-065 position sensor. The sampling rate was set to $f_S = 5\,\text{Hz}$.
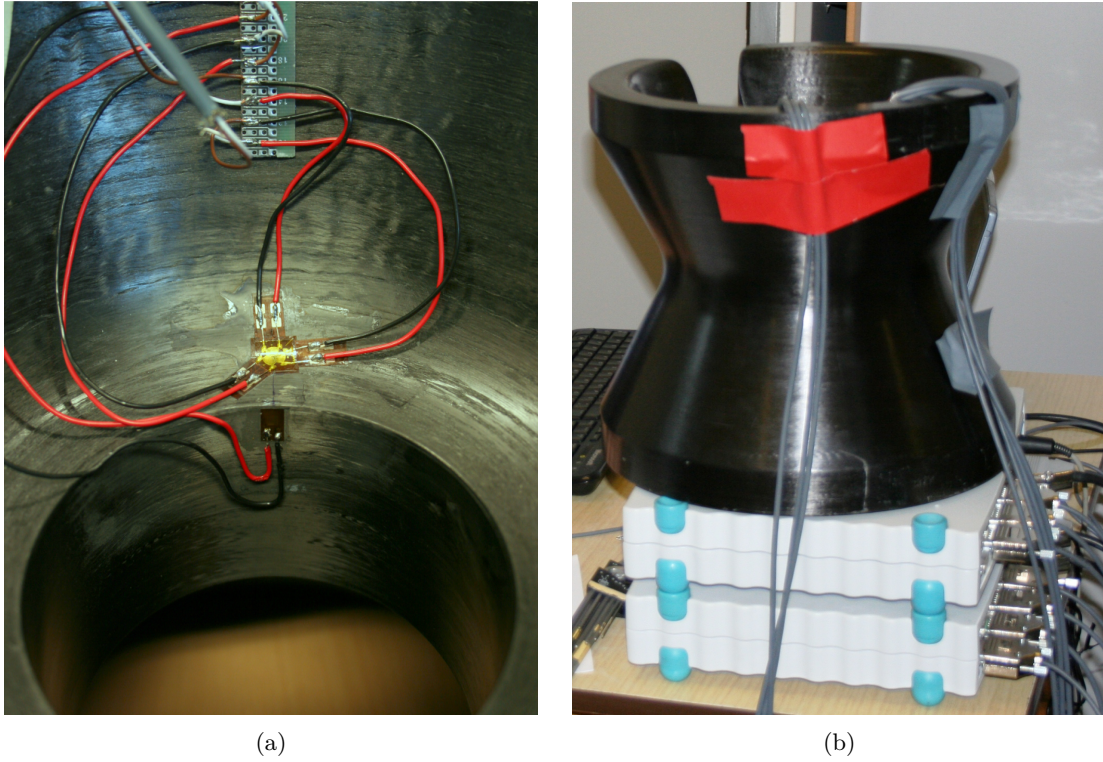
Figure 4.9: Three channel strain gauge at the predicted failure point: (a) measuring radial- and hoop strain, strain gauge on the inner radius to measure the axial strain; (b) HBM measurement equipment consisting of two eight channel HBM Spider8 amplifier.

Optical Strain Measurement Digital image correlation (DIC) was used to perform a non-contact deformation measurement. The DIC software used in this experimental work was the ARAMIS DIC system, developed by Gesellschaft für optische Messtechnik (GOM), see Fig.4.10(a).

The stereo vision system consists of two 1.3 mega pixel cameras located about 1 m in front of the universal tensile testing machine illuminated by two light sources to generate a better contrast.

The maximum acquisition frequency is $f_S = 6\,\mathrm{Hz}$ and the picture resolution is $445{\times}371$ pixels that results in a physical size of the pixel being of the order of 0.1 mm. By use of a white colored stochastic pattern spray painted on the specimen it was possible to measure the deformation field in three dimensions after calibration.

The calibration was performed with a calibration plate in absence of the test specimen while the midpoint of the calibration plate was positioned at the location of the predicted failure point, see Fig. 4.10(b). The deformation images and the crosshead travel were collected with a sampling rate of $f_S = 0.67\,\mathrm{Hz}$.
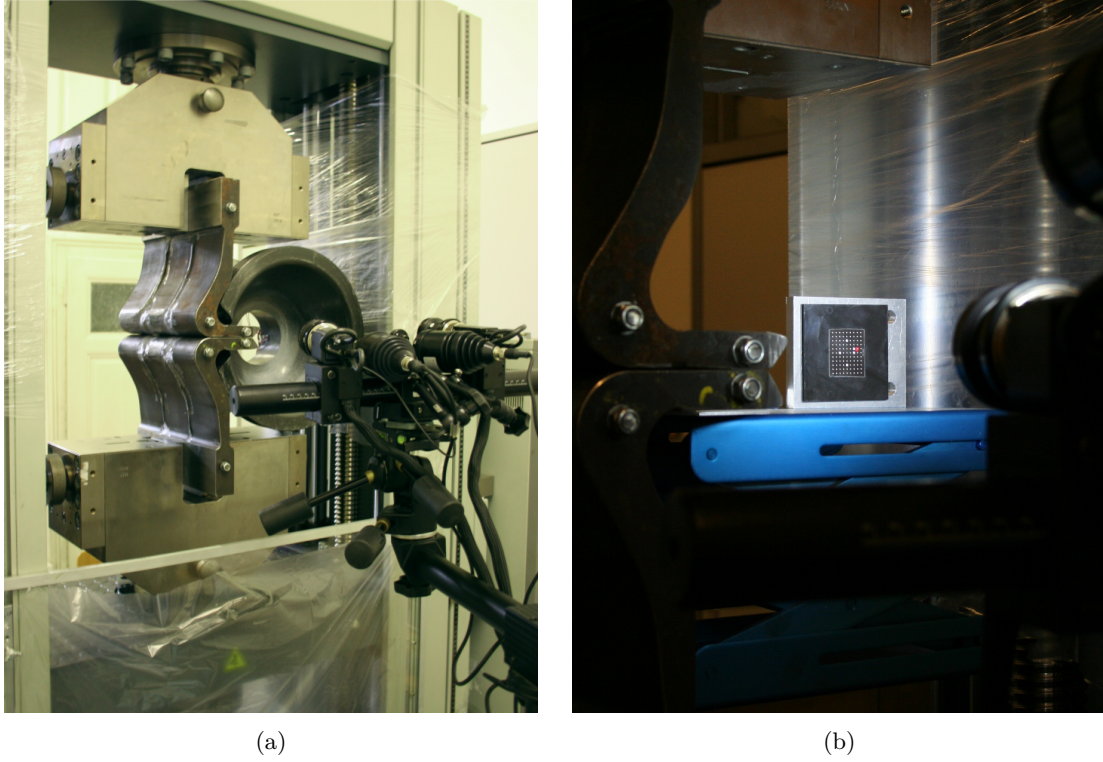
<div align="center">(a)   (b)</div>

Figure 4.10: GOM ARAMIS measurement setup: (a) synchronized stereo cameras facing one specimen failure surface; (b) 3D calibration of the camera image.

4.5.1 Maximum Load and Strain Measurement

The result of the load measurement is depicted in Fig. 4.11. As can be seen, the curve is nonlinear with respect to the crosshead travel of the machine at the first 20 %. This is caused by the non-perfect contact surface between the load transfer elements and the specimen. The system gets linear at an applied load of 10 kN.

The maximum load until failure occurs is about 45 kN. Figure 4.11 shows the measured signals of the strain gauges. The radial strain reaches a maximum of 15300 μm/m. The hoop and axial strain reaches a magnitude of 1300 μm/m and $-3700\,\mu$m/m, respectively. Then the radial failure occurs and splits the strain gauge, which is an indicator for a good failure point prediction. The optical strain measurement result for the expected failure point on the other specimen side can be seen in Fig. 4.12.

The absolute difference between the two measurement methods for radial and hoop strains is about 2000 μm/m and 700 μm/m. The optical measurement results of the observed area are depicted in Fig. 4.13. The images shown were taken directly before and directly after the critical load has been reached. This enables a perfect visualization of the crack that splits the rotor into two pieces. As can be seen, the crack occurs in the predicted area because of radial failure of the specimen.
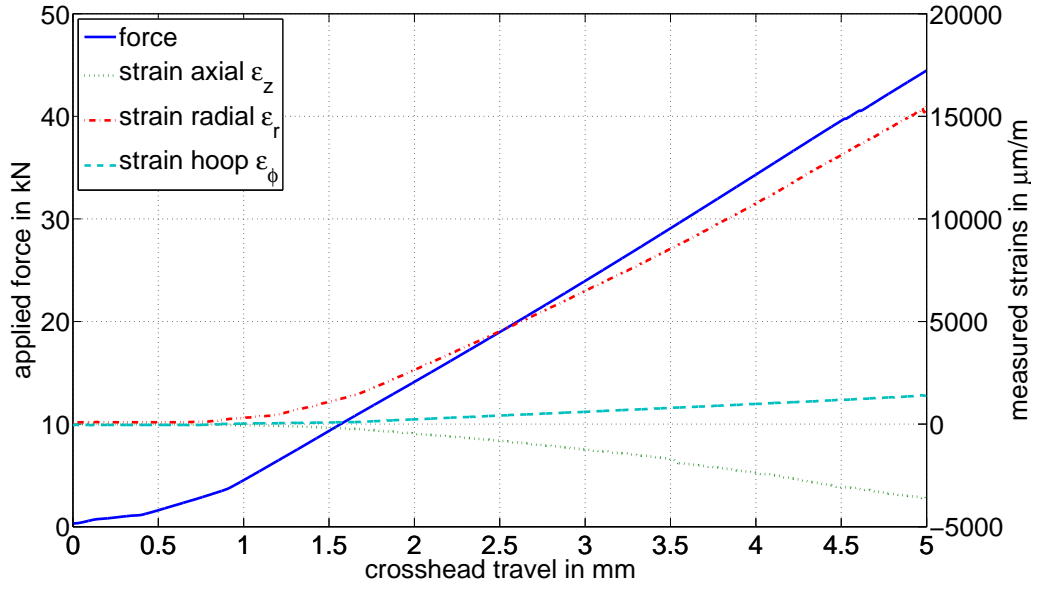
Figure 4.11: Flywheel static burst test experiment results: applied force to the load tranfer elements and strains in axial-, radial- and hoop direction as a function of the crosshead travel of the universal tensile testing machine.
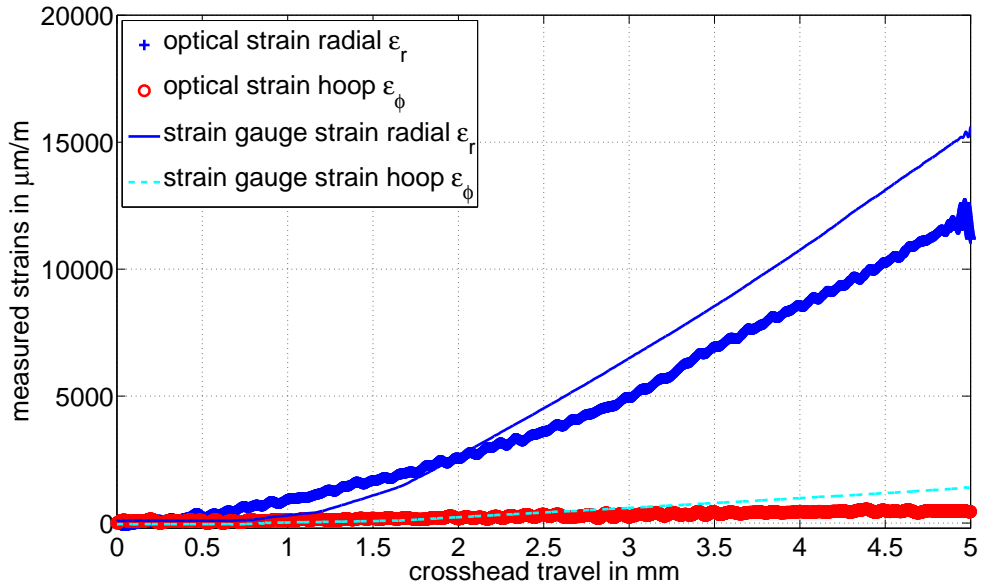

Figure 4.12: Optically and strain gauge measured strains in radial- and hoop direction as a function of the crosshead travel of the universal tensile testing machine.
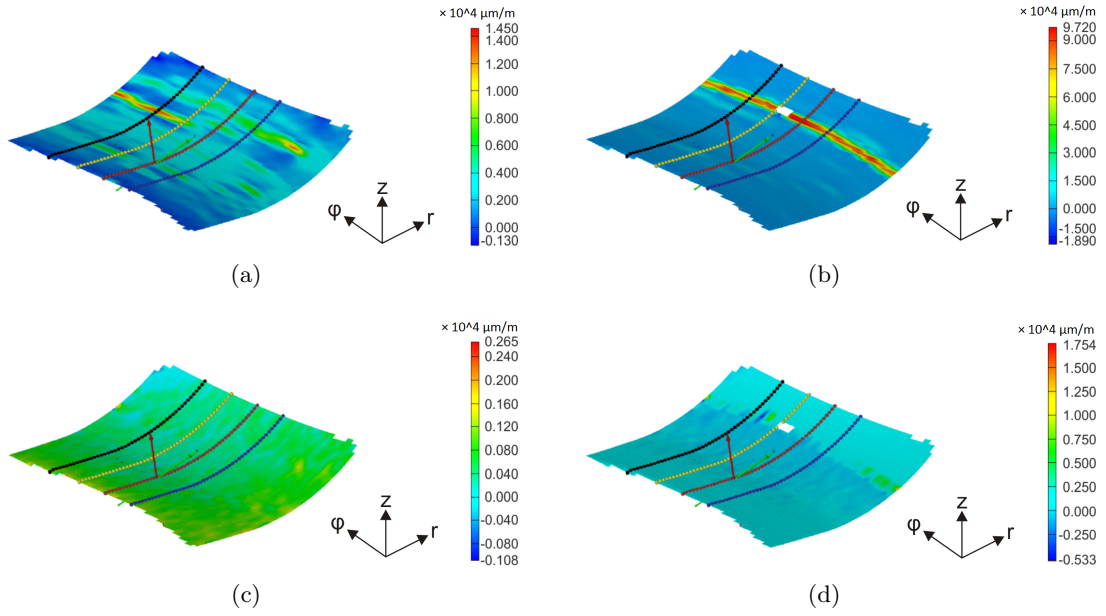
61

Figure 4.13: Optical strain measurement results: (a) radial direction, one time step before burst occurs; (b) radial direction, after failure at $F = 45\,\text{kN}$; (c) hoop direction, one time step before burst occurs; (d) hoop direction, after failure at $F = 45\,\text{kN}$.

4.5.2 Burst Fragment Analysis

The possibility of stopping the universal tensile testing machine directly after the burst event makes it possible to analyze the burst fragment. In this case, the burst fragment is the whole test specimen. At first, the crack on the surface is visualized to see its path running through the specimen. Therefore, a special fluid and developer combination is used to color the crack path in red, see Fig. 4.14(b).

Afterwards, a slice of $10\,\text{mm}$ thickness was cut out of the failure region of the test specimen. This was done with a band saw machine using a very slow feedrate to avoid any unwanted manipulation of the crack region, see Fig. 4.14(a). The resulting specimen (Fig. 4.14(c)) was then trimmed and polished with changing granulation size of the abrasive paper to clear the surface from tracks of the saw blade.

The first observation of the failure surface starts with following the crack from the start to the end. This was performed by a stereo microscope with a magnification of $50\times$, see Fig. 4.14(d). The specimen showed two cracks running from the left and right inner contour, both starting from the predicted failure point. The observation plan, as well as the crack images are depicted in Fig. 4.15.

Due to the fact that the carbon fiber/matrix interaction has a strong effect on the strength of the fiber reinforced materials, scanning electron microscope (SEM) observations of the interphase regions were done. Therefore, the specimen is further trimmed to
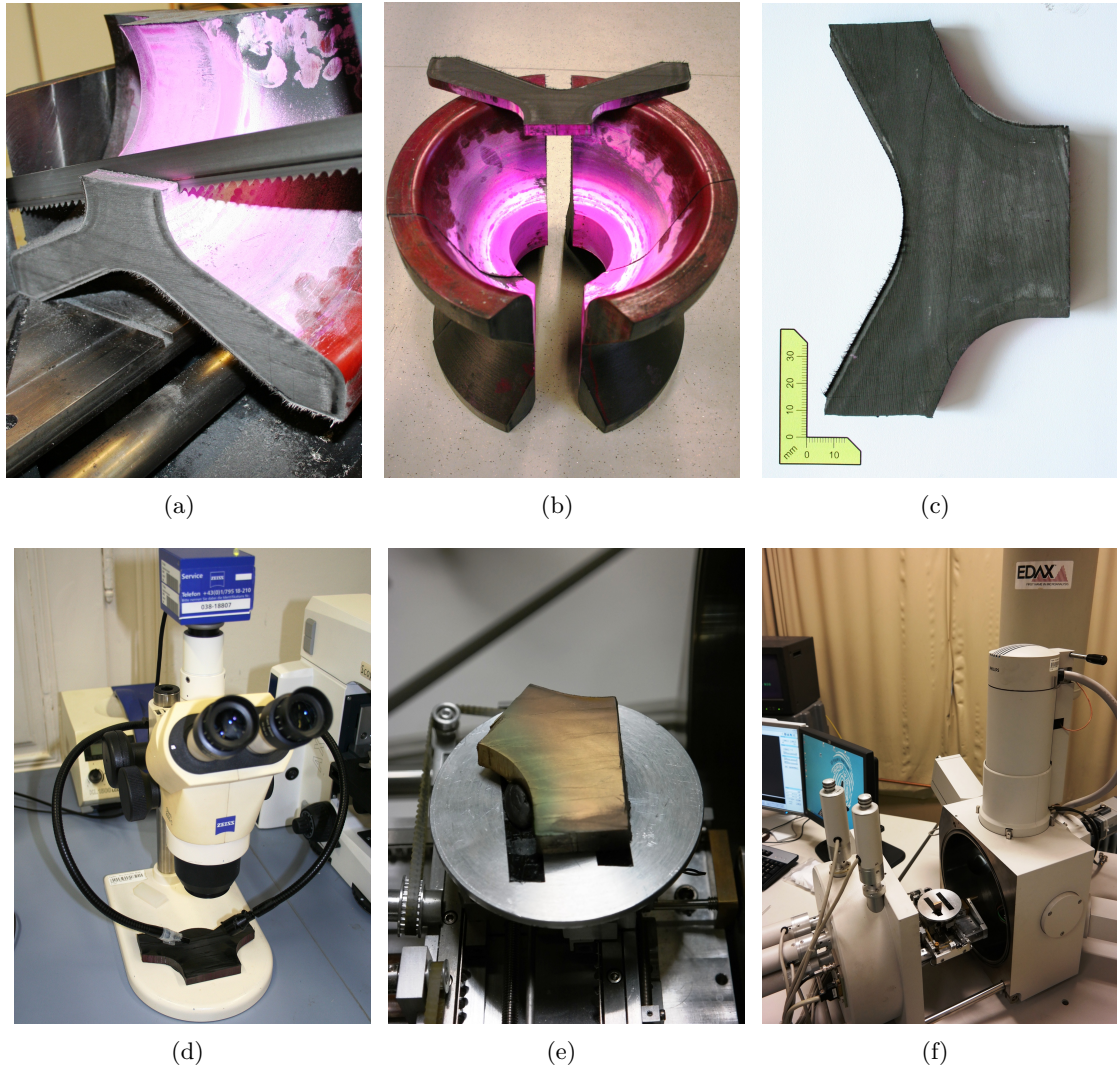
Figure 4.14: Observation of the failure surface: (a) cutting out the specimen with a band saw machine; (b) slice of 10 mm thickness in the predicted failure plane; (c) finished polished specimen for light microscope; (d) stereo microscope Zeiss Stemi 2000-C (magnification range: 10× to 50×); (e) finished gilded specimen for electron microscope; (f) SEM FEI Philips XL 30 (magnification range: infinitely variable up to 1000000×).

fit inside the SEM, see Fig. 4.14(f). Furthermore, the specimen was gilded to make the surface electrically conductive for use in the SEM, see Fig. 4.14(e). The interphase regions near the crack on the right side is depicted in Fig. 4.16 with different magnifications starting from 100× up to 4000×.
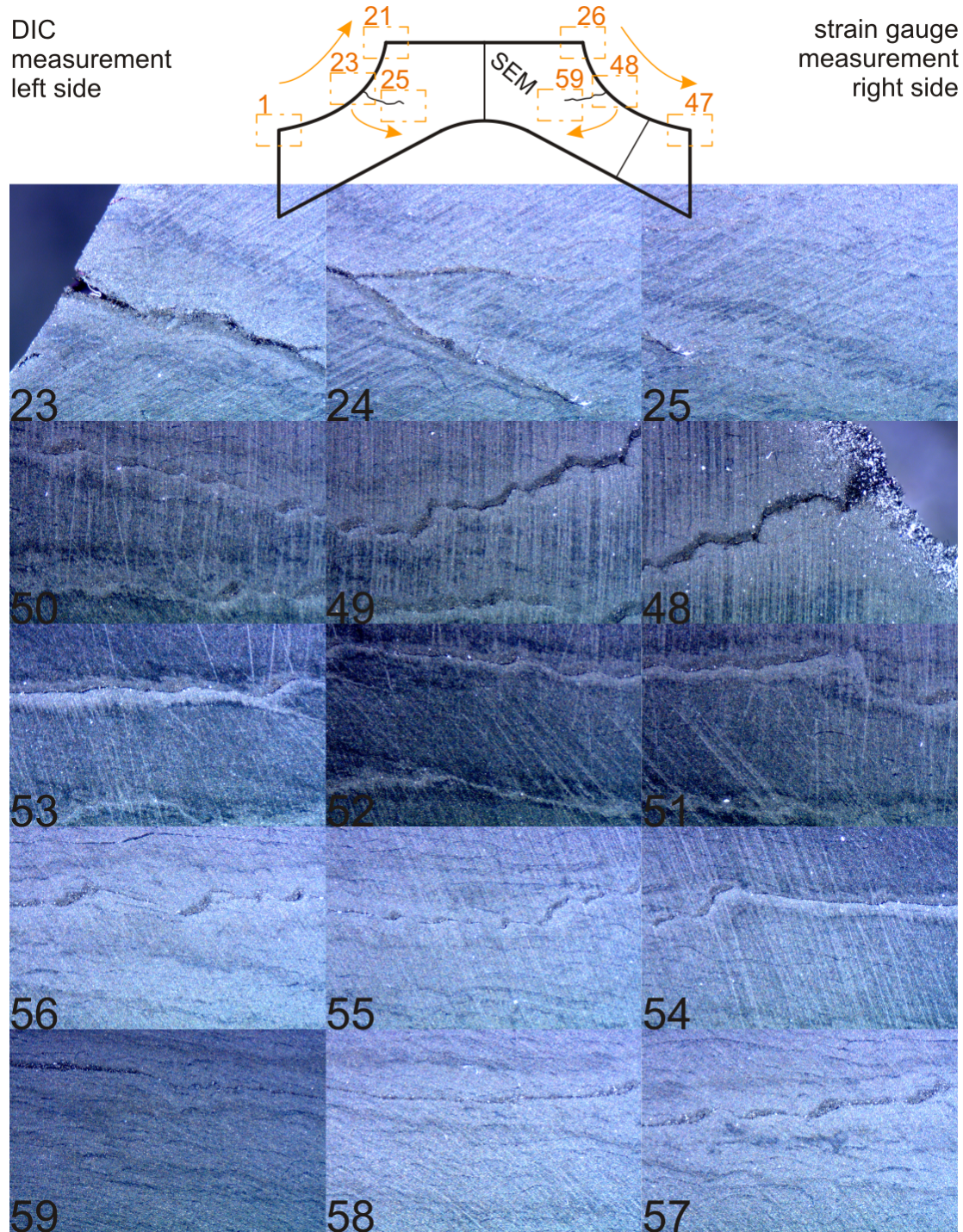
Figure 4.15: Stereo microscope results of the failure surface (magnification range: 50×) following the left (23 → 25) and right (48 → 57) crack starting from the inner contour.
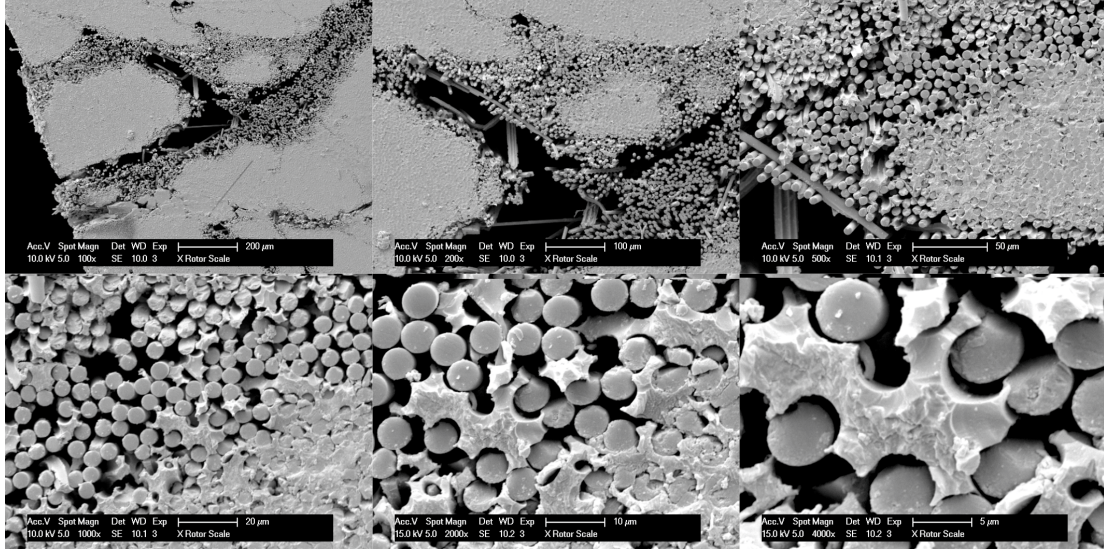
Figure 4.16: SEM results of the failure surface (magnification range: 100× to 4000×).

4.5.3 Analysis of Results

The simulation was performed neglecting the contact between the load transfer elements and the scaled CFRP inertia mass. This does not affect the result in the failure point but the observed elastic deformation of the load transfer elements during the experiment showed a major difference compared to the simulation. The simulation showed no movement of the whole assembly transverse to the pulling direction that is caused by a stick-slip effect in the contact area and the low stiffness of the clamping unit compared to perfect boundary conditions in the simulation. In fact, the simulation result shows a lower maximum load of $F = 43\,\text{kN}$ that is in very good coincidence with the FSBT test procedure, where the rotor cracked at $F = 45\,\text{kN}$. Furthermore, the failure point of simulation and experimental result show very good agreement.

The images taken by the stereo microscope show that both cracks run inside the wound layers due to lower strength than in pure epoxy matrix. Another visible result is the low void content which is a result of the pretension force during winding operation.

The SEM results make it possible to further understand the failure. The crack runs almost everywhere between the fiber and the matrix. This is an indicator for a rather weak resin fiber bond, resulting in interface cracks. For these structures possible uncertainties like residual stresses [91] or imperfections on the surface [92] due to the manufacturing process can be the reason. This causes a major decrease in radial direction strength and should be considered when choosing the fiber/matrix combination. The difference between weak and strong interfacial behavior was studied in [93, 94, 95].

5 Application: FESS - Flywheel Energy Storage System

5.1 Introduction

Within this chapter the achieved results of the previous ones are combined and applied to a FESS. The main focus lies on the completely new design of the FESS rotor that consists of a CFRP hollow shaft with sections of different winding angles and a hoop wound hybrid multi-ring, press-fitted inertia mass with a H-shaped cross-section where parts of it are presented in [96, 75, 97, 98].

The key design features of the FESS are the high energy efficiency and reliability. In the following the main components are shown and quickly explained which are the result of a major optimization procedure that covered hundreds of parameters that are detailed described in [99, 100, 101, 87, 102, 86].

5.2 FESS Prototype

The developed FESS prototype is designed for household applications where several charging and discharging cycles and storing periods of about one day can occur. The prototype and the electronic rack are shown in Fig. 5.1(a).

The in-runner FESS concept is covered inside an evacuated containment that is also used as supporting structure for the upper and lower stator where the axial and radial AMB's, M/G, auxiliary bearings and the position sensors are located. The FESS components are depicted in Fig. 5.1(b).

5.2.1 Electronic Rack

In Fig. 5.2(a) the front view of the electronic rack is shown. At the top the power supply for the sensors, control electronic and the data acquisition (DAQ) system is located. Underneath, the inverters for the AMB's (four, including two H-bridges each), the M/G (six H-bridges for the six coils of three phases A,B and C) and the used load for discharging (three 400 W lights on top of the electronic rack) are mounted.

Inverter The inverters for the AMB's are designed for minimum losses at a maximum continuous output current of 12 A, whereas the inverter for the M/G can provide 30 A continuous at a linked voltage of the DC bus of 350 V. Below the inverters, the three power supplies for the linked voltages are located. The upper two are for the AMB
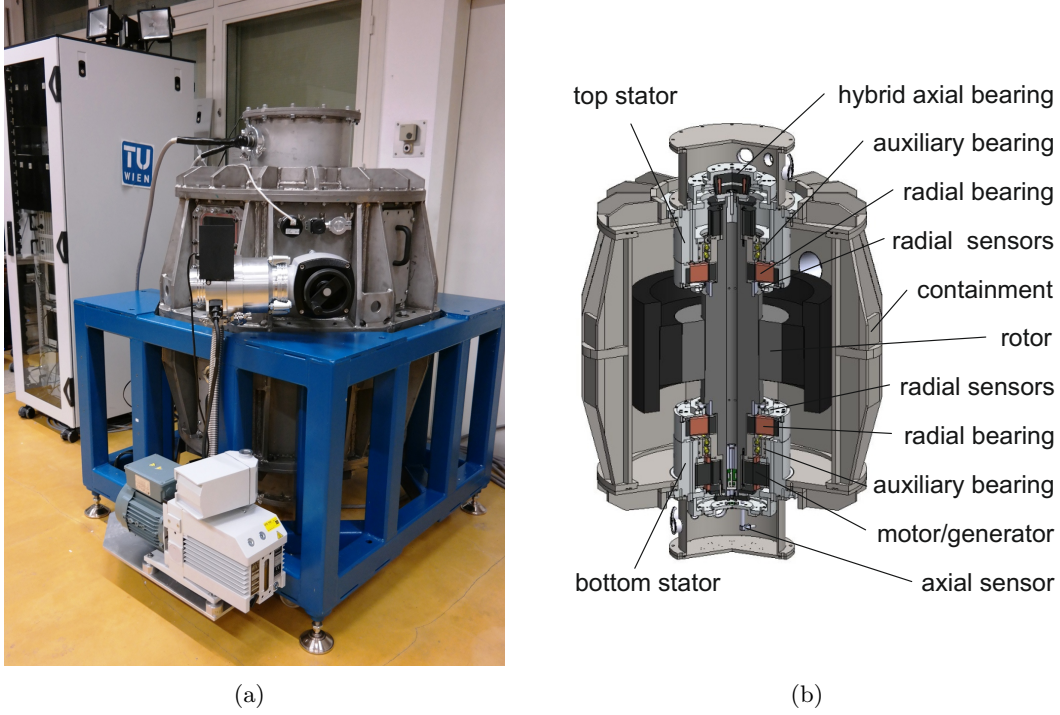
Figure 5.1: Flywheel energy storage system (FESS): (a) prototype consisting of the electronic rack and the containment including the flywheel; (b) cut view of the FESS.

inverters and the lower one is for the M/G inverters to be able to use different linked voltages for testing and to avoid total failure in case of total power loss.

Control electronic The rear view of the electronic rack is depicted in Fig. 5.2(b). From the left to the right one can see the power and sensor wires, the mainboard including the five controllers (axial AMB, radial AMB, M/G phase A,B and C), several filters for the sensor signals (positions, currents, voltages and temperatures) and the multichannel DAQ system.

Data acquisition The DAQ was realized by using two National Instruments cRIO systems in master/slave configuration programmed in LabVIEW. In total 120 channels are recorded at $62.5 \, \text{kS/ch}$ and handled by the integrated FPGA and realtime module before the data is streamed galvanically isolated to the PC where the signals are visualized and saved. The schematic is shown in Fig. 5.2(c).

The front panel (LabVIEW VI, see Fig. 5.2(d)) is designed for condition monitoring of the following FESS groups: axial AMB (z-position, current and voltage), radial AMB's (x_1, y_1-position, x_2, y_2-position, currents and voltage), M/G (absolute angle position, incremental angle pulse, currents and voltage) and system states (logic and temperatures).
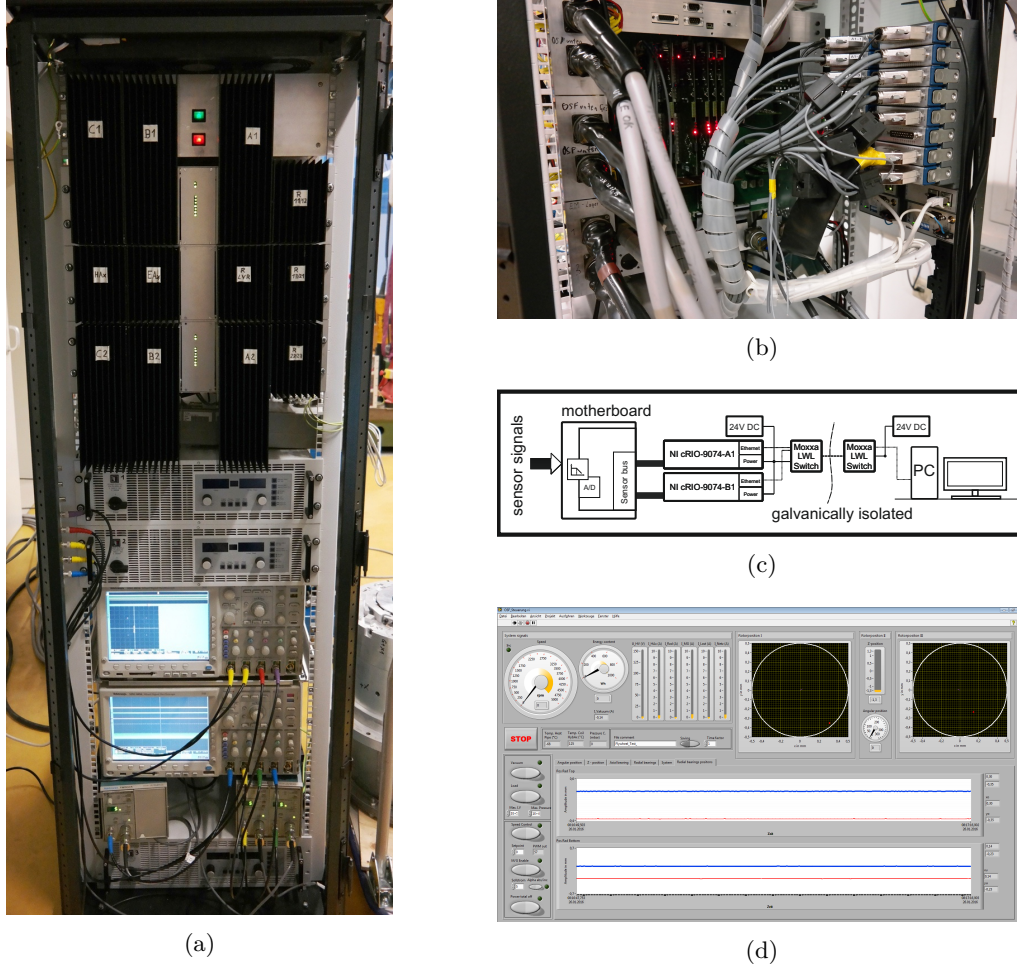
Figure 5.2: Electronic rack: (a) front view; (b) rear view showing the DAQ system, the ARM controller cards and the mainboard; (c) schematic of the DAQ system; (d) front panel of the LabView VI for condition monitoring.

5.2.2 Containment

High rotational speeds cause high kinetic energy and so fragments of the rotor can do serious damage to structures and people in case of a burst event. The heavy and very stiff designed steel construction is necessary in first to ensure a safe operation of the FESS and in second to evacuate the chamber to reduce rotational losses due to air drag. The containment and the support structure including the vacuum system is shown in Fig. 5.1(a).

Inside the containment there is the top and bottom stator mounted. The top stator consists of the axial and top radial AMB and the top auxiliary bearing, whereas the lower stator consists of the bottom radial AMB, the M/G and the bottom auxiliary bearing. In each stator, four radial position sensors are placed in differential mode and the angular
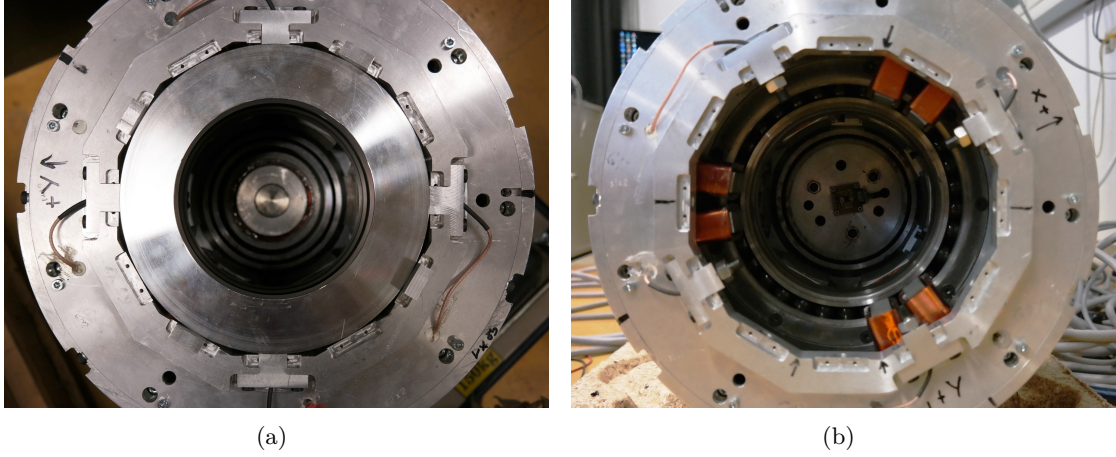
Figure 5.3: Stators of the FESS: (a) top stator with the calibration ring for the position
sensors; (b) bottom stator.

position sensors as well as the axial position sensor are integrated in the bottom stator.
The two finished assembled stators are shown in Fig. 5.3(a) and Fig. 5.3(b).

Active Magnetic Bearings The most important part of high efficient FESS are the
AMB's due to lower losses compared to conventional roller bearings and for the possibility
to vary the stiffness and damping of the bearings by adapting the control parameters.

The radial AMB's are separated into two planes with three magnets each in $120\,°$
configuration. The axial bearing is designed in a hybrid configuration consisting of an
AMB in combination with a permanent magnet to further reduce the power needed for
static levitation.

Switched Reluctance Motor The major advantage of a switched reluctance motor
(SRM) for FESS applications is the minimal holding torque in stand-by operation, one of
the most criticized facts in this topic. The M/G used is a 6/4-SRM with no permanent
magnets in the rotor part. The SRM serves also the possibility for compensation of
unbalance forces by separate control of the coils-current of one phase.

Rotor The main focus of the FESS lays on the rotor due to its high speed rotating
inertia mass that stores the kinetic energy. The aim of rotor design is to maximize the
energy density κ which is defined as the rotational kinetic energy per unit mass m

$$\kappa = \frac{1}{2}\frac{J\omega_{\max}^2}{m} \ , \tag{5.1}$$

with the maximum angular velocity $\omega_{\max}$ and the polar moment of inertia J of the rotor.
The design purpose is also strict to the following considerations:

- especially for filament wound CFRP or other fiber reinforced materials it is necessary to measure the material parameter from specimens that are manufactured in the same way as the rotor is done,

- using a strength safety factor for all failure criteria, to ensure some clearance for manufacturing imperfections or modeling uncertainties,

- if it's possible, one should manufacture press-fitted multi-ring assemblies for the inertia mass due to the advantages of pre-stressed structures,

- the dynamics of the rotor has to be taken into account, due to the fact, that flywheel application use large moments of inertia and so a fast drive through natural frequencies of the rotor is problematic because of resonances and existing unbalances.

In the following section, a design of a FESS rotor is presented that uses the above mentioned considerations.

5.3 Design and Optimization of a CFRP Flywheel Rotor

The starting point for the investigation on a new FESS rotor is a configuration with an aluminium shaft that is thermally shrink-fitted into a CFRP hoop wound inertia mass with a special patented geometry ([103, 86]). The shape of this CFRP inertia mass is a result of a two-step energy density optimization. In the first step a genetic algorithm is used to find the optimum shape of the inertia mass. Based on these results characteristic parameters are derived and a combined strength safety factor and rotordynamic optimization is carried out in the second step.

The stress state of this FESS rotor (aluminium shaft & inertia mass) is a linear combination of the thermal press-fitting process and the inertial load due to rotation. With a strength safety margin of two, an energy density of 5.5 Wh/kg at a rotor speed of $\omega_{\mathrm{sp}} = 860\,\mathrm{s}^{-1}$ can be reached with this setup, compared to 3.8 Wh/kg for a conventional H-shaped rotor geometry at a rotor speed of $\omega_{\mathrm{sp}} = 750\,\mathrm{s}^{-1}$.

This values are in fact theoretically, because the manufacturing by wet filament winding is rather complicated and uneconomical. The biggest problem is given by the exothermic reaction of the epoxy resin during the hardening process. This implies thermally induced pre-stressing that has a negative influence on the applicable load by tension stress.

The thermal pre-stresses are reduced by manufacturing rings with lower thicknesses in radial direction that are press-fitted together. The feasibility study for a press-fitted multi-ring assembly with rectangular cross-section was shown in [97]. Furthermore, the energy density of a FESS rotor can be increased by using a CFRP hollow shaft instead of a full aluminium shaft ([98]).

The new design of the FESS rotor consists of a CFRP hollow shaft and a press-fitted hybrid multi-ring H-shaped inertia mass. The whole design had to be integrated into the existing FESS test rig and therefore the following boundary conditions are present:

- the outer geometry of the shaft is given to use the existing AMB and M/G parts,

- the inner geometry of the containment is the limit for the size of the inertia mass,

- a minimum core diameter of the hollow shaft due to a minimum mandrel diameter for filament winding,

- a maximum of three rings for the inertia mass because of the high manufacturing effort and

- the overall mass of the FESS rotor is restricted.

This hollow shaft design further increases the energy density and the pre-stressing of the inertia mass reduces the radial stress component of the stress state compared to a full inertia mass and so higher operational speeds can be achieved for this CFRP material with a low radial strength.

Material Modeling   The aluminium, steel and ferro-magnetic sections are assumed to have isotropic mechanical behaviour. The hollow shaft is separated into three cylinders with different but constant positive and negative winding angle α_i. The rings for the inertia mass are hoop wound ($\alpha = 0\,^\circ$).

Hence, the cylinders can be obtained by several plies of embedded fibers and so each ply has an orthotropic mechanical behavior, as shown in Fig. 5.4(a) and Fig. 5.4(b). The generalized Hooke's law is used to model the orthotropic material behavior in the local ply l, q, t-frame with $\boldsymbol{E}_L$, the local material stiffness tensor. It's components are computed by the given relations

$$\Delta = \frac{1 - 2\nu_{12}\nu_{21} - 2\nu_{21}\nu_{23}\nu_{12} - \nu_{23}^2}{E_1 E_2^2}, \tag{5.2}$$

$$
\begin{aligned}
G_{qt} &= \frac{E_2}{2(1 + \nu_{23})}, \quad \frac{\nu_{ij}}{E_i} = \frac{\nu_{ji}}{E_j}, \quad i, j = 1, 2, 3 \ , \\
E_{ll} &= \frac{1 - \nu_{23}^2}{E_2^2 \Delta}, \qquad E_{lq} = \frac{\nu_{21} + \nu_{21}\nu_{23}}{E_2^2 \Delta}, \\
E_{qq} &= \frac{1 - \nu_{12}\nu_{21}}{E_1 E_2 \Delta}, \quad E_{qt} = \frac{\nu_{23} + \nu_{12}\nu_{21}}{E_1 E_2 \Delta}, \\
E_{tt} &= \frac{1 - \nu_{12}\nu_{21}}{E_1 E_2 \Delta}, \quad E_{lt} = \frac{\nu_{21} + \nu_{21}\nu_{23}}{E_2^2 \Delta}.
\end{aligned}
\tag{5.3}
$$

The overall mechanical behavior in the global frame (φ, r, z) is calculated by assuming that the use of the classical lamination theory (CLT) is valid for the three sections with high thickness to radius ratio and where only the membrane forces $\boldsymbol{n}_G$, the extensional stiffness tensor $\boldsymbol{A}$ and the strains $\boldsymbol{\varepsilon}_G$ are taken into account. The bending moments $\boldsymbol{m}_G$ and the bending stiffness tensor $\boldsymbol{D}$ are neglected.
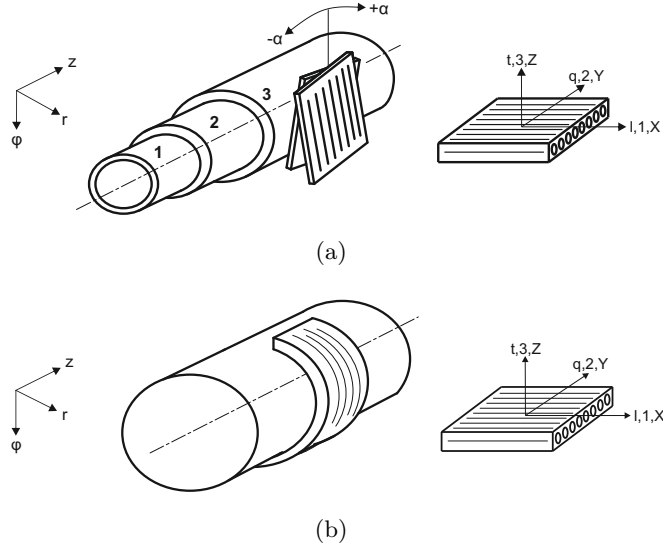
(a)

(b)

Figure 5.4: Composite cylinder sections in the global φ, r, z-coordinate system, and plan of ply in the local l, q, t-coordinate system: (a) three sections of different winding angles; (b) hoop wound cylinder.

Further, the assumption of a symmetric laminate with equal ply thicknesses h leads to a zero coupling stiffness tensor $\boldsymbol{B}$ and therefore also the curvature $\boldsymbol{\kappa}_G$ must not be taken into account. The overall global stiffness tensor $\boldsymbol{E}_G$ can be described by transformation of the local stiffness tensor $\boldsymbol{E}_L$ of each ply into the global coordinate system. Due to the positive and negative winding angle and the assumption of an even number of plies n in each section, the global stiffness tensor $\boldsymbol{E}_G(\alpha)$ can be calculated as follows

$$
\boldsymbol{n}_G = \begin{bmatrix} n_\varphi \\ n_r \\ n_z \\ n_{rz} \\ n_{\varphi z} \\ n_{\varphi r} \end{bmatrix} = \sum_{k=1}^{n} \int_{r_{k-1}}^{r_k} \begin{bmatrix} \sigma_\varphi \\ \sigma_r \\ \sigma_z \\ \sigma_{rz} \\ \sigma_{\varphi z} \\ \sigma_{\varphi r} \end{bmatrix}_k dr = \sum_{k=1}^{n} \int_{r_{k-1}}^{r_k} (\boldsymbol{E}_G)_k \begin{bmatrix} \varepsilon_\varphi \\ \varepsilon_r \\ \varepsilon_z \\ \gamma_{rz} \\ \gamma_{\varphi z} \\ \gamma_{\varphi r} \end{bmatrix}_k dr
$$

$$
= \sum_{k=1}^{n} \int_{r_{k-1}}^{r_k} (\boldsymbol{T}^{-1} \boldsymbol{E}_L \, \boldsymbol{T}^{-T})_k \begin{bmatrix} \varepsilon_\varphi \\ \varepsilon_r \\ \varepsilon_z \\ \gamma_{rz} \\ \gamma_{\varphi z} \\ \gamma_{\varphi r} \end{bmatrix}_k dr = \sum_{k=1}^{n} \left[(\boldsymbol{T}^{-1} \boldsymbol{E}_L \, \boldsymbol{T}^{-T})_k \int_{r_{k-1}}^{r_k} dr \right] \underbrace{\begin{bmatrix} \varepsilon_\varphi \\ \varepsilon_r \\ \varepsilon_z \\ \gamma_{rz} \\ \gamma_{\varphi z} \\ \gamma_{\varphi r} \end{bmatrix}}_{\varepsilon_G} \quad (5.4)
$$

$$
= \sum_{k=1}^{n} \left[(\boldsymbol{T}^{-1} \boldsymbol{E}_L \, \boldsymbol{T}^{-T})_k (r_k - r_{k-1}) \right] \varepsilon_G = \boldsymbol{A} \cdot \varepsilon_G \; ,
$$

$$\boldsymbol{n}_G = \left[h \sum_{k=1}^{n} (\boldsymbol{T}^{-1} \boldsymbol{E}_L \, \boldsymbol{T}^{-T})_k \right] \boldsymbol{\varepsilon}_G$$

$$= h \left[\frac{n}{2} (\boldsymbol{T}(\alpha)^{-1} \boldsymbol{E}_L \, \boldsymbol{T}(\alpha)^{-T}) + \frac{n}{2} (\boldsymbol{T}(-\alpha)^{-1} \boldsymbol{E}_L \, \boldsymbol{T}(-\alpha)^{-T}) \right] \boldsymbol{\varepsilon}_G \;, \qquad (5.5)$$

$$\boldsymbol{\sigma}_G = \boldsymbol{n}_G / (n \cdot h) = \underbrace{\left[\frac{(\boldsymbol{T}(\alpha)^{-1} \boldsymbol{E}_L \, \boldsymbol{T}(\alpha)^{-T}) + (\boldsymbol{T}(-\alpha)^{-1} \boldsymbol{E}_L \, \boldsymbol{T}(-\alpha)^{-T})}{2} \right]}_{\boldsymbol{E}_G} \boldsymbol{\varepsilon}_G \;, \qquad (5.6)$$

$$\boldsymbol{\sigma}_G = \boldsymbol{E}_G(\alpha) \cdot \boldsymbol{\varepsilon}_G \;, \qquad (5.7)$$

$$\boldsymbol{E}_G(\alpha) = \frac{(\boldsymbol{T}(\alpha)^{-1} \boldsymbol{E}_L \, \boldsymbol{T}(\alpha)^{-T}) + (\boldsymbol{T}(-\alpha)^{-1} \boldsymbol{E}_L \, \boldsymbol{T}(-\alpha)^{-T})}{2} \;. \qquad (5.8)$$

Thereby, the transformation matrix $\boldsymbol{T}$ with $c = \cos\alpha$ and $s = \sin\alpha$ computes by

$$\boldsymbol{T}(\alpha) = \begin{bmatrix} c^2 & 0 & s^2 & 0 & 2cs & 0 \\ 0 & 1 & 0 & 0 & 0 & 0 \\ s^2 & 0 & c^2 & 0 & -2cs & 0 \\ 0 & 0 & 0 & c & 0 & s \\ -cs & 0 & cs & 0 & c^2 - s^2 & 0 \\ 0 & 0 & 0 & -s & 0 & c \end{bmatrix} \;. \qquad (5.9)$$

Stress Analysis For stress analysis the rotor model was built up in the FE software COMSOL [68] performing a quasi-static analysis with press-fit between the inertia mass and the hollow shaft and press-fits between the three rings of the inertia mass. The axisymmetric geometry of the nonlinear (contact between rings and shaft) model of the rotor is discretized by quadrilateral finite elements with quadratic basis functions and using the $r\varphi$- symmetry plane as roller boundary condition, see Fig. 5.5. Each section of the CFRP hollow shaft is modeled by using Eqn. (5.8). The CFRP rings of the inertia mass are assumed to be transversely isotropic in hoop direction. For the CFRP rotor and the shaft components the material parameters are listed in Table 5.1. The stress state of this FESS rotor was calculated in two steps. In a first step the stress state due to all existing interference-fits and in a second step the inertial loads due to rotation was computed. The global stress state was transformed back into the local frame to perform the failure estimation by the generalized quadratic Tsai-Wu criterion, which reads as (see also section 4.3)

$$\overline{\boldsymbol{F}}^T \boldsymbol{\sigma}_L + \boldsymbol{\sigma}_L^T \widetilde{\boldsymbol{F}} \boldsymbol{\sigma}_L = 1 \;. \qquad (5.10)$$

The stress state vector $\boldsymbol{\sigma}_L$ and $\overline{\boldsymbol{F}}$, $\widetilde{\boldsymbol{F}}$ the second and fourth order tensor of the strength parameters out of Table 5.1 and Table 5.2 are used to calculate a scalar strength safety
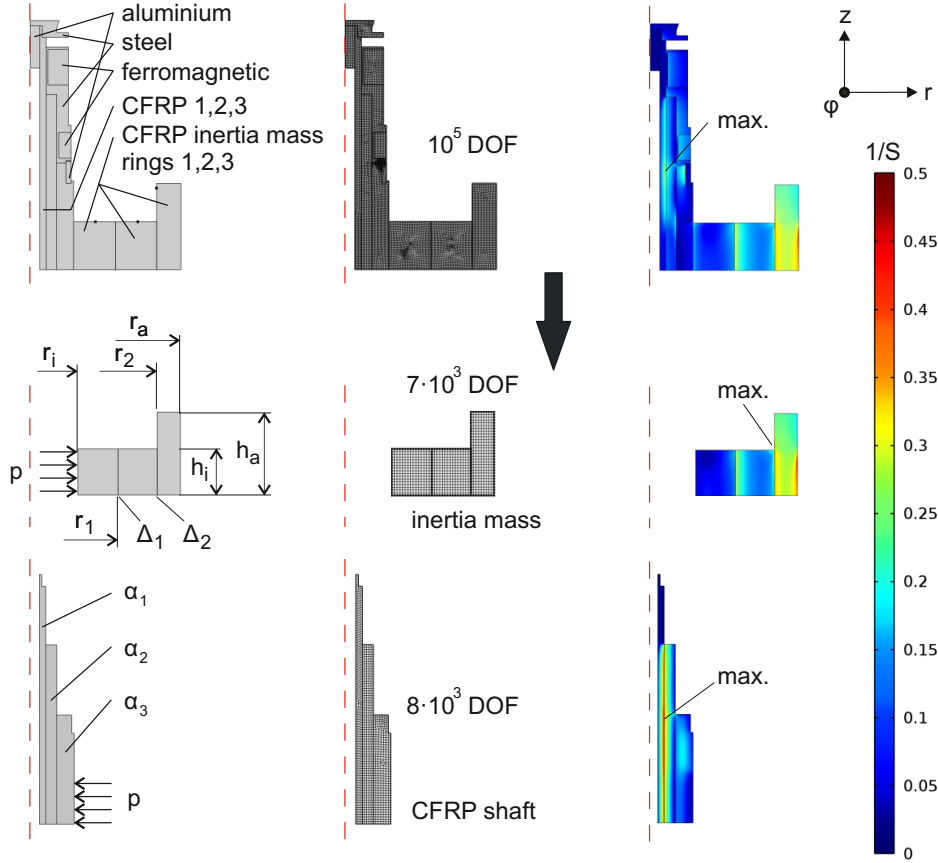
Figure 5.5: Stress analysis, defined regions and model simplification by separating the rotor into inertia mass and shaft including a link modeled with a pressure p to reduce simulation effort for the two optimizations.

parameter S. A safety parameter $1/S \geq 1$ indicates material failure and for the following optimization the strength safety factor $S_{R_{TW}}$ is used to avoid material failure.

Modal Analysis   For modal analysis of the FESS rotor the FE software ANSYS [69] was used with pre-stressing of the rotating structure using the following reduced semi-discrete Galerkin formulation for structural mechanics in the stationary frame

$$\boldsymbol{M}_u \cdot \underline{\ddot{u}} + (\boldsymbol{G}_u + \boldsymbol{C}_u) \cdot \underline{\dot{u}} + \boldsymbol{K}_u \cdot \underline{u} = \boldsymbol{f}_B \; , \tag{5.11}$$

where $\boldsymbol{M}_u$, $\boldsymbol{G}_u$, $\boldsymbol{C}_u$, $\boldsymbol{K}_u$ and $\boldsymbol{f}_B$ denotes the mass, gyroscopic, damping and stiffness matrix, and $\boldsymbol{f}_B$ is the bearing force vector. The rotordynamic model consists of different computational regions representing the components of the rotor, see Fig. 5.6. Each region is meshed using SOLID273 generalized axisymmetric solid 8 node element to perform a full 3D analysis with minimal simulation effort. Each section of the CFRP hollow shaft
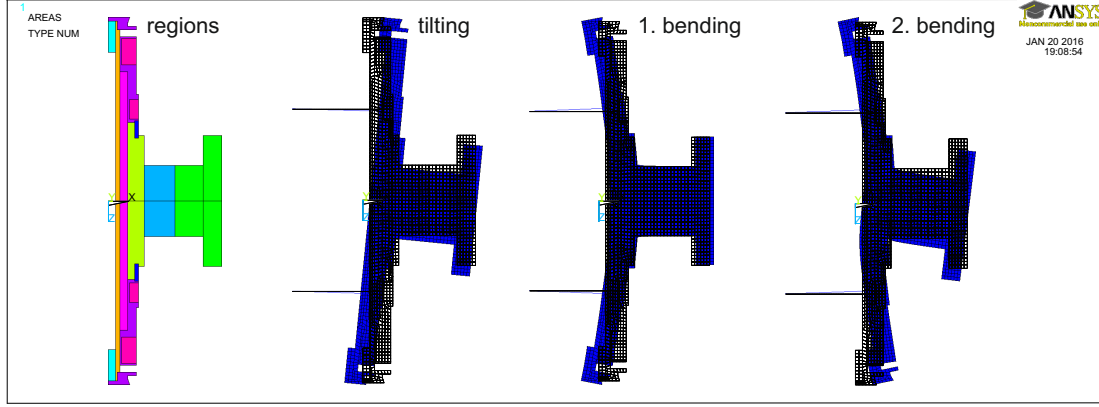
Figure 5.6: Rotordynamic analysis, defined areas and resulting sample mode shapes: tilting, first bending and second bending mode.

is modeled by using Eqn. (5.8). The CFRP rings of the inertia mass are assumed to be transversely isotropic in hoop direction. The whole configuration is pre-stressed, firstly due to the initial configuration and secondly by the stress stiffening effect due to rotation. The material parameters in Table 5.1 are used for all simulations. The characteristic of the magnetic bearing was simplified using the COMBIN214 2D element at the location of the radial bearings. These elements allow stiffness and damping characteristics in two perpendicular directions defining the bearing plane. The bearing stiffness and damping were set to 10^6 N/m and $2 \cdot 10^4$ Ns/m. Based on the maximum stored energy and the given rotor geometry of the inertia mass, the maximum speed of rotation was used to set up the Campbell diagram. In total, five incremental steps were used to calculate the Campbell diagram to find the critical speed of the FESS that operates below the lowest bending natural frequency, so called under-critical.

Optimization of the FESS Rotor   At first the geometry and the material combination for the rings of the inertia mass is optimized and afterwards the winding angles of the CFRP hollow shaft are optimized. This separation is valid due to the fact, that the optimization of the inertia mass is to maximize the energy density which is slightly effected by the shaft due to the small radii and vice versa the bending natural frequency maximization of the shaft is not effected by the inertia mass because firstly the overall mass is restricted and secondly for all possible materials, used for the different rings, the stiffness in axial direction is nearly the same which influences mostly the bending natural frequencies.

The optimization variables for the inertia mass are the following parameter: inner height h_i, radius r_1, r_2 and r_a and the interferences Δ_1 and Δ_2, see Fig. 5.5. The interferences are bounded by a maximum of 0.4 mm, the thickness of one ring is restricted to a minimum of 30 mm, the radius r_a can reach a maximum of 330 mm, the height h_i is able to reach $h_a = 200$ mm and the desired mass m_{des} should count 125 ± 5 kg. The problem was solved using a genetic algorithm. The fitness function is to maximize

the energy density κ

$$\min_{\boldsymbol{x}} \left\{ -\kappa \right\} = \min_{\boldsymbol{x}} \left\{ -\frac{1}{2} \frac{J\omega_{\max}^2}{m} \right\} , \tag{5.12}$$

Table 5.1: Measured material data for the T800S CFRP specimens with a fiber volume fraction of 60 % and additional material data used for simulation.

T800S/705		
Elastic modulus in direction l, GPa	E_1^*	139
Elastic modulus in direction q, GPa	E_2^*	7.8
Elastic modulus in direction t, GPa	E_3^*	7.8
Poissons ratio	ν_{12}^*	0.41
Poissons ratio	ν_{23}^*	0.38
Shear modulus in direction lq, GPa	G_{12}^*	3.4
Tensile strength in direction l, MPa	X_t^*	2200
Compressive strength in direction l, MPa	X_c^*	1000
Tensile strength in direction q, t, MPa	Y_t^*, Z_t^*	24
Compressive strength in direction q, t, MPa	Y_c^*, Z_c^*	113
Shear strength in direction lq, MPa	S_{12}^*	57
Shear strength in direction lt, MPa	S_{13}^*	57
Shear strength in direction qt, MPa	S_{23}^*	14
Density, kg/m^3	ρ^*	1617
Steel		
Elastic modulus, GPa	E_{St}	210
Poissons ratio	ν_{St}	0.3
Von mises strength, MPa	$\sigma_{V,St}$	690
Density, kg/m^3	ρ	7850
Aluminium		
Elastic modulus, GPa	E_{Al}	70
Poissons ratio	ν_{Al}	0.3
Von Mises strength, MPa	$\sigma_{V,Al}$	500
Density, kg/m^3	ρ	2700
Ferro-magnetic		
Elastic modulus, GPa	E_{Fm}	210
Poissons ratio	ν_{Fm}	0.3
Von Mises strength, MPa	$\sigma_{V,Fm}$	600
Density, kg/m^3	ρ	8150

* obtained by measurements

where $\omega_{\max} = \omega_{\mathrm{sp}}\sqrt{1/(S_{R_{TW}}\max(1/S_1, 1/S_2, 1/S_3))}$ and is evaluated by a simplified quasi-static FE model of the inertia mass calculating the safety parameters $1/S_{1,2,3}$ of the three rings and using a strength safety factor against failure $S_{R_{TW}}$, shown in the mid of Fig. 5.5, where $\boldsymbol{x} = (h_i, r_1, r_2, r_a, \Delta_1, \Delta_2)^T$ is the vector of the optimization variables. The pressure at the inner radius is set to $p = 5\,\mathrm{MPa}$ and interference pressures at the interfaces give the nonlinear constraint function

$$\min_{\boldsymbol{x}}(p_{\Delta_1}, p_{\Delta_2}) \geq p_{\min} \ , \tag{5.13}$$

where $p_{\min} = 2\,\mathrm{MPa}$ at full speed to guarantee no opening of the interfaces due to manufacturing uncertainties. The optimization was done for different materials for each ring. A set of four materials that differs in the stiffness in hoop direction, strength and density were used and so 64 optimizations had to be carried out to find the optimum configuration.

The optimization variables for the shaft are the three winding angles of the three different sections: α_1, α_2 and α_3. The step size of a winding angle is set to $\Delta\alpha = 1°$, due to the manufacturing constraints given by the filament winding process. This leads to a genetic algorithm which can handle integer variables. The fitness function is to maximize the lowest natural bending frequencies f_{B1} and f_{B2}

$$\min_{\boldsymbol{x}} \left\{ -\min(f_{B1}, f_{B2}) \right\} \tag{5.14}$$

and is evaluated by the rotordynamic FE model of the FESS rotor, where $\boldsymbol{x} = (\alpha_1, \alpha_2, \alpha_3)^T$ is the vector of the optimization variables. Therefore, the Campbell diagram is evaluated up to an angular velocity $\omega_{\max}$ that is given by the result of the previous optimization and the measured material properties. A simplified quasi-static FE model, shown in the bottom of Fig. 5.5, of the rotor with the three different inverse safety parameters $1/S_{1,2,3}$ of each region gives the nonlinear constraint function

$$\max_{\boldsymbol{x}} \left(\frac{1}{S_1}, \frac{1}{S_2}, \frac{1}{S_3} \right) \leq \frac{1}{S_{R_{TW}}} \ , \tag{5.15}$$

where $S_{R_{TW}}$ denotes a strength safety factor against failure that is given by the input. The static model was simplified to reduce simulation effort by replacing the contact between the inertia mass and shaft with a constant pressure of $p = 5\,\mathrm{MPa}$. Another constraint is the maximum allowable winding angle of about $70°$ to guarantee a possible manufacturing of the hollow shaft due to the pretension force.

The fitness functions as well as the constraints for both optimizations are shown in Fig. 5.7 and the MATLAB ([77]) built-in function $ga(...)$ has been used. The population size was 200 and ten elite individuals were used. Any other options where left default.

The goal of the first optimization is to find the material combination and geometry parameter that maximizes the energy density of the hybrid multi-ring inertia mass for the given geometry boundaries, strength safety factor $S_{R_{TW}} = 2$ for stress analysis and the selectable materials for the rings that are listed in Table 5.2. The optimization resulted in
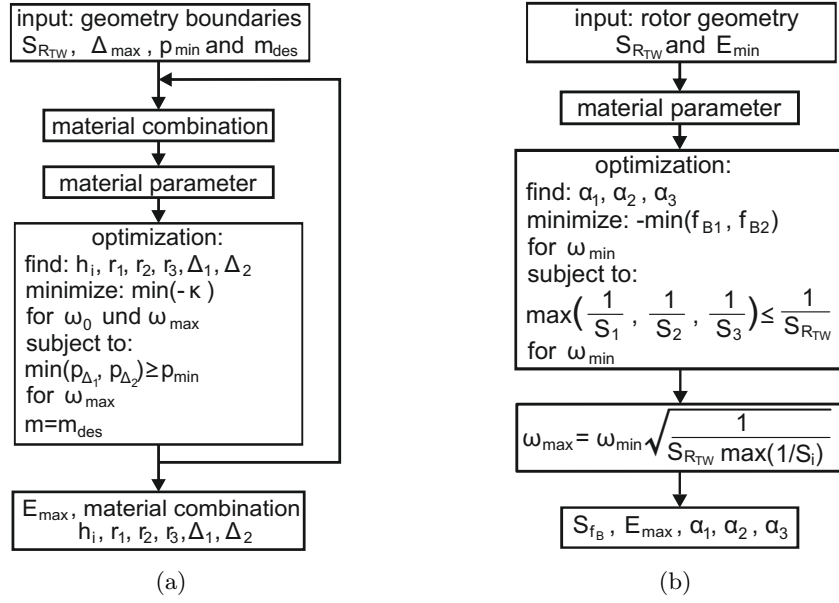
Figure 5.7: Optimization schemes: (a) hybrid multi-ring inertia mass; (b) CFRP hollow shaft.

a maximum energy density of $\kappa = 16.2\,\mathrm{Wh/kg}$ for an angular velocity $\omega_{\max} = 1390\,\mathrm{s}^{-1}$.

Finding the winding angle triple, which maximizes the minimum of the first and the second natural bending frequency for the given input of geometry, strength safety factor $S_{R_{TW}} = 2$ for stress analysis and the above given results is the goal of the second optimization. By fulfilling the nonlinear constraint function, a maximum angular velocity $\omega_{\max}$ can be calculated that leads to a maximum energy content $E_{\max}$. Using the Campbell diagram, a safety factor S_{fB} against reaching the lowest natural bending frequency, due to the optimal solution for the winding angles α_1, α_2 and α_3, can be found. After 45 generations, a winding angle optimum combination of $\alpha_1 = 19\,°$, $\alpha_2 = 69\,°$ and $\alpha_3 = 13\,°$ for an angular velocity $\omega = 1390\,\mathrm{s}^{-1}$ was found.

This leads to a lowest bending natural frequency of $284\,\mathrm{Hz}$ for the second S-shaped bending mode at this speed. The stress analysis at this speed results in a safety factor of $S_{R_{TW}} = 2.21$. Hence, the speed can still be increased to $\omega = 1460\,\mathrm{s}^{-1}$ until failure in the hollow shaft occurs and that leads to an energy density of $11.9\,\mathrm{Wh/kg}$ for the FESS rotor. Towards the energy density, this is an increase of $38\,\%$ compared to the aluminium shaft based FESS rotor with identical inertia mass. For this case the Campbell diagram has to be enlarged and it can be found that the critical speed is far beyond the failure speed. The safety factor against reaching the second backward bending mode is $S_{fB} = 1.21$, as can be seen in Fig. 5.8.
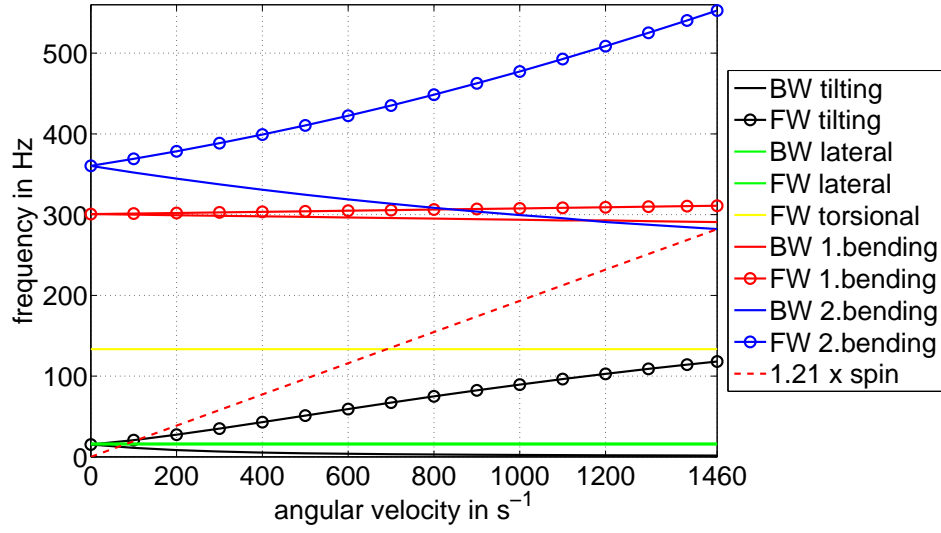
Figure 5.8: Campbell diagram of the FESS rotor: tilting mode (TM), first (1.BM) and second (2.BM) bending mode and critical speed.

Table 5.2: Selectable material data for optimization.

	1*	2*	3*	4
Fiber	T800S	K13916	K63916	S2-449 43.5k
Matrix	705 epoxy	705 epoxy	705 epoxy	SP 381
E_1, GPa	139	290	190	50
E_2, GPa	7.8	7.8	10.7	13.3
E_3, GPa	7.8	7.8	10.7	13.3
ν_{12}	0.41	0.4	0.4	0.4
ν_{23}	0.38	0.4	0.4	0.4
G_{12}, GPa	3.4	3.9	3.9	4.7
X_t, MPa	2200	1300	2400	1700
X_c, MPa	1000	470	1100	1160
Y_t, Z_t, MPa	24	19	19	62
Y_c, Z_c, MPa	113	105	105	155
S_{12}, MPa	57	25	25	97
S_{13}, MPa	57	25	25	87
S_{23}, MPa	14	14	14	21
ρ, kg/m^3	1617	1815	1860	1940

* obtained by measurements, the rest is from [76].

5.4 Manufacturing and Balancing of the CFRP Flywheel Rotor

The hollow shaft was manufactured using wet filament winding process. In total, a set of six T800S 24 K rovings were combined to achieve a band thickness of about 19 mm and a layer thickness of about 0.4 mm. The different winding angles were applied using different rotating and translational speeds of the CNC winding machine. The sections including the lowest winding angles were manufactured using special winding-pins that were mounted on the steel mandrel before winding operation to guarantee a slight pretension force of 20 N, see Fig. 5.9(a). After the winding operation, see Fig. 5.9(b), the mandrel including the unmachined part was cured in an oven with an defined cycle of 1st: 2h/100°C, 2nd: 6h/150°C, 3rd: 1h/60°C.

The finished cured part was then pulled off the mandrel by a hydraulic cylinder and the contour including the tolerances where machined using a CNC turning operation, see the finished shaft in Fig. 5.9(c).

The three rings where manufactured in the same way as the shaft but due to the hoop winding operation the mandrel setup is different as shown in Fig. 5.9(d). For the inner rings the T800S fiber, whereas for the outer ring the stiffer K13916 fiber was used. After curing with the identical cycle as the shaft was cured, the rings where separated and the conical contour including the interference-fit tolerances where machined. The three rings where then assembled by press-fitting with a 4 MN hydraulic press, see Fig. 5.9(e). First the inner two rings where press-fitted followed by the outer ring. In Fig. 5.9(f) the finished machined inertia mass is shown. In the meantime the hollow shaft was finished by inserting liners for mounting of the AMB and M/G parts as well as by thermal fitting of the aluminium sensor rings onto the shaft.

The shaft was then centric positioned inside the inertia mass, see Fig. 5.9(g) and afterwards the two parts where press-fitted together by a steel pressure pad and the 4 MN hydraulic press shown in Fig. 5.9(h). The assembling was then completed by mounting the rotor components of the axial and radial AMB's and the M/G parts, see Fig. 5.9(i).

The advantage of the hollow shaft is the possibility to integrate a wireless measurement system inside the core, see Fig. 5.10(a). This four channel system with a sampling frequency of $f_s = 125$ Hz communicates via Bluetooth with the measurement PC. Three of the four channels where used as quarter bridges for strain gauges applied onto the inertia mass to online measure defined strains as well as the temperature of the shaft with the fourth channel. The strain gauges applied on the inner and middle ring are depicted in Fig. 5.10(b) and Fig. 5.10(c).

After inserting the measurement system, the FESS rotor was ready for balancing. This was done by an automatic balancing machine that performs a dynamic unbalance correction in two planes described in [104]. The corrective masses, for a run at $\omega = 180\,s^{-1}$, of $A = 4.84$ g and $B = 4.35$ g made of CFRP where applied by epoxy resin inside the circumference of the outer ring. With this a quality grade of G2.5 mm/s, defined in [105], was reached. The machine and the applied corrective masses are shown in Fig. 5.11.

Figure 5.9: Fabrication and assembling of the FESS rotor: (a) steel mandrel with symmetric mounted winding pins; (b) winding operation of the hollow shaft; (c) finished machined shaft; (d) steel mandrel for hoop winding operation; (e) press-fitting of the rings; (f) finished machined inertia mass; (g) centric positioning of the shaft; (h) press-fitting of the shaft and the inertia mass by hydraulic press; (i) finished assembled rotor including the components of the axial and radial AMB's and the M/G.
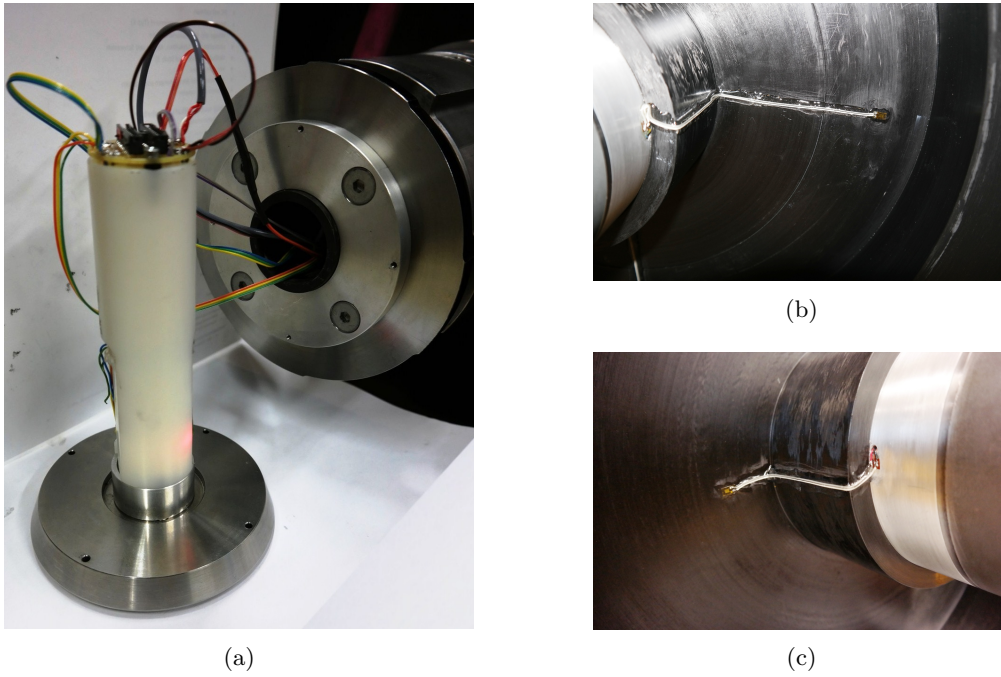
Figure 5.10: Wireless measurement system: (a) cylinder including the GSV-4BT system, lithium ion battery and the interface for the sensors; (b) radial strain gauge on middle ring; (c) radial strain gauge on inner ring.
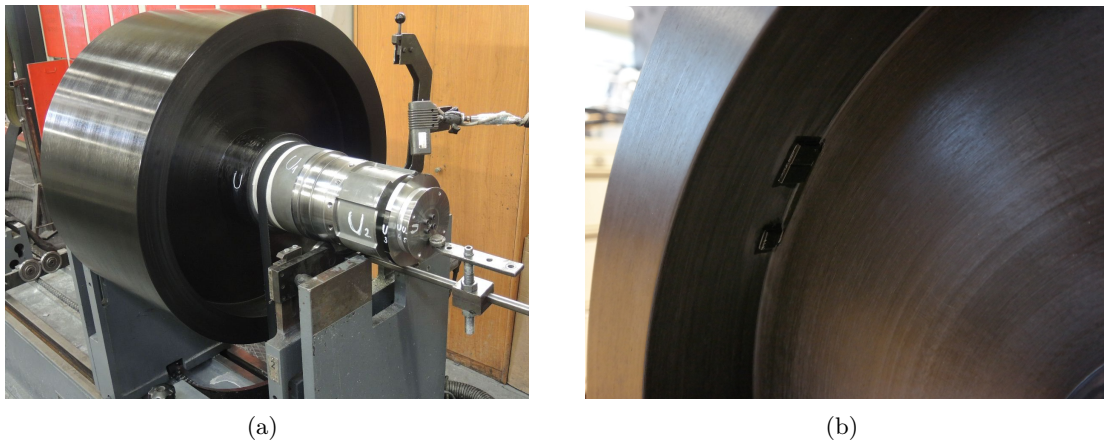

Figure 5.11: Automatic balancing of the FESS rotor: (a) balancing machine; (b) resulting corrective masses.
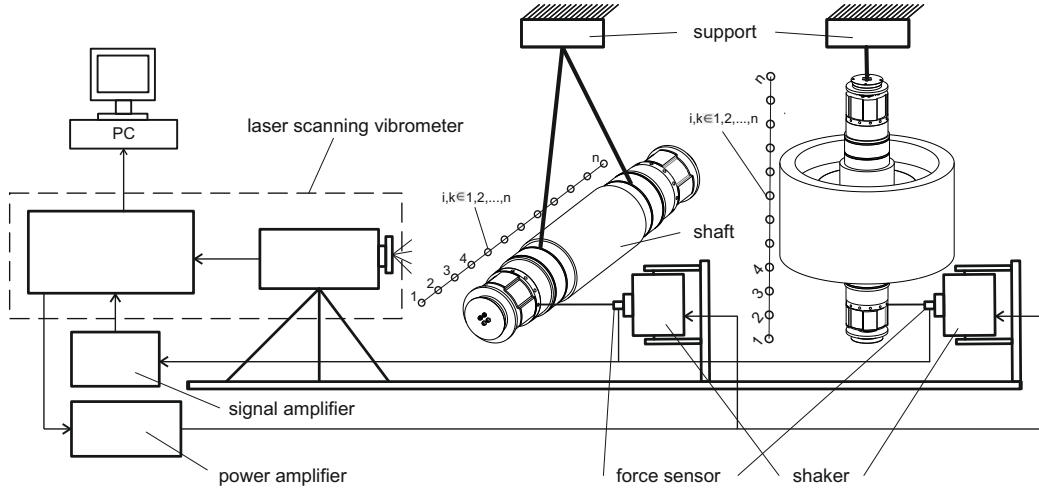
Figure 5.12: FVT testing scheme for the assembled shaft and the FESS rotor.

5.5 Experimental Results

This section presents the results of the experiments conducted on the prototype FESS system described above. At first the essential machine parameter that is directly measurable is presented. The spinning experiments and the efficiency test are performed with a maximum speed of $\omega = 440\,\text{s}^{-1}$, due to power electronic restrictions and sensor noise. The section closes with a discussion of the overall results from the experiments and compares them to simulation results and design criteria mentioned above.

5.5.1 Prototype Machine Parameter: Rotor Natural Frequency

Accurate prediction of the natural frequencies and mode shapes of the rotor are necessary to prevent excessive bearing loss and even catastrophic failure due to unwanted excitations or normal operating conditions. For a successful operation of a FESS, the knowledge of the natural frequencies of the rotor and its components is of major interest. In the following the complete assembled shaft without the inertia mass and the finished FESS rotor are experimentally analyzed and compared to simulations using modal analysis.

Experimental Modal Analysis (EMA)   Forced vibration testing (FVT) is performed to identify the shafts and the FESS rotor modal characteristics. Therefore, both structures were artificially excited in point i and its response $y_k(t)$ to this excitation is measured together with the forcing signal $x_i(t)$. By transformation of these time signals into the frequency domain, the frequency response matrix $\boldsymbol{H}(j\omega)$ can be found. By assuming a linear system, $\boldsymbol{H}(j\omega)$ is diagonal and so the excitation point i can be kept constant while measuring the response over the shaft in the n points, see Fig. 5.12. The structural responses were measured in discrete points by a PSV-500-H4 laser scanning vibrometer
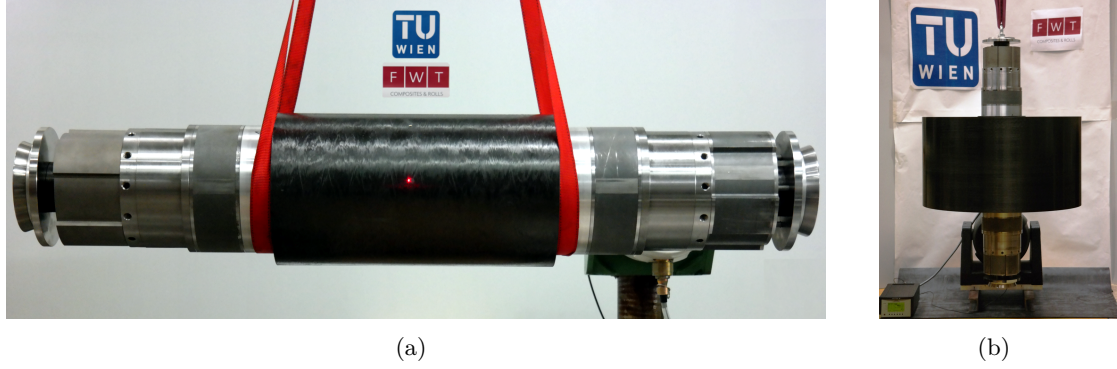
(a)   (b)

Figure 5.13: Free-free support: (a) assembled shaft including the motor-/bearing components; (b) FESS rotor.

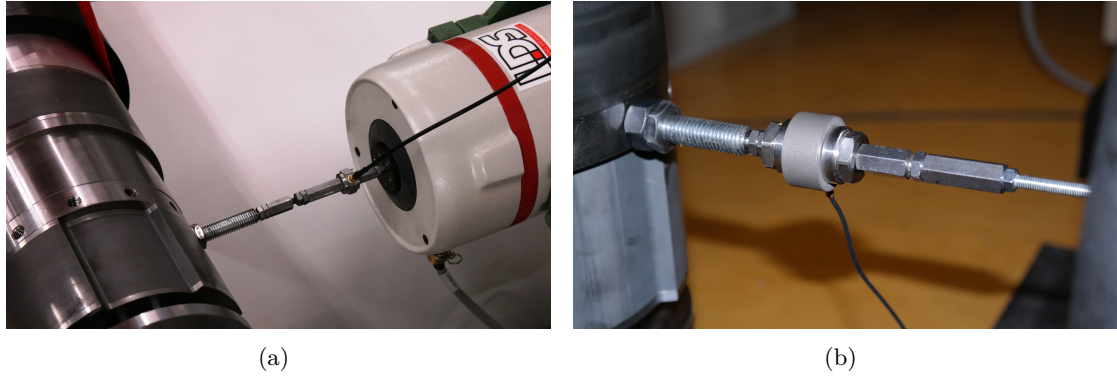(a)   (b)

Figure 5.14: Force excitation by electrodynamic shaker and force measurement by piezo-electric sensor: (a) assembled shaft; (b) FESS rotor.

(LSV) in a non contact way. Therefore, the structures were supported by "free-free" boundary conditions, with elastic bands hung up at a fixed support, see Fig. 5.13(a) and Fig. 5.13(b). The force input was provided by a coupling rod, including a piezoelectric force sensor that was mounted on an electrodynamic shaker, see Fig. 5.14(a) and Fig. 5.14(b). The excitation signal used was a band limited white noise ($0 - 2\,\mathrm{kHz}$ and $0 - 0.5\,\mathrm{kHz}$).

The movement of the axis was observed in $n = 70$ points for the shaft and in $n = 190$ points for the rotor. The excitation point was kept constant in point $i = 10$ for the shaft and in point $i = 26$ for the rotor. The measurements were filtered and averaged ($n_{AVG} = 20$). Then the best measurable natural bending frequencies and the corresponding mode shapes were extracted out of the average accelerance frequency response function (FRF) over all measured points. The measured natural frequencies and damping ratios are listed in Table 5.3 and the measured mode shapes are depicted in Fig. 5.15(a) and Fig. 5.15(b).
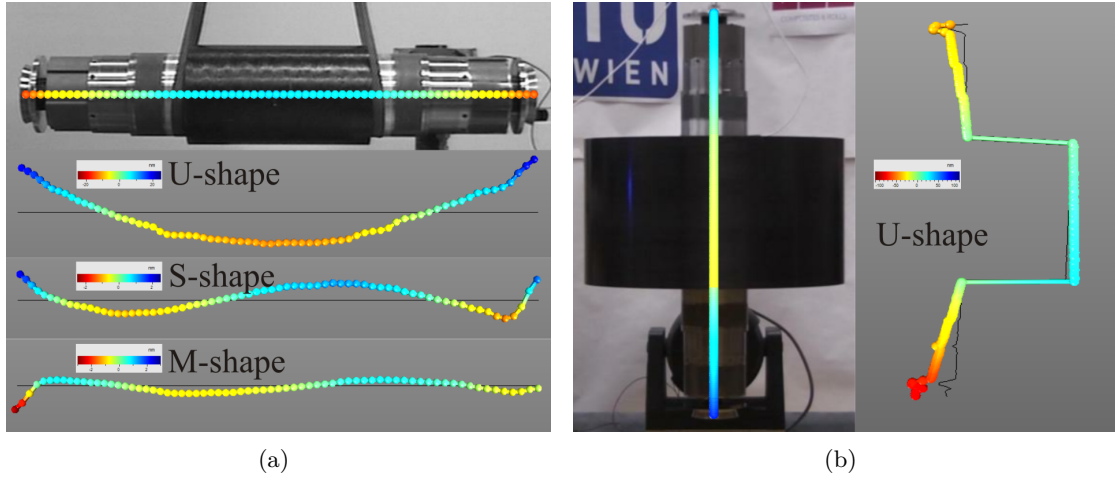
Figure 5.15: Out of plane deformation of measured mode shapes in nm: (a) assembled shaft; (b) FESS rotor.

Finite Element Modal Analysis (FEMA)   The bending natural frequencies for the FE model of the shaft and rotor are then compared to the experimental measured data. This was done in two ways. Firstly, a harmonic analysis without damping was carried out over the same frequency range like in the EMA with a step size of $\Delta f = 2\,\text{Hz}$.

Therefore, both models were excited in the same point $i = 10$ and $i = 26$ by a harmonic load. The point acceleration FRF's of point $k = 1$ and $k = 35$ for the shaft $k = 1$ and $k = 46$ for the rotor where calculated and are then compared to the EMA results shown in Fig. 5.16 and Fig. 5.17. The FEMA results of $H_{1,10}$ and $H_{35,10}$ agree well with the EMA locations of the first two bending modes (1.BM and 2.BM) and the same can be seen for the result of $H_{1,26}$ and $H_{46,26}$ for the first bending mode (1.BM) of the rotor.

Table 5.3: Experimental and simulated results.

Mode shape	EMA (LSV) f in Hz	ζ in %	FEMA (harmonic, undamped) f in Hz	FEMA (modal, damped*) f in Hz	ζ in %
Assembled shaft without inertia mass					
1.BM "U-shape"	368	1.01	398.98	398.96	1.23
2.BM "S-shape"	874	1.45	870.31	870.23	1.35
3.BM "M-shape"	1291	1.78	1212.3	1212.1	1.69
FESS rotor					
1.BM "U-shape"	270	1.11	300.46	300.44	1.15
2.BM "S-shape"	-	-	360.08	360.06	1.05

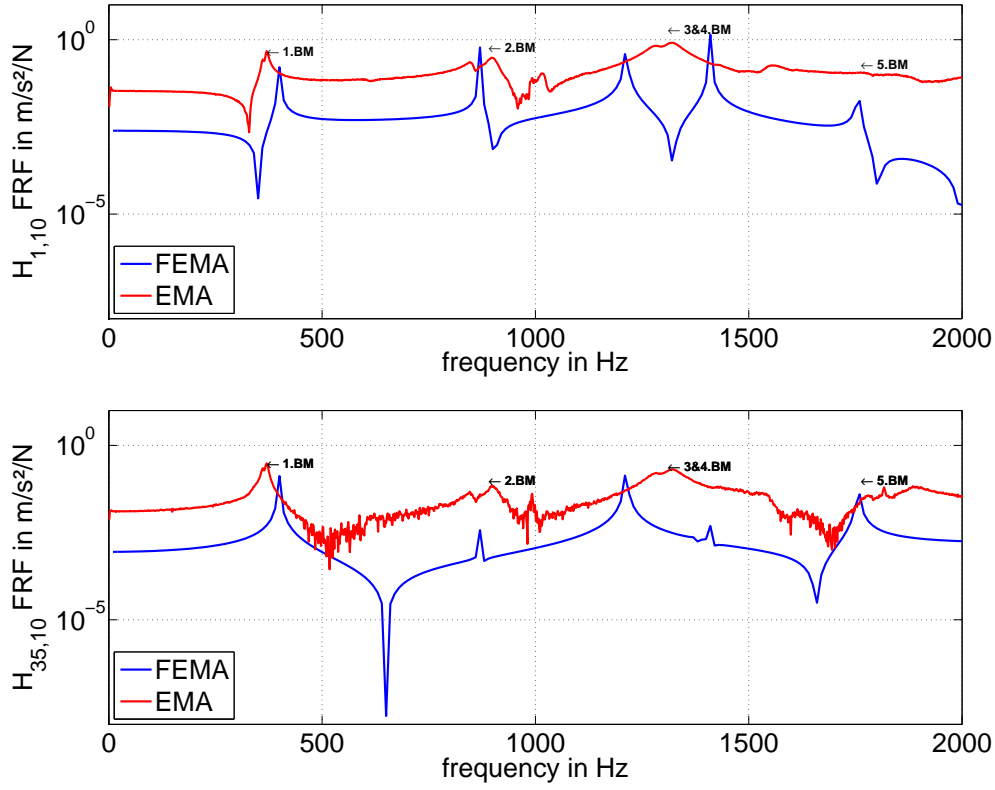* shaft:$\alpha = 30.96$ and $\beta = 0.000003895$

Figure 5.16: Shaft point accelerance FRF of finite element modal analysis (FEMA) and experimental modal analysis (EMA) at two different locations: response in point $k = 1$ and $k = 35$ and excitation in point $i = 10$.

Due to large damping of the material at higher frequencies, the EMA results show only a well damped 3.BM and no more determinable modes in this frequency range for the shaft. A similar EMA result shows the rotor measurement, where only the first bending mode can be clearly identified. This is also because of the fact that due to the large rotor mass it is hard to get enough energy into the system over this broad frequency range. It can also be seen that each mode separates at it's peak. This is caused by non-perfect axisymmetric structures resulting in mode shapes that are not vibrating in the measurement plane. The results of the harmonic analysis are also given in Table 5.3.

Secondly, a modal analysis including Rayleigh damping was performed to study the effect of structural damping. Therefore, a least squares fit was performed to identify the Rayleigh damping coefficients α and β by the given relation $2\zeta_i\omega_i = \alpha + \beta\omega_i^2$. The EMA modal parameter, the damping ratio ζ_i and the damped natural frequency ω_i, of all measurable shaft modes where used for the identification. For the FESS rotor the Rayleigh damping coefficients of the shaft were used. The results are given in Table 5.3.
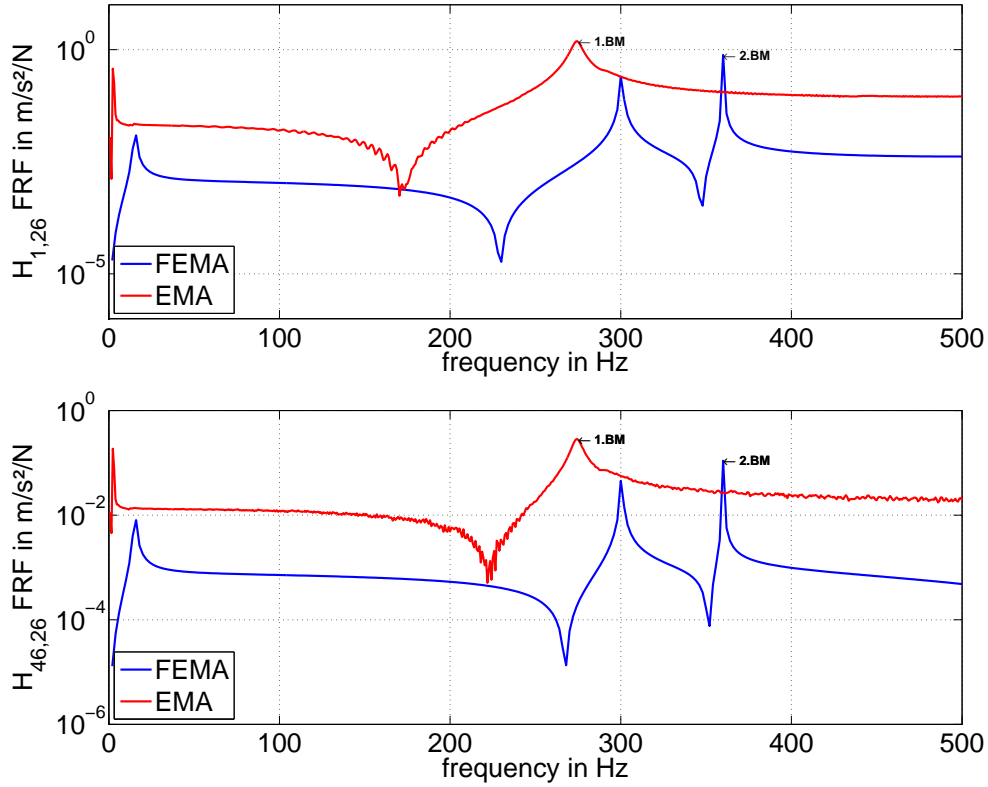
Figure 5.17: Rotor point accelerance FRF of finite element modal analysis (FEMA) and experimental modal analysis (EMA) at two different locations: response in point $k = 1$ and $k = 46$ and excitation in point $i = 26$.

5.5.2 Static Levitation Test

The loops for all control planes are closed by eddy-current based displacement sensors. The sensors for the radial AMB's are working in differential mode to minimize errors due to the high frequency switching inverters and to get double sensitivity. The zero position is calibrated with a sensor calibration ring, see Fig. 5.3(a). The control algorithm used is a decentralized control structure with PID control, detailed explained in [106]. The step responses of both control planes from the start positions (mechanical contact with auxiliary bearings) to operating positions are shown in Fig. 5.18(a) and Fig. 5.18(b).

The rotor moves strict into the center and stays stable within a circle of 0.07 mm radius. The axial position is feed back by a single displacement sensor but also a PID control structure is used. The axial position was calibrated in a different way. Due to the hybrid structure of the axial AMB the zero position was set exactly into the point where the current for the AMB is zero to guarantee energy efficient operation.
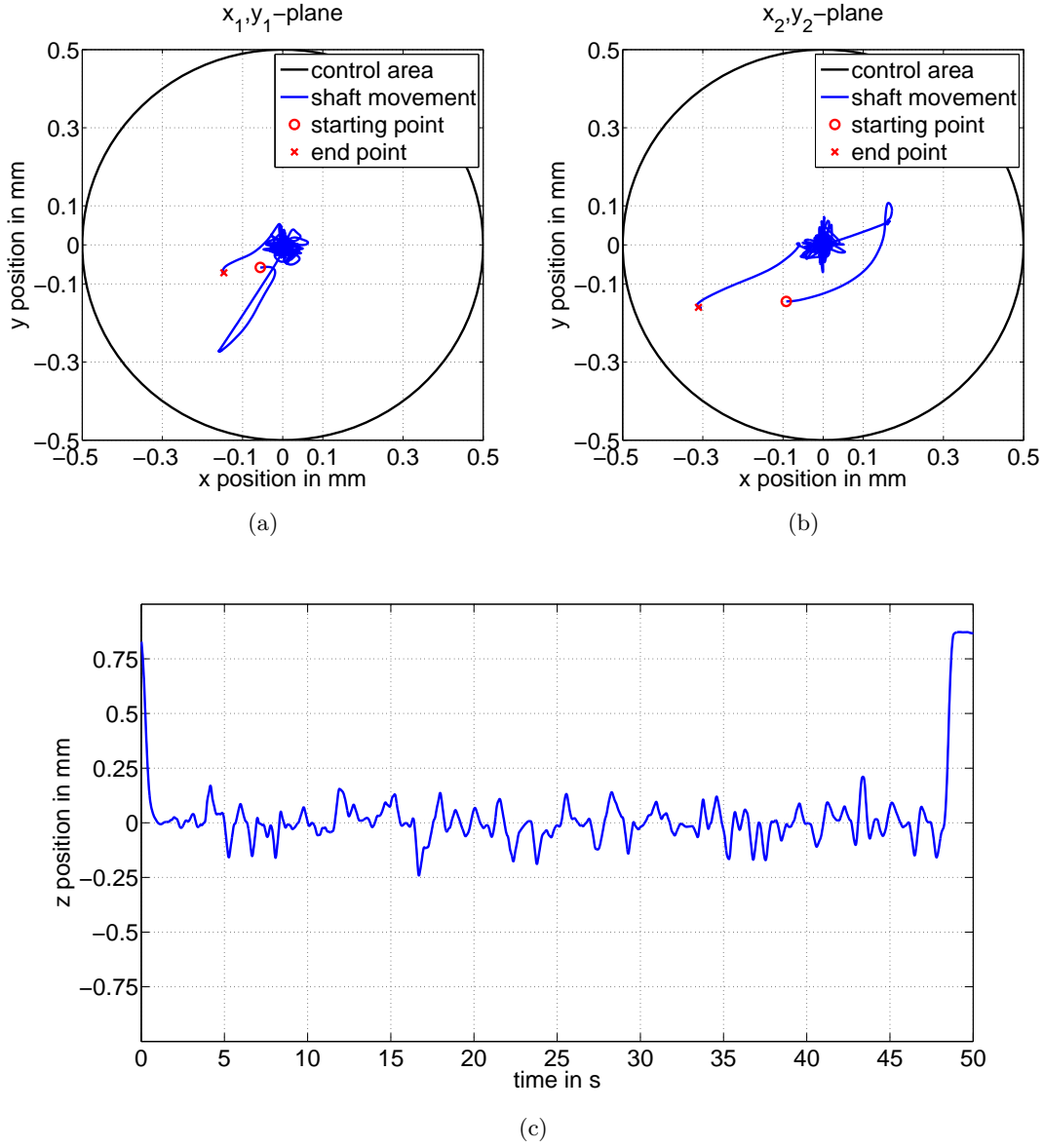
Figure 5.18: Static levitation of the rotor: (a) bottom radial bearing x_1, y_1-plane; (b) top radial bearing x_2, y_2-plane; (c) axial, z-direction

The step response from the start position (mechanical contact with top auxiliary bearing) to zero current position is shown in Fig. 5.18(c). The static levitation of the FESS rotor with a mass of 209 kg requires a power consumption of $P_{\mathrm{AMB}} = 25\,\mathrm{W}$.
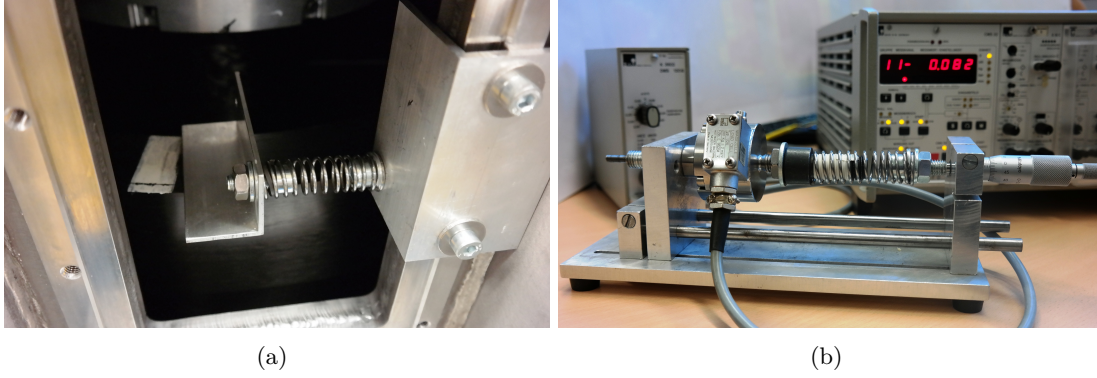
Figure 5.19: Measurement of moment of inertia: (a) applied spring between the rotor and containment; (b) displacement controlled spring constant measuring.

5.5.3 Measurement of Moment of Inertia

One advantage of FESS compared to e.g. batteries, is the accurate knowledge of the actual energy content $E_{\text{act}} = \frac{1}{2}J\omega^2$ due to measuring the angular velocity ω of the rotor. Therefore, the moment of inertia J has to be measured and this is performed by an oscillation test, see Fig. 5.19(a). The levitated rotor is connected by a spring to the containment. This results in a slightly damped free oscillating system with an undamped natural frequency ω_0 that can be calculated out of the systems response due to angular deflection α of the rotor.

Furthermore, by knowing the spring constant k, the moment of inertia can be direct calculated by the relation $J = kr^2/\omega_0^2$, where r is the distance of the spring application point to the axis of rotation. Figure 5.19(b) shows the measurement setup to calculate the spring stiffness constant.

The free oscillation of the rotor is depicted in Fig. 5.20. The damped natural frequency is given by $\omega_d = 2\pi/(t_2 - t_1)$. The damping coefficient is calculated out of the exponential envelope $\delta = log(\alpha_1/\alpha_2)/(t_2 - t_1) = 0.0486\,1/\text{s}$ and then the undamped natural frequency $\omega_0 = \sqrt{\omega_d^2 + \delta^2}$ follows to $\omega_0 = 5.76\,1/\text{s}$. A linear regression of the spring force vs. deflection data results in a spring stiffness constant of $k = 2170.6\,\text{N/m}$. In combination with the given distance $r = 0.34\,\text{m}$ the moment of inertia $J = 7.55\,\text{kgm}^2$ can be calculated.

5.5.4 Vacuum Tests

The vacuum system used for this experiment is a TRIVAC B D25B with a rated power of $P_{\text{vac}} = 750\,\text{W}$ at an minimum pressure of $p_{\text{vac}} = 0.1\,\text{mbar}$. The pressure was measured by a PENNINGVAC PTR90 sensor and observed by the data acquisition system described above. The goal of the first test is to measure the energy needed to evacuate the containment to provide operating condition that was defined by a pressure of $p_{\text{vac,op}} = 0.1\,\text{mbar}$. The second test is to observe the leakage of the containment over a
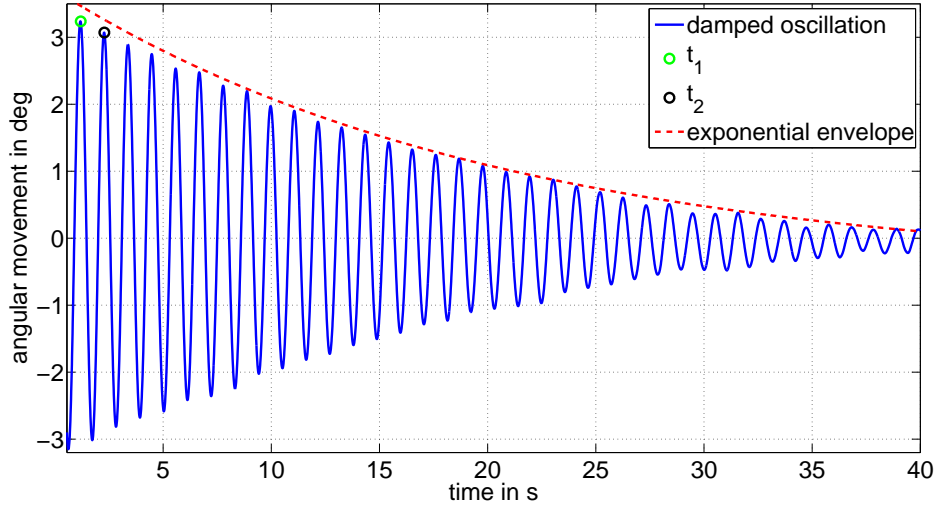
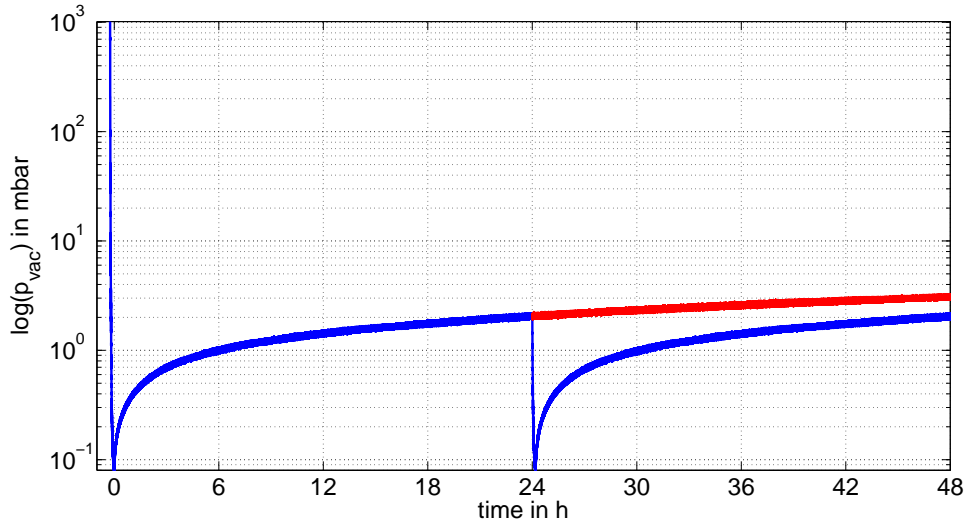Figure 5.20: Angular movement of the rotor due to initial deflection.

Figure 5.21: Containment pressure starting from the initial to operating condition including the leakage curve in red.

defined cycle of $t = 24\,\text{h}$ and measure the energy needed to get back to operating condition. The initial condition takes approximately $15\,\text{min}$ to reach the operating pressure, see Fig. 5.21. After that, the vacuum system is switched off and the vacuum loss due to leakage of the sealings starts. The cyclic cycle of $24\,\text{h}$ is re-evacuated in about $10\,\text{min}$ to reach the operating pressure of $p_{\text{vac}} = 0.1\,\text{mbar}$ again. This results in combination with Fig. 5.22 in an energy loss of $E_{\text{vac,init}} = 180\,\text{Wh}$ for the initial evacuation and
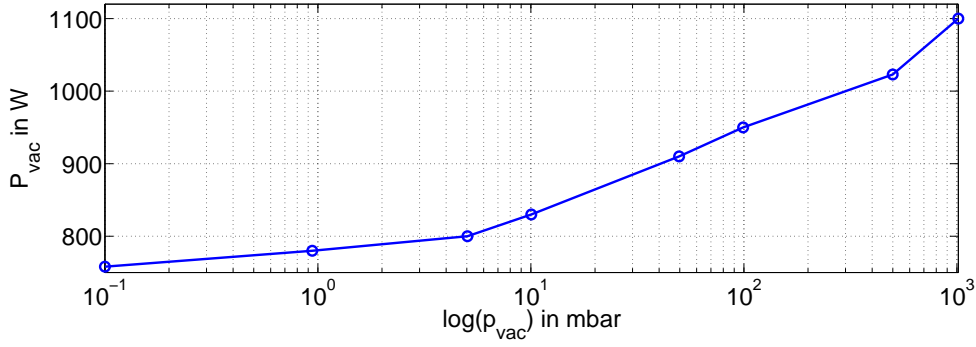
Figure 5.22: Power of the vacuum system for different containment pressure levels measured by a HEME ANALYST 2060 current probe.

$E_{\text{vac,op}} = 125\,\text{Wh}$ for a defined 24 h operation cycle.

5.5.5 Maximum Speed Test

The test was performed starting from the static levitation to a maximum speed of $\omega = 440\,\text{s}^{-1}$ and it's main purpose is to measure well chosen radial strain points of interest to validate the FE simulation used for stress analysis. This is usually performed by non-contact measuring of the radial deformation of the inertia mass or using a special optical pattern on the surface to perform Digital image correlation (DIC) during operation of the FESS.

With the above discussed wireless DAQ system, it is possible to observe up to four points by using quarter bridge operation mode. This implies a temperature compensation and therefore the temperature of the shaft during operation was observed by a PT1000 sensor by one measurement channel. In general the strains where measured by Hottinger Baldwin Messtechnik (HBM) strain gauges with a resistance of $350\,\Omega$ that were directly applied at the predicted maximum value point of the radial strain at the inner two rings, see Fig. 5.10(b) and Fig. 5.10(c). A third strain gauge was applied in hoop direction at the inside of the outer ring but unfortunately it was destroyed during the assembling of the rotor and containment.

The measurement was recorded with a sampling frequency of $f_s = 6\,\text{Hz}$ after evacuation of the containment and settling of the temperature of the shaft. During operation almost no temperature change inside the containment and of the shaft was observed. The relative strain changes due to inertial forces are depicted in Fig. 5.23. The depicted strains are relative because the static levitation is the pre-stressed configuration.

5.5.6 Efficiency Measurements

The FESS efficiency was measured during a spin up (charging of the system) and spin down cycles (discharging of the system) over a defined 2 : 1 speed range. The acceleration starts at a speed of $\omega = 120\,\text{s}^{-1}$ and is followed by deceleration from $\omega = 220\,\text{s}^{-1}$.
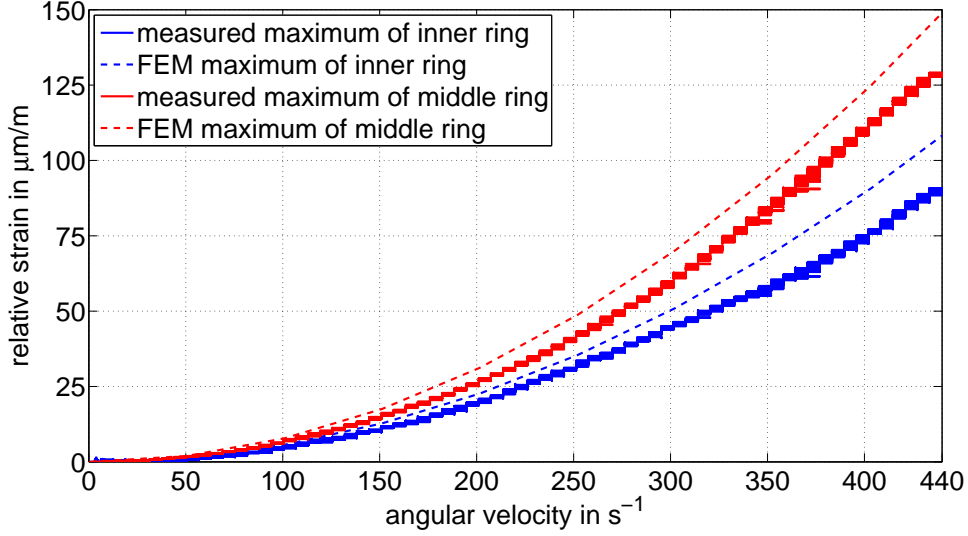
Figure 5.23: Measured vs. FEM radial strains on the inner and middle ring.

At first it must be mentioned that the chosen range is not the designed operating speed range of the presented FESS ($\omega_{\min} = 460\,\mathrm{s}^{-1}$ to $\omega_{\max} = 1460\,\mathrm{s}^{-1}$, $90\,\%$ DOD) and so the measurement will not represent the normal FESS operation mode. This measurement is used to measure only the electrical losses, because the starting speed is equal to the ending speed and so the mechanical power during the measurement is zero.

Therefore the integral of the output power P_{out} minus the power of the rotor loss P_{loss} divided by the sum of the inputted power $P_{\mathrm{in,i}}$ over the test time is used to calculate the average efficiency over the test cycles by

$$\eta_{\mathrm{avg}} = \frac{\int_0^T (P_{\mathrm{out}} - P_{\mathrm{loss}})\, dt}{\int_0^T \left(\sum_{i=1}^n P_{\mathrm{in,i}}\right) dt} \ , \tag{5.16}$$

where the input powers $P_{\mathrm{in,i}}$ are separated in the electrical power of the axial- and the two radial bearings, the motor/generator power, the sensor and controller power and the power for the vacuum system, see Fig. 5.24.

By using Eqn. (5.16) the average efficiency can be calculated out of the directly measured currents and voltages of all linked voltage DC buses, where all electrical losses, e.g. AMB, M/G, harmonic losses, etc., are included. The average efficiency for the test cycles, shown in the top of Fig. 5.24, calculates to $\eta_{\mathrm{avg}} = 32.4\,\%$.

To calculate the actual efficiency of the FESS at any operating point it is necessary to use the mechanical power P_{Rotor} by using the above measured moment of inertia J, the measured actual angular velocity ω and the angular acceleration $\dot{\omega}$ to calculate the efficiency η_{act} for charging and discharging of the FESS.

$$P_{\mathrm{Rotor}} = J\omega\dot{\omega} \ , \tag{5.17}$$
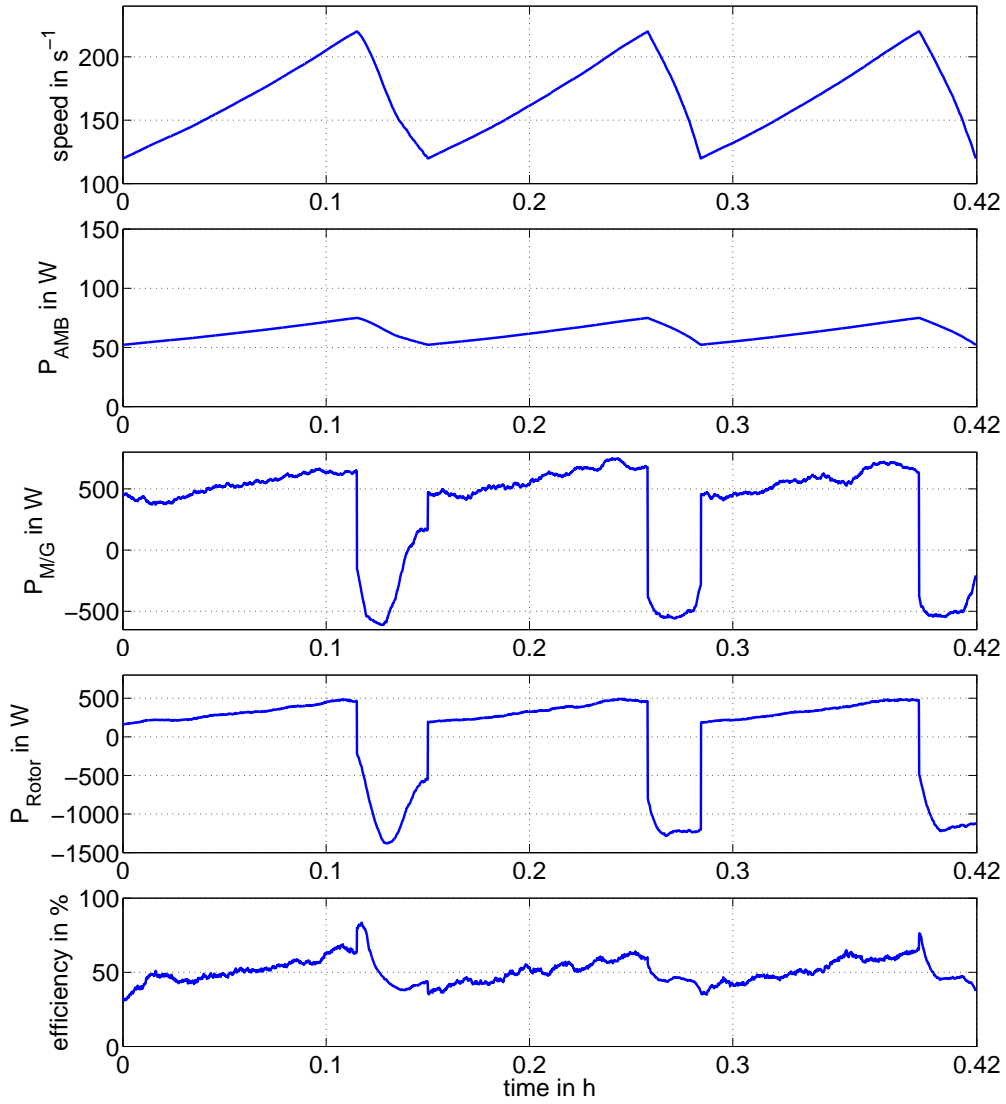
Figure 5.24: Measured power of the AMB's, M/G and the rotor for the defined speed range and cycles. The measurement was performed by Tektronix, MSO 4054 oscilloscopes, TM502A current amplifiers and A6302 current probes.

$$\eta_{\text{act}_{\text{charging}}} = \frac{P_{\text{Rotor}} - P_{\text{loss}}}{P_{\text{M/G}} + P_{\text{AMB}} + P_{\text{vac}} + P_{\text{sense\&control}}} \ , \qquad (5.18)$$

$$\eta_{\text{act}_{\text{discharging}}} = \frac{P_{\text{out}} - P_{\text{loss}}}{\mid P_{\text{Rotor}} \mid + P_{\text{M/G}} + P_{\text{AMB}} + P_{\text{vac}} + P_{\text{sense\&control}}} \ . \qquad (5.19)$$

The actual efficiency for the three cycles as well as the power consumptions are shown in Fig. 5.24 and also summarized in Table 5.4.

5.5.7 Analysis of Results

The energy density of a flywheel rotor is a quantity to compare materials suitable for FESS applications and to compare different storage technologies, see [21, 22, 107]. The values for composite rotors are in all cases higher than their competitors promising the advantage of FESS, see Table 5.5. There, the energy density κ is calculated with the assumption of an infinite thin, hoop wound hollow cylinder, the ultimate strength in fiber direction X_t and the density of the material ρ by

$$\kappa = \frac{1}{2}\frac{J\omega_{\max}^2}{m} = K\frac{X_t}{\rho} \ , \tag{5.20}$$

with K defining the geometric shape factor. In fact, the above shown calculation is not valid for any realizable FESS rotor. Therefore, one has to consider the stress component in radial direction that is included in the, e.g. Tsai-Wu failure parameter R_{TW} forming the adapted shape factor $\bar{K}$ depending on geometric and material attributes. The energy density for a general rectangular geometry, shown in Fig. 5.25(a) with a radii ratio $\chi = r_i/r_a$ is independent from the axial length h and defines as follows

$$\kappa = \frac{1}{2}\frac{J}{m}\frac{X_t}{\rho r_a^2} = \underbrace{\frac{1+\chi^4}{4}}_{K}\underbrace{\frac{1}{S_{R_{TW}}R_{TW}}}_{\bar{K}(\chi,\mathrm{mat})}\frac{X_t}{\rho} \ . \tag{5.21}$$

The geometric dependency of $\bar{K}$ for T800S/705 in Table 5.2 is depicted in Fig. 5.25(b). For the infinite thin hollow cylinder ($\chi = 1$) the energy density results in (5.20). The solid disc or cylinder ($\chi = 0$) shows a 83 % lower energy density, compared to $\chi = 1$, due to the low radial strength. It is also observed that for a small range of χ the energy density rises up to 5 % as a result of the perfect material utilization where the radial and hoop stress are at their limits. Furthermore, implementing a safety factor $S_{R_{TW}} = 2$ further reduces the energy density by 50 %. Common in-runner FESS rotors need a shaft and this negative arrangement (high mass, low radius) is also disadvantageous ending up in a maximal achievable energy density of 11.9 Wh/kg for the designed FESS rotor.

Table 5.4: FESS prototype efficiency test data.

Speed range, s^{-1}	120:220
P_{vac}, W	5.2
$P_{\mathrm{sense\&control}}$, W	11.4
P_{AMB}, W	$\approx 25 + 0.227\omega$
$\lvert P_{\mathrm{M/G}} \rvert$, W	500
P_{Rotor}, W	$= 7.55\omega\dot{\omega}$
P_{loss}, W	$\approx 12.7 \cdot 10^{-5}\omega^2$ at $p_{\mathrm{vac}} = 0.1\,\mathrm{mbar}$
η_{avg}, %	32.4

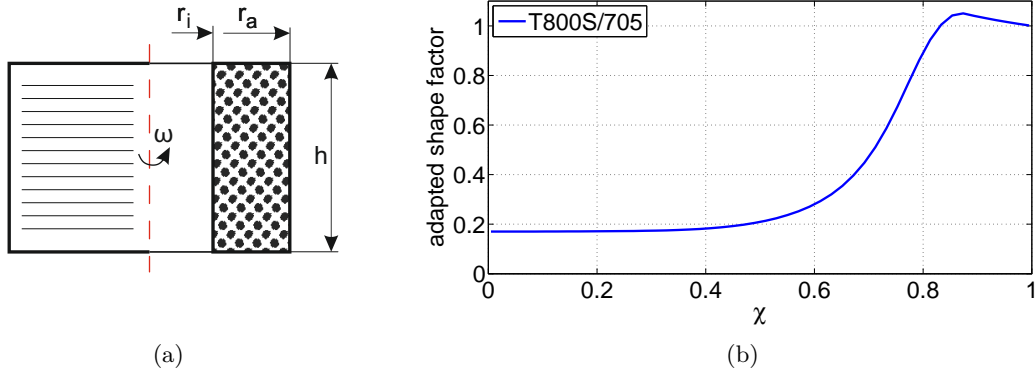(a)   (b)

Figure 5.25: Energy density of a FESS rotor: (a) geometry of the inertia mass; (b) T800S/705 adapted shape factor $\bar{K}(\chi, \text{mat})$ for $S_{R_{TW}} = 1$.

The measurement of the natural frequencies is largely depending on the boundaries and the nature of the structure. As a general rule it can be mentioned that, the stiffer and lighter a structure is, the harder is the measurement due to low displacement amplitudes. Both analyzed structures are stiff enough to see almost no difference in the output by changing the material, geometry or length of the elastic bands for the "free-free" support. The measured and simulated results, summarized in Table 5.3, show a relative error of 11 % for the first bending mode. The reasons for that can be explained from two different point of views, firstly the modeling error that is always present due to assumptions that make the mater easier to handle and secondly there are a lot of influencing factors that show up from the manufacturing of the designed rotor.

Table 5.5: Energy storage types out of [21, 22, 107].

Storage type	κ in Wh/kg
Electrochemical reaction	
Lead-acid battery	30-50
NiMH battery	60-120
Li-ion battery	90-190
Kinetic energy, flywheel	
Steel	67
Aluminium	83
Kevlar	213.8
CFRP (T300/2500)	562
CFRP (T800S/705)	189
Designed FESS rotor	11.9

During the manufacturing, deviations from the simulated rotor occurred because of

- changing of the geometry (adding chamfers) to ensure a problem-free press-fit of the components,

- changing of the geometry (diameters and interferences) due to tolerances and limits of the available machinery,

- the pretension force as well as the winding diameter directly influence the material parameter of the CFRP and even though if the material parameter are measured correctly due to specimen that are manufactured in the same way as the rotor is, the material parameter of the thick wound parts can differ easily in axial or radial direction and

- the exothermic reaction during the hardening of the CFRP leads to thermal induced pre-stresses that also influence the structural behavior.

The measurement of the moment of inertia and the true weight of the rotor show the discrepancy. The simulation resulted in a total weight of $m_{\mathrm{simu}} = 216\,\mathrm{kg}$ and a moment of inertia of $J_{\mathrm{simu}} = 8.75\,\mathrm{kgm^2}$. The real total weight of the rotor shown in the balancing protocol is $m_{\mathrm{real}} = 209\,\mathrm{kg}$ and the moment of inertia measurement resulted in $J_{\mathrm{real}} = 7.55\,\mathrm{kgm^2}$. The relation for the natural undamped frequency $\omega = \sqrt{k/m}$ leads to the most causal explanation for the difference in the results that the stiffness (quantitatively assumed as the stiffness parameter k) of the CFRP material is in real less than the assumed parameters for simulation.

This effect is also visible in the strain measurement during operation. The measured strain curves run underneath the simulated ones and this is an indicator for less stiffness in the radial direction. Furthermore, both strain curves show the expected quadratic dependency on the angular speed and also no hysteresis behavior was found in speeding up or down. This makes the adoption of linear material behavior valid.

The start up of the FESS prototype begins with the evacuation of the containment followed by the static levitation of the rotor. The evacuation moves quickly and the leakage is much less than expected. This can further be improved by omitting the service windows used for the prototype. Another factor is the relatively long lasting out-gas process of the CFRP that increases pressure after shut down of the vacuum system.

The parameter tuning for the control algorithms of the AMB's showed the large potential of this type of bearing. Thereby, it must be mentioned that the design strategy of an AMB must be fixed from the beginning, because the power consumption and further it's efficiency is inversely proportional to the performance. This fact shows the comparison between the static and dynamic power consumption. In the static case the stiffness and damping of the AMB can be decreased so that the power consumption is a minimum.

During operation a very stiff and fast acting AMB is needed to guarantee no contact with the auxiliary bearings and this is directly related to a linear increase of the consumed power depending on speed.

The M/G for charging and discharging is the most difficult component in this FESS prototype. In first this type of motor is highly efficient but the control effort is enormous. In fact, everything is dependent on the switch on/off angle and therefore a very accurate angle measurement is necessary to be able to perform the needed force compensation, speed and high efficient power control. Within this prototype, the angle at low speeds is measured by an magnetic absolute angle position sensor with pulse width output, but at higher speeds the actual angle is derived out of an incremental pulse that is highly effected by noise produced by the high voltage driven inverters for the M/G.

In fact, the maximum speed reached is the result of a vicious circle, because to speed up, high voltage to fast rise the current in a coil and an exact switch on/off angle is needed, but increasing the voltage increases the sensor noise that leads to wrong calculated angles that further decelerates the rotor and due to the generated high radial forces also a fall down of the rotor is possible. Anyway, even for the measured speed range discussed above, the basic working principle of a FESS could be well studied. The measured efficiency is for this prototype, the lowest possible value.

In the following, an extrapolation for the designed operating speed range is given with respect to the measured characteristics of the FESS prototype and some conservative chosen assumptions based on the validation experiments in [87, 101] and the observed results in Table 5.4. The dynamic characteristic of the FESS rotor can be described by the momentum balance

$$ J\dot{\omega} + a\omega = \begin{cases} M_t & \text{charging} \\ 0 & \text{storing} \\ -M_t & \text{discharging} \end{cases}, \tag{5.22} $$

where a denotes the coefficient of air friction ($\approx 12.7 \cdot 10^{-5}$ at $p_{\text{vac}} = 0.1\,\text{mbar}$) and M_t is the assumed average torque of the designed M/G with a power of 5 kW and a charging/discharging efficiency of 95 % defining the upper limit for the efficiency of the assumed cycle of the FESS prototype $\eta_{\text{avg,max}} = 90.3\,\%$. The solution of the above given first order differential equation defines the speed profile, shown in the top of Fig. 5.26. With $M_t \approx 7\,\text{Nm}$ an ideal charging and discharging time of $\approx 30\,\text{min}$ can be achieved.

Due to the fact, that the applied vacuum can further be improved to $10^{-3}\,\text{mbar}$ the rotor losses are a maximal value. Furthermore, the assumed linear dependency of the AMB power consumption on speed is too conservative. Therefore, the minimum efficiency for the assumed cycle, calculates by use of (5.16) and Table 5.4 to $\eta_{\text{avg,min}} = 76.9\,\%$.
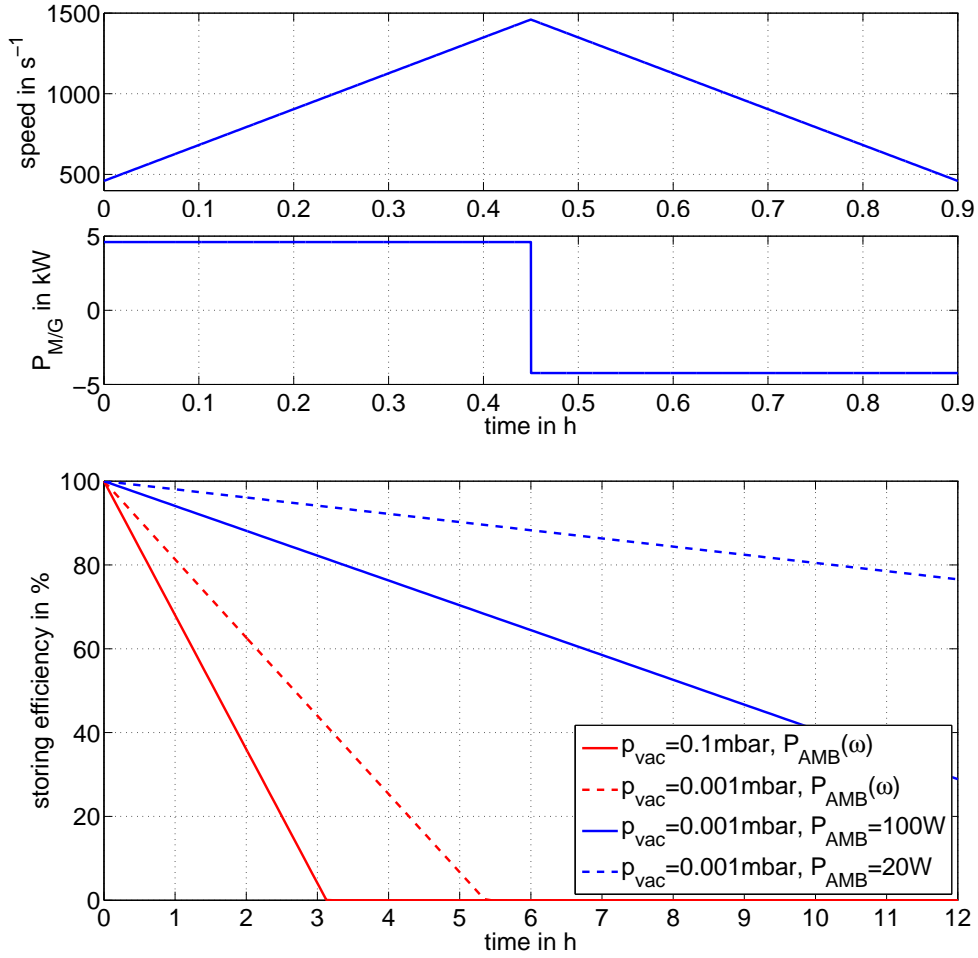
Figure 5.26: Assumed FESS characteristics for the designed operating speed range.

The overall efficiency is the product of the charging/discharging efficiency η_{avg} and the storing efficiency η_{store} , derived by the total stored energy $\text{TSE} = \frac{1}{2} J \left(\omega_{\max}^2 - \omega_{\min}^2 \right)$ to

$$\eta_{\text{store}} = \frac{\text{TSE} - \left[P_{\text{vac}} + P_{\text{sense\&control}} + P_{\text{AMB}}(\omega) + P_{\text{loss}}(\omega) \right] t}{\text{TSE}} \ , \tag{5.23}$$

where the solution of (5.22) for storing is used to calculate the speed dependent power consumptions of the AMB's and the rotor loss. The time dependent storing efficiency is depicted in the bottom of Fig. 5.26 and shows a huge dependency on losses due to air friction and AMB operation. Therefore, high quality vacuum and energy efficient AMB's ($P_{\text{AMB}} < 20\,\text{W}$) or passive magnetic bearings are needed for a successful high speed FESS used for long term storage.

6 Conclusion

High speed fiber reinforced rotors are the key to success for efficient FESS. Precise FE simulations are absolutely necessary to ensure safe and efficient operation of the FESS rotor. Therefore, the knowledge of the mechanical behavior and the modeling of FRP materials is essential. Within this thesis, the design of a fiber reinforced FESS rotor is presented, starting from the beginning of the material selection until the validation through experiments performed on test specimen or within the FESS test rig.

The optimization of the inertia mass showed the large potential of an assembled configuration using press-fits and different materials in radial direction compared to a thick wound inertia mass. Therefore, a lot of elastic material parameters need to be measured, that is, if performed in a destructive way, a costly and very time consuming task. Within this thesis some nondestructive methods based on modal analysis were presented that only need one measurement for each material. With a sufficient accuracy compared to destructive material tests, these methods are appropriate for material characterization and selection. In contrast, for stress and rotordynamic analysis, especially for the presented new CFRP hollow shaft design, the whole set of elastic and strength material parameters must be determined through destructive material testing according to standards that was performed on high strength and high modulus CFRP material.

High rotor speeds cause high kinetic energy that is explosively released in case of a burst event. Therefore, burst tests must be performed for every new rotor design to know the limits. These tests are dangerous and costly that leaded to a new idea of a FSBT method to replace this dynamic burst test. The in this thesis presented FSBT was used to burst a CFRP flywheel rotor with nearly the same stress distribution as in the dynamic case rotating with maximum speed. Failure prediction was done using different maximum stress criteria and a safety factor calculated using the Tsai-Wu criterion. Dynamic simulation results of a FESS rotor and static simulation results of the FSBT are in very good agreement including the failure point as well as the stress distribution and the maximum load.

Furthermore, the test procedure has been proved experimentally utilizing a universal testing machine and a scaled flywheel rotor. The experiment proves the static simulation of the FSBT. Furthermore, the quasi-static FE simulation results of the flywheel rotor using inertia loads compare well to the experimental data of the static burst test. The assumption of a linear system agrees very well with the measurement results. Also the importance of the radial strength of the used material, especially for thick-walled rotor geometries was found, which is of major relevance for choosing the correct material and rotor geometry. Hence, the presented test method is a very good controllable and

observable possibility to test a high speed FESS rotor in a static way instead of a much more expensive and dangerous dynamic spin up test.

With the found knowledge it was possible to go one step forward to design a CFRP rotor with a well defined strength safety factor. The in this thesis presented FESS rotor design consists of a CFRP hollow shaft that is press-fitted into a multi-ring CFRP inertia mass where the three rings are also press-fitted together forming a rotor with a H-shaped cross-section. With this configuration an increase of the energy density was achieved compared to an ordinary FESS rotor design using an aluminium shaft press-fitted into a thick wound CFRP inertia mass. Furthermore, inside the core of the shaft a wireless measurement system was integrated to online measure the mechanical strain of specific points on the inertia mass used for the validation of the FE simulations. The FE simulations compare well to the maximum speed test of the FESS as well as the experimental modal analysis of the FESS rotor.

The FESS characteristics was measured by static and dynamic tests where the static levitation experiments showed the huge potential of high efficient AMB's. The dynamic tests beyond a certain test speed failed due to power electronic restrictions. Therefore, all performed efficiency tests were performed in a lower speed range that do not represent the FESS normal operation. Furthermore, an extrapolation for the designed operating speed range showed that the efficiency of the M/G is the upper maximum efficiency for a short term storage FESS, typically $\eta_{\mathrm{avg,max}} \approx 90\,\%$ for switched reluctance machines, whereas the long term storage efficiency is largely dependent on the quality of the vacuum and the power consumption of the AMB's. The discussed example showed that for a very low power consuming AMB ($P_{\mathrm{AMB}} < 20\,\mathrm{W}$) and a high quality vacuum ($p_{\mathrm{vac}} \leq 10^{-3}\,\mathrm{mbar}$) a no-load loss of 2% per hour, based on the maximum energy content, is possible.

Bibliography

[1] P. V. Joshi, N. K. Jain, and G. D. Ramtekkar. Analytical modelling for vibration analysis of partially cracked orthotropic rectangular plates. *European Journal of Mechanics A/Solids*, 50:100–111, 2015.

[2] M. V. Quintana and L. G. Nallim. A variational approach to free vibration analysis of shear deformable polygonal plates with variable thickness. *Applied Acoustics*, 71:393–401, 2010.

[3] D. S. Cho, B. H. Kim, J. Kim, N. Vladimir, and T. M. Choi. Forced vibration analysis of arbitrarily constrained rectangular plates and stiffened panels using the assumed mode method. *Composites Science and Technology*, 90:182–190, 2015.

[4] N. Kolarevic, M. Nefovska-Danilovic, and M. Petronijevic. Dynamic stiffness elements for free vibration analysis of rectangular mindlin plate assemblies. *Sound and Vibration*, 359:84–106, 2015.

[5] S. Su, G. Jin, and X. Wang. Free vibration analysis of laminated composite and functionally graded sector plates with general boundary conditions. *Composite Structures*, 132:720–736, 2015.

[6] M. V. Quintana and R. O. Grossi. Free vibrations of a generally restrained rectangular plate with an internal line hinge. *Applied Acoustics*, 73:356–365, 2012.

[7] L. Xin and Z. Hu. Free vibration of simply supported and multilayered magneto-electro-elastic plates. *Composite Structures*, 121:344–350, 2015.

[8] D. H. Oh and L. Librescu. Free vibration and reliability of composite cantilevers featuring uncertain properties. *Reliability Engineering and System Safety*, 56:265–272, 1997.

[9] V. N. Burlayenko, H. Altenbach, and T. Sadowski. An evaluation of displacement-based finite element models used for free vibration analysis of homogeneous and composite plates. *Sound and Vibration*, 358:152–175, 2015.

[10] D. Matthews, H. Sun, K. Saltmarsh, and et al. A detailed experimental modal analysis of a clamped circular plate. In *43rd International Congress on Noise Control Engineering*, 2014.

[11] K. G. Muthurajan, B. Sanakaranarayanasamy, and B. Nageswara Rao. Evaluation of elastic constants of specially orthotropic plates through vibration testing. *Journal of Sound and Vibration*, 272:413–424, 2004.

[12] E. O. Ayorinde and L. Yu. On the elastic characterization of composite plates with vibration data. *Sound and Vibration*, 283:243–262, 2005.

[13] M. Grediac and P. A. Paris. Direct identification of the elastic constants of anisotropic plates by modal analysis: Numerical aspects. *Journal of Sound and Vibration*, 195(3):401–415, 1996.

[14] M. Grediac, N. Fournier, P. A. Paris, and Y. Surrel. Direct identification of the elastic constants of anisotropic plates by modal analysis: Experimental results. *Journal of Sound and Vibration*, 210(5):643–659, 1998.

[15] J. Caillet, J. C. Carmona, and D. Mazzoni. Estimation of plate elastic moduli through vibration testing. *Applied Acoustics*, 68:334–349, 2007.

[16] V. Kostopoulos and D. T. Korontzis. A new method for the determination of viscoelastic properties of composite laminates: a mixed analytical-experimental approach. *Journal of Composites Science and Technology*, 63:1441–1452, 2003.

[17] T. Söderström and A. Rensfelt. Estimation od material functions using system identification techniques. In *Proc. of the International Symposium on Advanced Control of Industrial Processes*, Hangzhou, China, May 23-26 2011.

[18] J. De Visscher, H. Sol, W. P. De Wilde, and J. Vantomme. Identification of the damping properties of orthotropic composite materials using a mixed numerical experimental method. *Applied Composite materials*, 4:13–33, 1997.

[19] M. Matter, T. Gmür, J. Cugnoni, and A. Schorderet. Numerical-experimental identification of the elastic and damping properties in composite plates. *Composite Structures*, 90:180–187, 2009.

[20] M. Matter, T. Gmür, J. Cugnoni, and A. Schorderet. Identification of the elastic and damping properties in sandwich structures with a low core-to-skin stiffness ratio. *Composite Structures*, 93:331–341, 2011.

[21] J. L. Perez-Aparicio and L. Ripoll. Exact, integrated and complete solutions for composite flywheels. *Composite Structures*, 93:1404–1415, 2011.

[22] S. M. Arnold, A. F. Saleeb, and N. R. Al-Zoubi. Deformation and life analysis of composite flywheel disk systems. *Composites: Part B*, 33:433–459, 2002.

[23] S. K. Ha, D. J. Kim, and T. H. Sung. Optimum design of multi-ring composite flywheel rotor using a modified generalized plane strain assumption. *International Journal of Mechanical Sciences*, 43:993–1007, 2001.

[24] S. K. Ha, D. J. Kim, S. U. Nasir, and S. C. Han. Design optimization and fabrication of a hybrid composite flywheel rotor. *Composite Structures*, 94:3290–3299, 2012.

[25] S. K. Ha and J. Y. Jeong. Effects of winding angles on through-thickness properties and residual strains of thick filament wound composite rings. *Composites Science and Technology*, 65:27–35, 2005.

[26] S. Kim, K. Hayat, S. Nasir, and S. Ha. Design and fabrication of hybrid composite hubs for a multi-rim flywheel energy storage system. *Composite Structures*, 107:19–29, 2014.

[27] A. C. Arvin and C. E. Bakis. Optimal design of press-fitted filament wound composite flywheel rotors. *Composite Structures*, 72:47–57, 2006.

[28] B. Bai, L. Zhang, T. Guo, and C. Liu. Analysis of dynamic characteristics of the main shaft system in a hydro-turbine based on ansys. *Procedia Engineering*, 31:654–658, 2012.

[29] Y. Fang and Y. Li. Dynamic responses of nickel-based single crystal superalloy dd6 blade. *Journal of Materials Engineering and Performance*, 22(6):1565–1573, 2013.

[30] Z. Kai, D. Xingjian, and Z. Xiaozhang. Dynamic analysis and control of an energy storage flywheel rotor with active magnetic bearings. In *Proc. of the International Conference on Digital Manufacturing & Automation*, 2010.

[31] X. Dai, K. Zhang, and X. Zhang. Design and test of a 300wh composites flywheel energy storage prototype with active magnetic bearings. In *Proc. of the International Conference on Renewable Energies and Power Quality*, 2011.

[32] M. Grujicic, G. Arakere, B. Pandurangan, V. Sellappan, A. Vallejo, and M. Ozen. Multidisciplinary design optimization for glass-fiber epoxy-matrix composite 5 mw horizontal-axis wind-turbine blades. *Journal of Materials Engineering and Performance*, 19(8):1116–1127, 2010.

[33] J. S. Park and J. H. Kim. Design and aeroelastic analysis of active twist rotor blades incorporating single crystal macro fiber composite actuators. *Composites Part B: Engineering*, 39(6):1011–1025, 2008.

[34] S. Singhal, K.V. Singh, and A. Hyder. Effect of laminated core on rotor mode shape of large high speed induction motor. In *Proc. of the International Electric machines & Drives Conference*, Niagara Falls, Canada, 2011.

[35] R. Mistry, B. Finley, S. Kreitzer, and R. Queen. Influencing factors on motor vibration & rotor critical speed in design, test and field applications. In *Proc. of the International Petroleum and Chemical Industry Technical Conference*, San Francisco, USA, 2014.

[36] D. Combescure and A. Lazarus. Refined finite element modelling for the vibration analysis of large rotating machines: Application to the gas turbine modular helium reactor power conversion unit. *Sound and Vibration*, 318:1262–1280, 2008.

[37] A. L. Gyekenyesi, J. T. Sawicki, and W. C. Haase. Modeling disk cracks in rotors by utilizing speed dependent eccentricity. *Journal of Materials Engineering and Performance*, 19(2):207–212, 2010.

[38] C. R. Morrison, A. Provenza, A. Kurkov, G. Montague, K. Duffy, O. Mehmed, D. Johnson, and R. Jansen. Fully suspended, five-axis, three-magnetic-bearing dynamic spin rig with forced excitation. *Experimental Mechanics*, 45(3):226–237, 2005.

[39] J. J. Sinou. An experimental investigation of condition monitoring for notched rotors through transient signals and wavelet transform. *Experimental Mechanics*, 49(5):683–695, 2009.

[40] R. Sino, T.N. Baranger, E. Chatelet, and G. Jacquet. Dynamic analysis of a rotating composite shaft. *Composite Science and Technology*, 68:337–345, 2008.

[41] B. G. Choi and B. S. Yang. Optimum shape design of rotor shafts using genetic algorithm. *Journal of Vibration and Control*, 6:207–222, 2000.

[42] R. R. Chang and J. M. Chu. Predictions of first-ply failure load of laminated composite shafts. *Experimental Mechanics*, 43(2):183–193, 2003.

[43] S. Chen, C. Kung, T. Liao, and Y. Chen. Dynamic effects of the interference fit of motor rotor on the stiffness of a high speed rotating shaft. *Transactions of the Canadian Society for Mechanical Engineering*, 34(2):243–261, 2010.

[44] http://beaconpower.com/carbon-fiber-flywheels/ (last seen, 17.05.2016).

[45] http://www.power-thru.com/ (last seen, 17.05.2016).

[46] http://stornetic.com/. http://stornetic.com/ (last seen, 17.05.2016).

[47] http://www.gkn.com/landsystems/brands/hybrid-power/technology-and-innovation/Pages/default.aspx (last seen, 17.05.2016).

[48] http://www.torotrak.com/products-partners/products/flybrid/ (last seen, 17.05.2016).

[49] http://www.ricardo.com/en-GB/News–Media/Press-releases/News-releases1/2011/Breakthrough-in-Ricardo-Kinergy-second-generation-high-speed-flywheel-technology/ (last seen, 17.05.2016).

[50] http://www.schenck-rotec.de/userFiles/library-PDF/RM1015d.pdf (last seen, 17.05.2016).

[51] G. Genta. Spin tests on medium energy density flywheels. *Composites*, 13:38–46, 1982.

[52] H. E. Sonnichsen. Ensuring spin test safety. *Mechanical Engineering*, 115(5):72–77, 1993.

Bibliography

[53] E. D. Reedy and H. K. Street. Composite-rim flywheels: Spin tests. *SAMPE Quarterly*, 10:36–41, 1979.

[54] A. D. Sapowith and W. E. Handy. A composite-flywheel burst-containment study. *Report No.AVSD-0350-81-RR*, 1982.

[55] L. M. Trase. The evaluation and implementation of a water containment system to support aerospace flywheel testing. In *Proc. of the 37th Intersociety Energy Conversion Engineering Conference*, pages 234–238, 2002.

[56] M. Strasik, P. E. Johnson, A. C. Day, and et al. Design, fabrication, and test of a 5-kwh/100-kw flywheel energy storage utilizing a high-temperature superconducting bearing. *IEEE Transactions on Applied Superconductivity*, 17(2):2133–2137, 2007.

[57] D. H. Curtiss, P. P. Mongeau, and R. L. Puterbaugh. Advanced composite flywheel structural design for a pulsed disk alternator. *IEEE Transactions on Magnetics*, 31:26–31, 1995.

[58] G. Nagy, S. Rosenwasser, and G. Mehle. The evaluation and testing of graphite fiber composite materials for high speed rotors. *IEEE Transactions on Magnetics*, 31:289–293, 1999.

[59] G. Nagy and S. Rosenwasser. The evaluation of advanced composite material performance in high speed pulsed power rotor applications. *IEEE Transactions on Magnetics*, 37:314–317, 2001.

[60] V. Lelos, S. Manifold, and J. Granier. Structural properties and testing of a composite banding used in high-speed rotors. *IEEE Transactions on Magnetics*, 43:250–253, 2007.

[61] J. Tzeng, R. Emerson, and P. Moy. Composite flywheels for energy storage. *Composites Science and Technology*, 66:2520–2527, 2006.

[62] R. N. Headifen, S. Gupta, and D. Okey. Experimental testing of thick-walled graphite fiber composite rings. *Composites Science and Technology*, 51(4):531–536, 1994.

[63] R. Ahmad, F. A. R. Al-Salehi, S. T. S. Al-Hassani, and M. J. Hinton. Strength and failure modes of hoop wound cfrp tubes under compressive high rates of loading. *Applied Composite Materials*, 12(5):277–292, 2005.

[64] F. A. R. Al-Salehi, S. T. S. Al-Hassani, H. Haftchenari, and M. J. Hinton. Effect of temperature on the tensile strength and failure modes of angle ply cfrp tubes under hoop loading. *Applied Composite Materials*, 5(5):319–343, 1998.

[65] F. A. R. Al-Salehi, S. T. S. Al-Hassani, H. Haftchenari, and M. J. Hinton. Temperature and rate effects on grp tubes under tensile hoop loading. *Applied Composite Materials*, 8:1–24, 2001.

[66] H. Haftchenari, F. A. R. Al-Salehi, S. T. S. Al-Hassani, and M. J. Hinton. Effect of temperature on the tensile strength and failure modes of angle ply aramid fibre (krp) tubes under hoop loading. *Applied Composite Materials*, 9:99–115, 2002.

[67] M. Kaltenbacher. *Numerical Simulation of Mechatronic Sensors and Actuators: Finite Elements for Multiphysics.* Springer, Berlin, Germany, 3rd edition, 2015.

[68] *COMSOL MULTIPHYSICS® Academic Research, Release 4.2b, Structural Mechanics Module Analysis Guide, COMSOL, Inc.*

[69] *ANSYS® Academic Research, Release 13.0, Help System, Rotordynamic Analysis Guide, ANSYS, Inc.*

[70] T. Mori and K. Tanaka. Average stress in the matrix and average elastic energy of materials with misfitting inclusions. *Acta Metallurgica*, 21:571–574, 1973.

[71] Y. Benveniste. A new approach to the application of mori-tanaka's theory in composite materials. *Mechanics of Materials*, 6:147–157, 1987.

[72] J. N. Reddy. *Mechanics of laminated composite plates and shells: theory and analysis.* CRC Press, Boca Raton, USA, 2 edition, 2003.

[73] S. W. Tsai. *Theory of Composites Design.* Think Composites. Dayton, USA, 1992.

[74] S. Hartl. *Metrological recording of load limits and identification of the material parameters of composite flywheel rotors.* Diploma thesis, TU–Wien, 2012.

[75] S. Hartl, A. Schulz, and M. Kaltenbacher. Direct estimation of the elastic constants of cfrp plates by using lagrange's equation. In *Proc. of the International Conference on Composite Structures*, Lisbon, Portugal, June 15-18 2015.

[76] US Department Of Defense. *Composite Materials Handbook-MIL 17, Volume 2: Polymer Matrix Composites: Materials Properties.* CRC Press, Boca Raton, USA, 2000.

[77] MATLAB. *version 7.11.0 (R2010b).* The MathWorks Inc., Natick, Massachusetts, 2010.

[78] *DIN EN ISO 527-1:2012-06, Kunststoffe - Bestimmung der Zugeigenschaften - Teil 1: Allgemeine Grundsätze (ISO 527-1:2012).*

[79] *DIN EN ISO 527-5:2010-01, Kunststoffe - Bestimmung der Zugeigenschaften - Teil 5: Prüfbedingungen für unidirektional faserverstärkte Kunststoffverbundwerkstoffe (ISO 527-5:2009).*

[80] *DIN EN ISO 2561:1995, Kohlenstofffaserverstärkte Kunststoffe - Unidirektionale Laminate, Zugprüfung parallel zur Faserrrichtung.*

[81] *DIN EN ISO 14129:1998-02, Faserverstärkte Kunststoffe - Zugversuch an 45-Laminaten zur Bestimmung der Schubspannungs/Schubverformungs-Kurve des Schubmoduls in der Lagenebene (ISO 14129:1997).*

[82] *DIN EN ISO 14126:2000-12, Faserverstärkte Kunststoffe - Bestimmung der Druckeigenschaften in der Laminatebene (ISO 14126:1999).*

[83] *DIN EN ISO 14125:1998, Faserverstärkte Kunststoffe - Bestimmung der Biegeeigenschaften.*

[84] *ASTM D2290-12, Standard Test Method for Apparent Hoop Tensile Strength of Plastic or Reinforced Plastic Pipe.*

[85] S. Hartl, A. Schulz, H. Sima, T. Koch, and M. Kaltenbacher. A static burst test for composite flywheel rotors. *Applied Composite Materials*, pages 1–18, 2015.

[86] T. Hinterdorfer, A. Schulz, H. Sima, S. Hartl, and J. Wassermann. Topology optimization of a flywheel energy storage rotor using a genetic algorithm. In *Proc. of the International Symposium on Magnetic Bearings*, Linz, Austria, August 11-14 2014. IEEE.

[87] T. Hinterdorfer. *Effizienter Energietransfer und Steigerung der Energiedichte bei magnetisch gelagerten Schwungradspeichern.* Dissertation, TU–Wien, 2014.

[88] C. Millan, M. A. Jimenez, and A. Miravete. Finite element calculation of a press fit joint between a composite materials tube and an aluminium cylinder. *Applied Composite Materials*, 6(6):369–380, 2001.

[89] M. P. Bendsoe and O. Sigmund. *Topology Optimization.* Springer, Berlin, Germany, 2nd edition, 2004.

[90] A. H. Gandomi, X. S. Yang, S. Talatahari, and A. H. Alavi. *Metaheuristic Applications in Structures and Infrastructures.* Elsevier, Oxford, GB, 2013.

[91] H. Sekine and E. Shin. Optimum design of thick-walled multi-layered cfrp pipes to reduce process-induced residual stresses. *Applied Composite Materials*, 6(5):289–307, 1999.

[92] P. A. Smith, L. Boniface, and N. F. C Glass. A comparison of transverse cracking phenomena in (0/90)s and (90/0)s cfrp laminates. *Applied Composite Materials*, 5:11–23, 1998.

[93] W. Chen, Y. Yu, P. Li, C. Wang, T. Zhou, and X. Yang. Effect of new epoxy matrix for t800 carbon fiber/epoxy filament wound composites. *Composites Science and Technology*, 67:2261–2270, 2007.

[94] S. L. Gao, E. Mäder, and S. F. Zhandarov. Carbon fiber and composites with epoxy resins: topography, fractography and interphases. *Carbon*, 42(3):515–529, 2004.

[95] I. Cerny and R. M. Mayer. Fatigue of selected grp composite components and joints with damage evaluation. *Composite Structures*, 94(2):664–670, 2012.

[96] S. Hartl and M. Kaltenbacher. Design of a cfrp hollow shaft to increase the energy density of a flywheel rotor. *Composites Part B: Engineering*, to be published 2016.

[97] S. Hartl, A. Schulz, and M. Kaltenbacher. Optimum design of a high energy density composite flywheel rotor. In *Proc. of the Vienna young Scientists Symposium*, Wien, Austria, June 25-26 2015. TU Wien.

[98] S. Hartl, A. Schulz, and M. Kaltenbacher. Design of a carbon fiber reinforced plastic shaft for a high speed flywheel rotor. In *Proc. of the International Conference on Composite Materials*, Cobenhagen, Denmark, July 19-24 2015.

[99] A. Schulz, S. Hartl, H. Sima, T. Hinterdorfer, and J. Wassermann. Innovative flywheel energy storage system with high energy efficiency and reliability. *e&i Elektrotechnik und Informationstechnik*, 132(8):481–490, 2015.

[100] A. Schulz. *Entwicklung eines aktiven Magnetlagers mit hoher Betriebssicherheit.* Dissertation, TU–Wien, 2006.

[101] H. Sima. *Erhöhung der erzielbaren Speicherzeit von magnetisch gelagerten Schwungradspeichern.* Dissertation, TU–Wien, 2014.

[102] T. Hinterdorfer, A. Schulz, H. Sima, S. Hartl, and J. Wassermann. Compensation of unbalance forces of a switched reluctance machine with combined current and fluxlinkage control. In *Proc. of the International Symposium on Magnetic Bearings*, Linz, Austria, August 11-14 2014. IEEE.

[103] A. Schulz, T. Hinterdorfer, H. Sima, J. Wassermann, and M. Neumann. *FLYWHEEL*. WO Patent 2013170284 (A1). issued November 21, 2013.

[104] D. Norfield. *Practical Balancing of Rotating Machinery.* Elsevier, Amsterdam, Netherland, 2 edition, 2006.

[105] *DIN EN ISO 1940:1-2003, Mechanische Schwingungen Anforderungen an die Auswuchtgüte von Rotoren in konstantem (starrem) Zustand Teil 1: Festlegung und Nachprüfung der Unwuchttoleranz.*

[106] G. Schweitzer and E.H. Maslen. *Magnetic Bearings.* Springer, Heidelberg, Germany, 2009.

[107] http://www.epectec.com/batteries/cell-comparison.html (last seen, 17.05.2016).

Curriculum Vitae

Personal Data

- **Name:** Stefan Hartl

- **Date of birth:** March 12, 1987

- **Place of birth:** Amstetten, Austria

Education

- **M.Sc.**, Master Program Mechanical Engineering focused on Mechatronics, Vienna University of Technology, 2012, Master Thesis: *Metrological recording of Load Limits and Identification of the Material Parameters of Composite Flywheel Rotors*

- **B.Sc.**, Bachelor Program Mechanical Engineering, Vienna University of Technology, Austria, Vienna, 2010, Bachelor Thesis: *Extension of an existing Pump Test Rig*

- **High School Diploma**, Mechanical Engineering focused on Automation Technology, Federal Higher Technical Institute for Educating and Experimenting, Austria, Waidhofen/Y., 2006, Thesis: *Fully automatic Sandblasting Machine for Saw Blades*

Professional Experience

- **Project assistant**, working within the nationally supported research project "Optimum-Shape-Flywheel", Vienna University of Technology, Institute of Mechanics and Mechatronics, Austria, Vienna, February 2013 to February 2016.

- **Project assistant**, working within projects "ARGOS Rail" and "ARGOS Road", Hottinger Baldwin Messtechnik, Austria, Vienna, August 2012 to January 2013.

- **Teaching assistant**, Vienna University of Technology, Institute of Mechanics and Mechatronics, Austria, Vienna, 2008 to 2012.

- **Summerjobs**, DOKA Formwork Experts, Austria, Amstetten, 2003 to 2011.